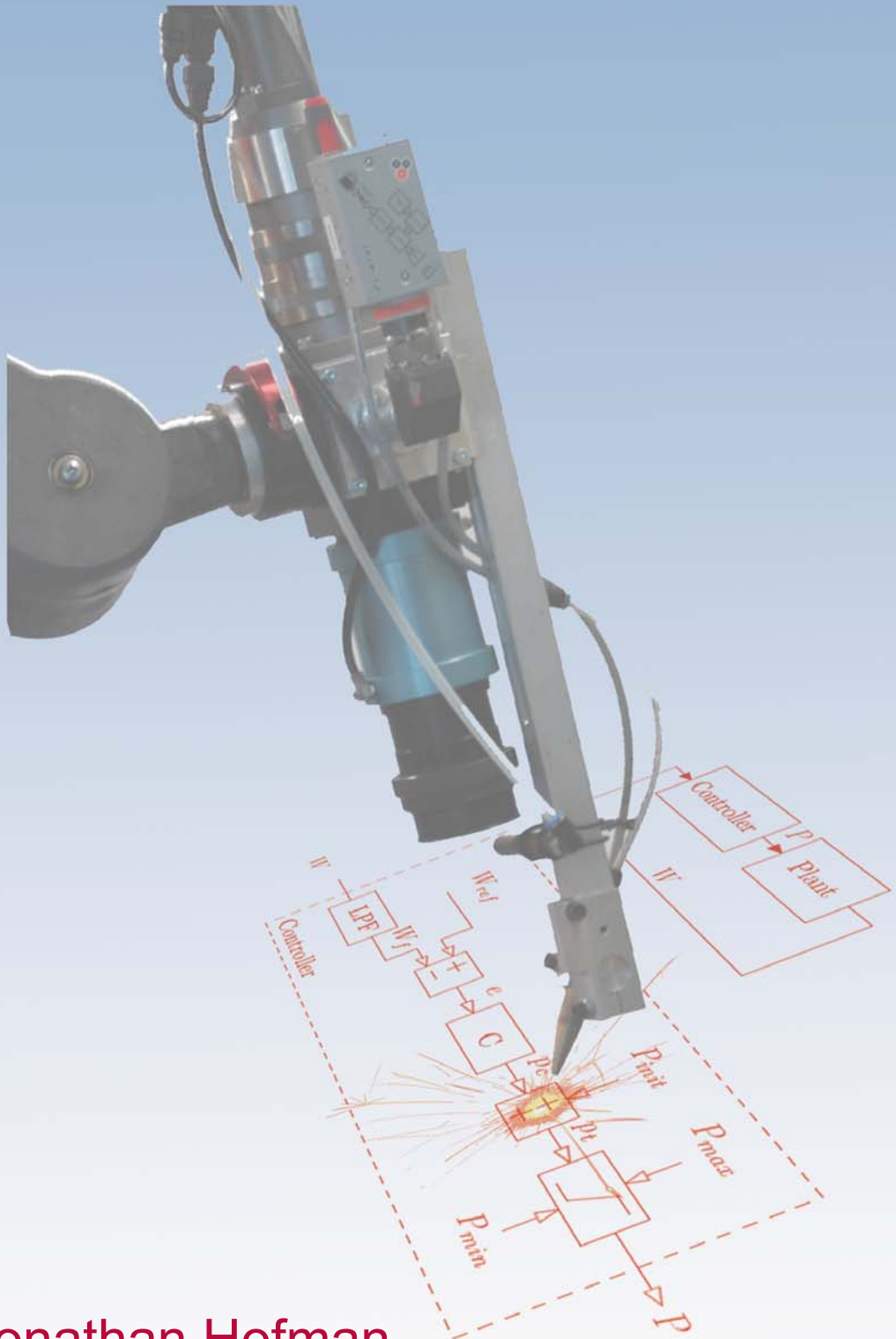


Development of an Observation and Control System for Industrial Laser Cladding



Jonathan Hofman

DEVELOPMENT OF AN OBSERVATION
AND CONTROL SYSTEM FOR
INDUSTRIAL LASER CLADDING

Jonathan Hofman



The research described in this thesis is carried out in the framework of the Research Program of the Materials innovation institute M2i (www.m2i.nl), the former Netherlands Institute for Metals Research.

Development of an Observation and Control

System for Industrial Laser Cladding

Hofman, Johannes Tjaard

ISBN 978-90-77172-42-1

©2009 J. T. Hofman, Enschede, the Netherlands.

Printed by Ipskamp Drukkers BV.

DEVELOPMENT OF AN OBSERVATION
AND CONTROL SYSTEM FOR
INDUSTRIAL LASER CLADDING

PROEFSCHRIFT

ter verkrijging van
de graad van doctor aan de Universiteit Twente,
op gezag van de rector magnificus,
prof. dr. H. Brinksma,
volgens besluit van het College voor Promoties
in het openbaar te verdedigen
op vrijdag 13 februari 2009 om 15.00 uur

door

Johannes Tjaard Hofman
geboren op 13 December 1979
te Oldehove

Dit proefschrift is goedgekeurd door
prof.dr.ir. J. Meijer, promotor
dr.ir. B. Pathiraj, assistent-promotor

Summary

Laser cladding has become an important surface modification technique in today's industry. It is not only applied for coating new products but also for repair and refurbishment as well as in rapid prototyping. Due to the complexity of the process, a highly skilled operator is required.

A laser clad workstation has been developed. It uses a 4 kW Nd:YAG fibre coupled laser as heat source. The specially developed optical system is mounted on a six-degree of freedom industrial robot, allowing the cladding of complicated 3-dimensional products. This system combines the benefits from a Top-hat energy distribution with a practical working distance. The clad material is supplied to the melt pool by a powder nozzle. A high velocity gas flow around the powder jet allows a focussed powder stream.

A camera based monitoring system for the laser cladding process has been developed. This system determines the main dimensions of the melt pool in real-time.

A developed FEM model of the laser cladding process accurately predicts the shape and temperature of the clad layers by including the interaction between the laser beam and the powder jet. The model results are in good correspondence with experimental results.

An extensive set of cladding experiments has been performed with variable spot size, laser power, cladding speed and powder mass rate. From these experiments, optimal process conditions could be determined.

From the experimental work, a clear correlation between the dilution and the width of the melt pool was found. This correlation was found to be independent of the substrate temperature, enabling real time control of

the dilution by adjusting the laser power.

A feedback control strategy was developed and implemented based on the melt pool width information from the camera. As a result, the energy input into the substrate and consequently thermal distortion of the products is minimized, while a good metallurgical bonding and minimal dilution are obtained. Due to this minimal dilution, the hardness of the clad layer can be controlled and maintained to be uniform.

High temperature gradients and different material properties may cause high residual stresses or even cracks. To investigate this effect, a simple and fast method based on deflection measurements has been developed. The residual stress values obtained by this procedure have been compared with stresses from X-ray measurements. The results show a good agreement for Stellite 12 clad layers on a steel substrate. Tensile stresses of large magnitude develop in the layer which increase with the cladding speed.

The control strategy is implemented in C++ code running under the WindowsTM operation system. This system was implemented and tested in industry (Stork Gears & Services, Rotterdam, The Netherlands) providing increased use of the cladding technique with better quality assurance.

Contents

Summary	i
Contents	vi
1 Introduction	3
1.1 Outline	3
2 Laser cladding: state-of-the-art	5
2.1 Introduction	5
2.2 Surface modification	5
2.3 Laser surface modification	7
2.4 Laser Cladding	8
2.4.1 Process description	8
2.4.2 Process development	13
2.4.3 Modeling	14
2.4.4 Materials properties	16
2.4.5 Applications of laser cladding	17
2.4.6 Sensing and control	19
2.5 Motivation for the current research	21
3 Experimental setup	23
3.1 Introduction	23
3.2 Laser and manipulator	23
3.3 Optical systems and energy distributions	26
3.3.1 Standard optical system	26
3.3.2 Tele-zoom optical system	28
3.4 Powder delivery nozzle	31
3.5 Review and conclusions	33

4	Influence of process settings on the heat flow and clad characteristics	37
4.1	Introduction	37
4.2	Heat balance and boundary equation	38
4.3	Influence of process settings	40
4.3.1	Influence of the cladding speed and laser power	40
4.3.2	Influence of the powder jet on the heat input distribution	41
4.3.3	Influence of the initial substrate temperature	42
4.4	Influence of the laser beam distribution	43
4.4.1	Laser beam diameter	43
4.4.2	Laser beam energy distribution	43
4.5	Review and conclusions	49
5	Monitoring system	51
5.1	Introduction	51
5.2	Optical path	52
5.2.1	Process radiation	53
5.2.2	Spectroscopic analysis	54
5.2.3	Intensity as function of the temperature	56
5.3	Image processing	57
5.3.1	Processing time	60
5.4	Accuracy of the measurements	61
5.5	Powder material and required threshold level	62
5.6	Review and conclusions	65
6	Modeling of the melt pool	67
6.1	Introduction	67
6.2	Finite Element Model	67
6.2.1	Heat balance	68
6.2.2	Boundary equations	70
6.2.3	Geometrical transformation	72
6.3	Review and conclusions	75
7	Clad characteristics and correlations using FEM model simulation and experiments	77
7.1	Introduction	77
7.2	Simulation and experimental procedures	78
7.2.1	Simulations procedure	78

7.2.2	Experimental procedure	80
7.3	Results and discussion	81
7.3.1	Influence of the process settings on the clad characteristics	84
7.4	Influence of the dilution on the hardness	89
7.5	Sensor for real-time dilution control	91
7.6	Temperature fields and cooling rates	97
7.7	Review and conclusions	98
8	Feedback control system	101
8.1	Introduction	101
8.2	System identification	101
8.3	Feedback controller	105
8.4	Implementation	110
8.4.1	Analogue signal routing	112
8.5	Review and conclusions	112
9	Controller performance	113
9.1	Introduction	113
9.2	Influence of the powder material on the controllability	113
9.3	Controlled cladding of a thin steel plate	115
9.4	Influence of heat accumulation and geometry changes	116
9.4.1	Determination of the melt pool width	118
9.4.2	Monotonous increasing relation between laser power and melt pool	120
9.4.3	Controlled cladding on a solid bar	121
9.4.4	Fixed laser power cladding on a bar with changing geometry	122
9.4.5	Controlled cladding on a bar with changing geometry	125
9.4.6	Hardness in clad layers with respect to control of dilution.	126
9.5	Review and conclusions.	128
10	Industrial implementation of the controller	131
10.1	Introduction	131
10.2	Laser cladding setup	131
10.3	Optical path and process radiation	132
10.4	Controller system	135
10.5	Controlled cladding	137

10.5.1	Observability of the melt pool	138
10.5.2	Determination of the melt pool width	139
10.5.3	Progressive relation between laser power and melt pool	139
10.5.4	Maintain a constant melt pool width	140
10.5.5	Overlap cladding	142
10.5.6	Influence of the substrate temperature	143
10.5.7	Cladding of a pitch shaft of a windmill turbine.	145
10.6	Review and conclusions	147
11	Residual stresses	151
11.1	Introduction	151
11.2	Experimental setup and procedure	151
11.3	Relations between process settings and residual stresses	154
11.3.1	Plastic and elastic deformations	154
11.3.2	Laser power	155
11.3.3	Deflection	155
11.3.4	Stress distribution in the clad layer	156
11.3.5	Stresses at the surface	157
11.3.6	Stress as function of cladding speed	159
11.4	Review and conclusions	162
12	Conclusions	165
A	Ray pattern of the variable focus optics	171
B	Powder jet speed	173
C	Laser and Powder interactions	177
D	Cross-section images of Clad tracks using a 3.0 mm spot	185
E	Cross-section images of Clad tracks using a 4.5 mm spot	187
F	Cross-section images of Clad clad layers	189
	Samenvatting	193
	Acknowledgment	197
	Bibliography	198

Nomenclature

Abbreviations

3D	Three dimensional
a.u.	Arbitrary units
CCD	Charged Coupled Devices
CMOS	Complementary MetalOxideSemiconductor
CW	Continuous Wave
FEM	Finite Element Method
HAZ	Heat Affected Zone
HPDL	High Power Diode Laser
LPF	Low Pass Filter
Nd:YAG	Neodymium-doped Yttrium Aluminium Garnet
PI	Proportional-Integral
PID	Proportional-Integral-Differential

Symbols

A_b	Cross-sectional area of molten substrate material	m^2
A_c	Cross-sectional area of clad track	m^2
a	heat diffusion coefficient	m^2/s
C	Absorptivity	
c_p	Specific heat	$J/(kg\ K)$
D_c	Dilution	
d_{spot}	Diameter of the (focused) laser beam	mm
E_d	Energy density	J/m^2
E_s	Specific energy	J/m
H	Heat input	J/m^2

H_c	Height of clad track	m
H_m	Latent heat of fusion	J/kg
I	Irradiance	W/m ²
I_s	Power intensity on the surface	W/m ²
I_p	Laser beam intensity distribution	W/m ²
k	Thermal conductivity	W/(m K)
\dot{M}	Powder feed rate	kg /s
ρ	Density	kg/m ³
Pe	Péclet number	
P_l	Laser power	W
P_i	Initial laser power	W
q	Heat flux on the clad domain	W/m ²
t	Time	s
T	Temperature	K
$T_{threshold}$	Grayscale value of image which corresponds to the melt temperature	
V_c	Cladding speed	m/s
v_p	Powder jet speed	m/s
W	Melt pool width	m
W_c	Width of clad track	m
$W_{reference}$	Reference (target) melt pool width	m
\mathbf{x}	Spacial coordinates	m
ϵ	Strain	
λ	Wavelength	m
λ_{max}	Maximum principle moment	m ⁴
λ_{min}	Minimum principle moment	m ⁴
Φ	Power flux intensity	m/s
σ	Stress	MPa
τ	Time constant	s

Notations

\tilde{a}	Dimensionless version of a
\mathbf{a}	Vector or array
\mathbf{a}^T	Transpose of \mathbf{a}
\dot{a}	$\frac{d}{dt}a$
$a(b)$	a is a function of b
∇	$(\frac{\partial}{\partial x_1}, \dots, \frac{\partial}{\partial x_N})$

Chapter 1

Introduction

With the increasing complexity of products, the market for functional materials has increased significantly during the past years. Materials nowadays require multiple conflicting properties such as high hardness and ductility. Different properties however are often required at different locations on the products. Wear and corrosion resistance are only required at the surfaces of products for instance. Many fabrication solutions exist for applying functional coatings. A superior coating technique, which manifest a metallic bonding of substrate and coating, is the laser cladding technique. Laser cladding has become an important surface modification technique in today's industry and continues to gain market. Laser cladding is not only applied for coating but also for repair and refurbishment as well as for rapid prototyping. The work as described in this thesis focusses on the investigation and automation of the laser cladding process.

1.1 Outline

In chapter 2 the state of the art of the laser cladding technique is presented. Based on this state of the art, the objectives of this thesis are formulated. In chapter 3 the experimental setup, which is used throughout this research is presented.

Chapter 4 discusses the influence of process settings on the clad and melt pool characteristics from a physical point of view. It discusses the influence of the energy distribution on the quality of the produced clad layers and motivates the use of a top-Hat energy distribution which is used throughout this research. Within this work, a camera based observation

and control system was developed. The observation system is presented in chapter 5. Chapter 6 describes the Finite Element Method (FEM) model which is developed as part of this work. In chapter 7, the results from the performed simulations and experiments are presented and the influence of the process settings on the results are discussed. The quality of the clad layer, especially the hardness, is highly influenced by the dilution. High levels of dilution should be avoided. In this work a camera based feedback controller is developed and discussed in chapter 8, which focusses on limiting the dilution. The effectiveness of the developed control system is demonstrated in chapter 9. Chapter 10 discusses the laser cladding capabilities in an industrial environment and the implementation of the process controller developed as part of this work. This leads to an increased quality control and a lead in the field of laser cladding companies. Laser cladding is often limited in its application due to the residual stresses in the clad layers, often leading to hot or cold cracking. Chapter 11 describes a fast method for the investigation and determination of residual stresses in such clad layers. Finally, in chapter 12 the work described in this thesis is reviewed, and conclusions are stated.

Chapter 2

Laser cladding: state-of-the-art

2.1 Introduction

Laser cladding is becoming an important surface modification technique in today's industry and is applied for coating, repair and refurbishment as well as for rapid prototyping. In this chapter, a general introduction of the laser cladding process is presented and compared to other surface modification processes. In addition the state of the art of the laser cladding technique is presented. This chapter is finalized by giving a preview of the work described in this chapter and formulating the objectives of this work.

2.2 Surface modification

Surfaces of materials are always in contact with their surrounding, resulting in degradations due to wear, erosion and corrosion. Surface modification aims at reducing such surface degeneration. Surface modification may involve the application of a coating, for instance by using chemical vapor deposition, plasma spraying and laser cladding. Surface modification can be applied to all kinds of products to increase performance, reduce costs, and modify the surface properties independent of the bulk material. This enables the realization of products with improved functionality, at reduced use of scarce and expensive materials.

The different surface modifications techniques which are currently being used in the surface industry are briefly summarized in Table 2.1. Each of the surface modification techniques has some advantages over other processes and sometimes they are used on a large scale. For instance, the spraying

Table 2.1: Surface treatment processes [1].

Surface Process	Process Characteristics
Laser	-Low heat input, thin layers, low dilution and porosity, high hardness, small HAZ, high initial equipment investment and slow processing rates
Welding	-Oxyacetylene - liquid /solid bond, high heat input -TIG - reasonable bonding, medium heat input -Open arc - low heat input -Shielded metal arc -MIG - reasonable bond, medium heat input -Submerged arc -Electroslag -Paste fusion -Plasma arc - Thick layers, high deposition rates, low equipment cost, covers large areas, high heat input and part distortion.
Spraying	-Flame Powder / Wire Fusion bond, no dilution -Electric arc metallising -Plasma Liquid/solid bond, low heat input, no dilution
Physical Vapor Deposition (PVD)	-Vacuum coating (thermal evaporation) -Sputtering -Ion plating -Ion implantation
Mechanical Plating	-Peening -Fillet rolling
Electrochemical	-Aqueous -Fused salts

processes have less heat input to the parts, resulting in virtually no thermal distortion of the products. The bonding however, is weak and the layers are relatively thin. The risk of damage of the layers therefore is high, making it less suited for mechanically loaded parts. The laser and the plasma arc surface modification techniques both yield good metallurgical bonding and thick layers can be produced, making them ideal for coating highly loaded parts. Successful application of these methods can be found in a lot of industries like gas, offshore, mining, food processing, engine and automotive industry.

2.3 Laser surface modification

Laser surface modification involves all the processes where a laser source is used to locally heat the surface. Using laser energy as heating source has some advantages over conventional heating sources [2, 3]:

1. The energy supply can be well controlled.
2. Selective surfacing of small areas is possible.
3. Controlled thermal profile and therefore shape and location of the heat affected region are limited.
4. The total heat input is low, resulting in minimal distortion.
5. The heating and cooling rates are high, resulting in a fine microstructure and/or metastable phases.
6. The treatment is a non-contact process. There is no tool wear and no mechanical forces act on the workpiece.
7. Chemical cleanliness and therefore minimal pollution.
8. The process is well suited for automation.

The laser surface modification processes can be divided into thermal and thermochemical processes . This is graphically expressed in Figure 2.1. The thermal processes such as surface hardening and melting, involve the modification of surface properties by changing the microstructure of the surface layer. The thermochemical processes such as alloying, cladding and particle dispersion, involve changing the surface properties by adding new materials to the laser generated melt pool. The degree of mixing between

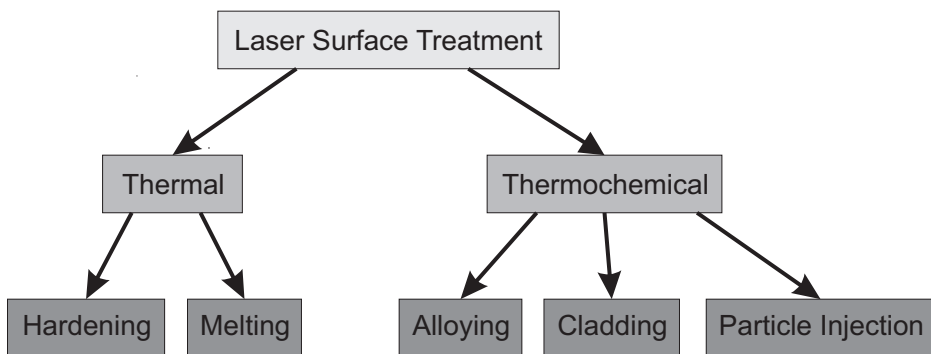


Figure 2.1: Division of the laser surface modification processes.

added and substrate materials depends on the method involved. With

particle dispersion, hard particles are injected into the melt pool, without melting the particles. Laser alloying changes the surface of the work piece by mixing an alloy material with the substrate. The alloy material is added to the melt pool and mixed with the base material to obtain the desired composition. The aim of laser cladding is to add an alloy material onto a surface without severe dilution. In this way, the properties of the surface layer will solely depend on the added material.

2.4 Laser Cladding

Laser cladding uses a high-power laser beam to melt a cladding material and a thin layer of the substrate to form a pore- and crack-free coating of typically 0.05 to 2 mm thick with low dilution that is perfectly bonded to the substrate [4].

2.4.1 Process description

The aim of laser cladding process is to deposit a clad layer onto surfaces of workpieces in order to generate functional layers or to regenerate the natural shape of parts. The material can be deposited in three different ways; by powder injection, by pre-placing the powder or by wire feeding. A laser beam generates a melt pool in the substrate and allows the additional material to be melted. By moving the laser beam over the surface, a solid layer is formed immediately after the laser has passed. Laser cladding by powder injection is superior to alternative processes because it is more energy efficient and it allows for better process control and reproducibility [5]. A great variety of materials can be deposited on a substrate by powder injection. Layer thicknesses range from 0.05 to 2 mm. Also multilayer cladding of the same or different materials is possible to achieve better mechanical properties or higher cladding thicknesses. The process is schematically shown in Figure 2.2. The powder flow can be off-axis or co-axial. In both cases the powder travels some distance through the laser beam causing the particles to be preheated or to be melted before they reach the melt pool. With laser cladding, the clad interface usually has a small dilution zone of substrate and clad material. In order to realize a such a small dilution zone, the process parameters and material combinations have to be adapted to the geometrical boundary conditions of the work piece. It is a combination of properties which makes the laser cladding process unique from the other laser surface treatments. Firstly, mixing of

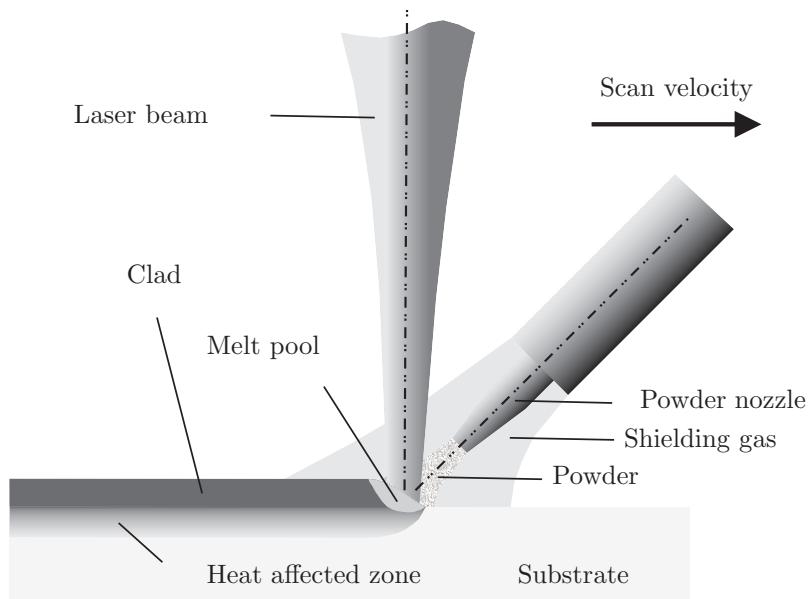


Figure 2.2: The laser cladding process

the cladding material with the substrate material can be kept very low. Hence, the surface properties of the coated product will primarily depend on the properties of the used cladding material. The cladding material can be chosen according to the service conditions during the lifetime of the product. Secondly, the bonding of the clad layer with the substrate is excellent. Thirdly, the process window of the input parameters is rather large, so the input parameters can be chosen with some margin.

The success of laser cladding relies on the quality of the obtained clad layer. The quality depends on a large variety of input and process parameters such as laser power, beam velocity, choice of material, spot dimensions, laser beam absorption and melt pool dynamics. The quality of a clad layer is classified into four groups [5], see Table 2.2.

In practice, it is hard to produce clad layers which possess all these properties. The clad layer is characterized by several geometrical quantities. The quantities H_c , W_c , A_c and A_b of Figure 2.3 are the clad layer height, width and the areas of clad and the molten base materials respectively. An important quality measure is the dilution (D_c) of the clad layer. A way to determine the dilution level, is by the concentrations of a specific element in the clad layer, the supplied clad material and the substrate

Table 2.2: Properties of clad layers.

Geometrical properties	Mechanical properties	Metallurgical properties	Qualitative properties
clad dimensions dilution roughness	hardness distribution residual stress wear resistance tensile strength	microstructure dilution grain size homogeneity corrosion resistance	porosity cracking

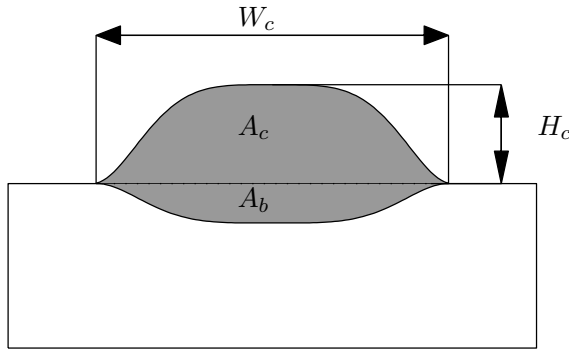


Figure 2.3: Schematic cross section of a clad layer.

material. Salehi [6] used the iron content to determine the dilution using the following equation:

$$D_c = \frac{L_{Fe} - P_{Fe}}{S_{Fe} - P_{Fe}} \quad (2.1)$$

where P_{Fe} , L_{Fe} and S_{Fe} are the iron concentration in the supplied powder, the clad layer and the substrate respectively. An approximation of the dilution level, which is used throughout this research, is the ratio between the area of the molten substrate material and the total area of the molten layer.

$$D_c = \frac{A_b}{A_b + A_c} \quad (2.2)$$

In order to obtain a surface layer which is hardly diluted by the substrate material, this ratio has to be as small as possible. However, if the ratio is zero, there is the risk of no fusion and bonding between cladding material

and substrate. Therefore a dilution between 2% and 10% is generally accepted. The dilution level depends on power level and the distributions of both the laser beam and the powder jet. Using a laser beam with a Gaussian energy distribution leads to more substrate material being molten in the center of a clad track while at the same time, the amount of molten substrate material at the sides of the track might be zero, i.e. no metallurgical bonding between substrate and clad layer exists. The width of the clad track is mainly correlated to the diameter of the used laser beam. The height of the layer is mainly determined by the powder feed rate.

Figure 2.4 depicts the input parameters of the cladding process and their relation to the clad quality and some geometrical features of the melt pool which are measurable by a camera.

Required energy

Laser cladding requires melting of the powder material and the surface layer of the substrate. The depth of the clad layer and the heat affected zone depend on the interaction time between laser and material, the laser power and the width of the track. A minimal combination of power density and interaction time is required for proper bonding. An important variable is the energy density:

$$E_d = \frac{P_l}{V_c \cdot d_{spot}} \quad (2.3)$$

Where

$$\begin{aligned} E_d &= \text{energy density} \\ P_l &= \text{laser power} \\ V_c &= \text{velocity of the laser beam over the substrate} \\ d_{spot} &= \text{diameter of the laser spot} \end{aligned}$$

Increasing the energy density increases the depth of the clad layer. However, it has to be kept in mind that there are energy losses by reflection and reradiation. A part of the laser power is reflected from the surface of the substrate. Secondly, a part is reflected from the powder particles as they approach the melt pool. Thirdly, a part is lost by radiation and convection from the melt pool. Fourthly, a part is lost by conduction from the melt pool to the substrate. Finally, a part of the laser power is absorbed by powder particles which do not enter the melt pool. The efficiency of the

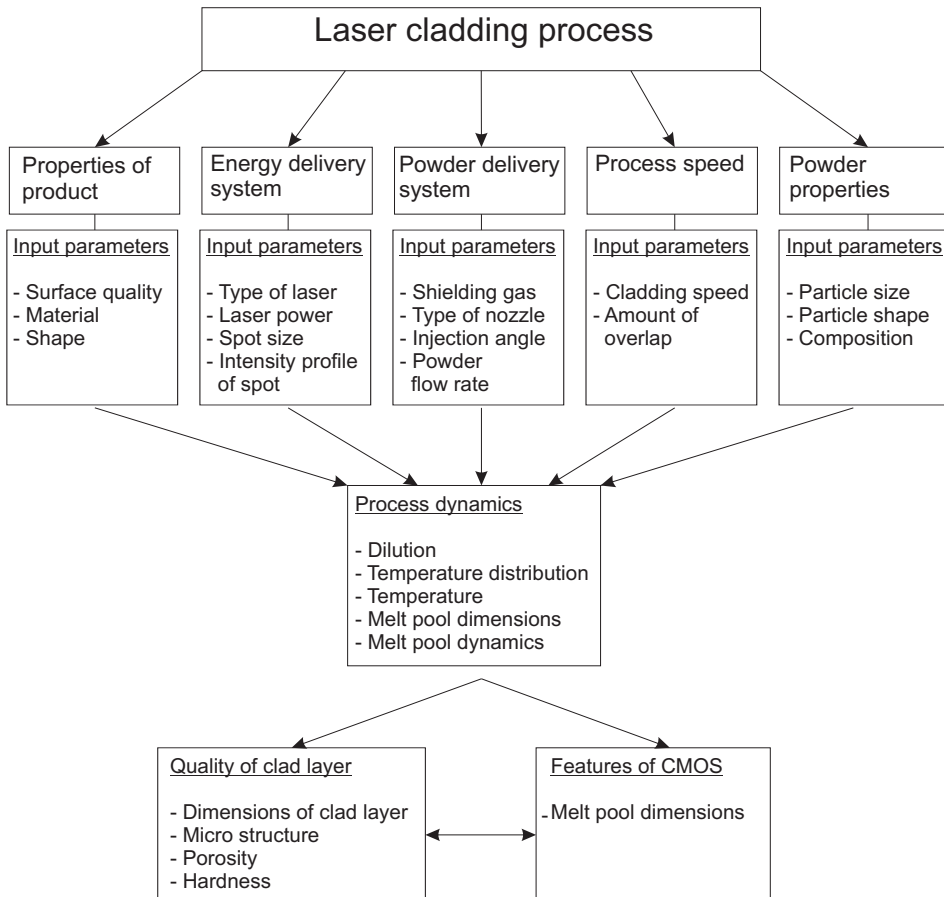


Figure 2.4: Interactions of Laser cladding input parameters to clad quality and online measurable quantities.

cladding process is examined by Gedda [7] and the results are displayed in Table 2.3

The laser power which is needed to melt the injected powder material can be calculated using:

$$P_l = \dot{M}(c_p \cdot \Delta T + H_m), \quad (2.4)$$

Table 2.3: Laser power efficiency

	Laser power Nd:YAG
Power reflected from the cladding melt	40 %
Power reflected from the powder cloud	10 %
Power used to heat the substrate	30 %
Power used to melt the clad layer	20 %

where

P_l = laser power

\dot{M} = powder feed rate

c_p = specific heat capacity of cladding material

ΔT = difference between the melt and ambient temperature

H_m = latent heat of fusion

As an example, using a 2 kW laser, about 500 W of energy will be used to melt the powder. Using Stellite 12 powder, about 75 mm³/s of clad material can be deposited. At a typical cladding speed of 20 mm/s, this results in a track of about 4 mm width and 1 mm high.

2.4.2 Process development

In the late 1980's, industrial applications made a break through. Leader companies include Rolls Royce, Pratt & Whitney, GM, Rockwell and Westinghouse, Fiat and others [8, 9]. The process development started with a two step process by pre-placing a paste of material on the surface which in a second step was molten by the laser. That process took much more time than the currently used one step process. In the later, the clad material is fed continuously during the process, mostly as a powder transported by an inert carrier gas. The powder can be supplied from the side or coaxial to the laser beam. Initially CO₂ lasers were used because of their high power and relatively high efficiency. Currently Nd:YAG and high power diode lasers (HPDL) are also successfully used for laser cladding. Because of their flexibility Nd:YAG lasers are applied in combination with optical fibres and robots. They are available in high powers although the wall plug efficiency is poor (some 3 %). Also HPDL are available in high power ranges. Besides the possibility to equip them with optical fibres, they can also be connected directly to a robot or Gantry system [10, 11]. The absorption of Nd:YAG

and HPDL laser radiation by the melt pool is comparatively high (40 %), but much higher than CO₂ - laser radiation (10 %). The wall plug efficiency of about 30 % of HPDL is relatively high although the beam quality is comparable low. It was shown in [12] a HPDL is a useful tool for laser cladding. The low beam quality is not a problem to obtain the required power density on the surface but it limits the ability to go into bores or other deep lying surfaces.

In order to improve the processing time of laser cladding with attendant improvements in the process efficiency, research activities are going on [13]. Fiber lasers are becoming available at high powers and beam quality nowadays [14]. A summary of the characteristics of these lasers is presented in Table 2.4.

Table 2.4: Commercial laser systems used for cladding.

Type	Output Power (kW)	Wavelength (μm)	Wall Plug Efficiency (%)	Beam Delivery
CO ₂	20	10.6	10	Mirror
Nd:YAG	6	1.06	3 to 5	Fiber
HPDL	4	0.9	30	Fiber
Fiber	50	1.07	30	Fiber

2.4.3 Modeling

To understand the different aspects of the laser cladding process, process models can be of aid. Many different modeling methods can be applied, all with their specific advantages. Models, which are found in literature can be distinguished as steady state models, dynamic models and lumped models. Some models focus on the melt pool, the powder injection and on how the clad geometry is formed.

In general, the modeling process can be described as follows. The laser beam reaches the substrate surface attenuated by the particles due to absorption and reflection. The laser power hits the substrate surface, producing a melt pool. The pre heated powder particles arrive in the melt pool. This part of the process is extensively described in the literature using the heat transfer equations for conduction and for convection caused by the moving beam [15, 16]. The depth of the melt pool should be small and equal over the diameter of the beam to avoid mixing of substrate material in the pool. Using an analytic approach it was shown that this can

be realized by choosing a power density distribution with higher intensities at the sides of the spot [17]. Although in laboratories it was proved to work well, in industry it is not applied up to now.

Melt pool flow has also been modeled extensively. Due to high temperature gradients, there will be a surface tension gradient driving the melt flow within the melt pool. Depending on the depth of the pool, the flow will either be in the surface plane for shallow pools and circulation in depth for deeper pools. The preheated particles or droplets yield a convective heat transfer which is taken into account only in a few numerical models until now [18].

Dynamic models of the process are important for process control. Both theoretical and empirical models have been developed. An analytical model was developed by Bamberger et al. [19] for estimating the process parameters by direct injection of powder into the melt pool. They used the model to control the cladding speed as a function of the temperature of the melt pool. A more advanced model was reported by Kim [20] who used a two dimensional, transient finite element technique. Empirical models for system identification have been developed by Römer [21, 15, 22] using autoregressive exogenous (ARX) system identification techniques to obtain dynamic models for laser alloying. These models used the scanning velocity and the laser power as inputs and the melt pool area as the output of the system. By measuring the melt pool area by a digital CMOS camera [23] they used this model to control the scanning speed and the laser power by means of feedback control. Although such systems are available nowadays, they are not yet used in industry because of the nonlinearity of the cladding process.

An interesting part of modeling laser cladding is the calculation of temperature distributions. Jendrzejewski [24] has calculated the temperature distribution for multi layer clads. To get closer to applications, Palumbo [25] has modeled the laser cladding process on ring geometries for the treatment of valve seats in engines. A combination of various modeling techniques was done by Toyserkani [26], including fundamental work of Picasso [27]. Another model was realized by Sameni [28]. In this model the clad height was calculated by a fuzzy logic based model. Further models for laser cladding are e.g. numerical FEM models, being developed in order to predict the metallurgical and the mechanical properties of laser clad layers on a substrate. Brückner [29, 30] calculated the residual stresses developed during the laser cladding process by FEM for single weld beads as well as for coatings consisting of different numbers of overlapping clad beads. They

showed that the stress state is significantly changed by the thermal and mechanical interaction of these beads during the laser treatment. Decreasing the cladding speed, effectively increasing the heating time, decreases the residual stresses from 900 MPa to 700 MPa. Preheating the substrate to a temperature of 300⁰C reduces the tensile stresses in the clad layer from 900 MPa to 700 MPa. Further increasing the substrate temperature does not lead to lower stresses. Higher temperatures however result in an increasing deformation of the substrate.

2.4.4 Materials properties

The laser cladding process can be used to produce layers on both ferrous and nonferrous substrates. Most cladding is done to improve surface properties of relatively heavy and cheap substrate materials. Therefore ferrous substrates form the majority of products nowadays. Depending on the application, cobalt, nickel and iron based materials are often used as clad material. In this section, the most widely used clad materials are discussed.

Cobalt base superalloys (trade name Stellites) are popular and are used to improve the wear resistance of mechanical parts in hostile environments. Usually they consist of about 60 % of cobalt, mixed with elements like nickel, chromium, tungsten, carbon and molybdenum. Chromium is added to form carbides and to provide strength to the cobalt matrix as well as to enhance the resistance against corrosion and oxidation. Tungsten and molybdenum have large atomic sizes and therefore give additional strength to the matrix. They also form hard and brittle carbides. Nickel is added to increase the ductility. The carbides are mostly the chromium rich M_7C_3 (M=metal) type. These carbides (~ 2200 HV) are responsible for the hardness of the clad (~ 550 HV) and for the wear resistance. In low-carbon alloys, other carbides such as M_6C and $M_{23}C_6$ are found. The hardness and the wear resistance for a given cobalt base powder mixture can be further improved by adding hard particles, such as carbides, nitrides and borides directly to this mixture. An example is the addition of tungsten carbide (WC/W_2C) to a cobalt base powder in order to enhance the abrasive wear resistance.

Nickel base alloys are used for applications in aggressive atmospheres at high temperatures. They have a good high temperature corrosion and oxidation resistance. Nickel base alloys can also be used as a substitute for cobalt. Elements that can be mixed with nickel are chromium, boron, carbon, silicon and aluminium. The formation of hard borides and silicon

carbide improves the wear resistance and hardness but these hard phases make the coating brittle. Hard particles can also be mixed with the clad powder. Addition of tungsten carbides to a mixture of Ni-B-Si gives a nickel rich structure with fine distributed Ni_3B and dissolved tungsten. The addition of boron and silicon improves the wetting behavior resulting in very smooth surfaces. Aluminium can be added to further increase the hardness by the formation of intermetallic phases ($NiAl_3$ and Ni_2Al_3) or oxides (Al_2O_3).

Iron base alloys, a mixtures of iron, chromium, carbon and manganese or tungsten show a good wear resistance due to the formation of carbides. The carbides are of the type M_6C instead of M_7C_3 , as found in cobalt base clad materials. Another application is the cladding of austenitic corrosion resistant layers on top of low carbon steels. The corrosion resistance can be further improved by increasing the molybdenum content.

Aluminium and titanium alloys are widely used to make parts for aerospace and automotive applications because of their low weight and high strength. At high temperatures, however, the mechanical properties and the wear resistance are poor. This can be improved by use of a nickel base clad layer thus combining the advantage of light weight with a high temperature wear resistance. Nickel, titanium and aluminium are known to form brittle intermetallic compositions which are sensitive to cracking. Well bonded aluminium oxide layers could be obtained by cladding aluminium alloys with a mixture of aluminium and silicon oxide. Then the following reaction will occur: $4Al + 3SiO_2 \Rightarrow 2Al_2O_3 + 3Si$. The presence of silicon in the oxide layer is favorable for the wetting by liquid aluminium. The hardness of an aluminium or titanium alloy can also be increased by the injection of a mixture of hard particles. Especially silicon carbide and titanium carbide seem to be useful hard particles. An application is a clad layer of a very hard cubic boron nitride and Ti_6Al_4V mixture on a Ti_6Al_4V compressor blade.

2.4.5 Applications of laser cladding

The laser cladding technique has found its way into the industry. Cladding is applied in the field of functional coatings, repair and prototyping. Clad layers are often used to increase the hardness of the surface and consequently increase the fatigue and wear resistance of these functional surfaces. Product examples are cladding of Stellite on cam shafts to increase the wear resistance, repair of worn sealing rings (Figure 2.5) and

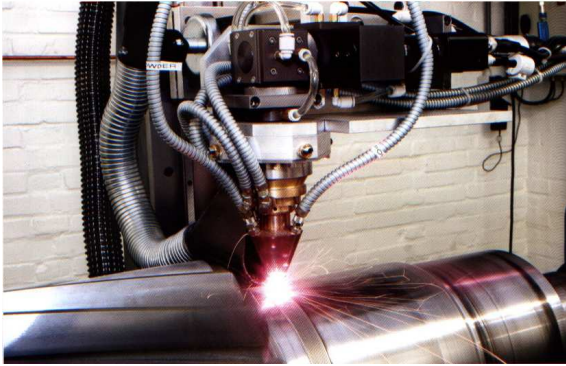


Figure 2.5: Laser clad repair of worn sealing ring, photo courtesy of Stork Gears & Services.



Figure 2.6: Laser cladding of a diesel engine intake valve.

cladding of diesel engine intake valves to increase the corrosion resistance (Figure 2.6). Laser cladding is also applied for products operating at high



Figure 2.7: Cladding of a large heat exchanger kalott. Operational temperature $> 1000^{\circ}\text{C}$ (Courtesy of NedClad Technology BV).

temperatures. Figure 2.7 shows a large heat exchanger kalott. This exchanger is about 1 meter in diameter and made of ferritic creep resistant

steel. A Stellite 21 clad layer is applied to protect the part from aggressive gasses at high temperature ($> 1000^{\circ}\text{C}$) by NedClad Technology BV, The Netherlands.



Figure 2.8: Cladding of a large valve (Courtesy of NedClad Technology BV).

Laser cladding is also used at the inside of valves used in natural gas extraction. The low alloyed 0.4% C steel surfaces have been corroded in a few years. An Inconel 625 layer is used in this application. These layers are applied for over ten years. So far, none of the surfaces have failed as inspections show. Figure 2.8 shows a photo of the repair of such a valve. The laser cladding technique is also highly suited for the local repair of worn sealing rings. Examples include axes used in wind turbines. Due to the nature of the laser cladding process, minimal heat input and limited distortion, the technique is suited for the repair of small parts. In those applications, local repair results in reduced costs as well as increased lifetime of the products. The laser cladding technique can also be used in the field of rapid prototyping. Products are built up in layers allowing complicated three dimensional products to be made, including closed holes in products. Functional parts are found in the aerospace industry, as well as in the medical field [31].

2.4.6 Sensing and control

The quality of a clad layer depends on the process parameters such as laser power, laser spot size, processing speed, and powder feed rate. All these variables have their effect on the temperature of the clad interaction zone. Laser cladding is currently an open-loop process. This means that the success of the cladding relies heavily on the skills of the operator. Unless the

required expertise is provided, the chance of a successful use of the cladding technique is small. Post-processing of poorly coated products is expensive and time consuming. Therefore, the need exists for online prediction and control of the clad properties. For industrial applications, online monitoring and controlling the cladding process is not widely in use now.

Bi et al. [32] investigated several infrared sensors such as pyrometer, photodiode and CCD camera as monitoring systems for the laser cladding process. They successfully implemented a control system which was based on the infrared temperature signal obtained by the photodiode. By adjusting the laser power in order to maintain a constant signal for the infrared temperature signal voltage, they managed to reduce the amount of molten substrate material.

Salehi et al. [6, 33] developed a multi variable control strategy based on a LabVIEW platform to control the laser cladding process. They adjusted the laser power to maintain a constant melt pool temperature. They discovered that during cladding, the melt pool size increases slightly. As a consequence, more powder is trapped into the melt pool. This leads to an increase in laser power to maintain the desired temperature, resulting in wider and higher tracks with increasing time. By combining the temperature information with data obtained by a photodiode, they implemented a multi variable control strategy. This controller was capable of controlling the laser power and cladding speed simultaneously. The combined control action was capable of producing clad tracks with a more constant clad height. Industrial implementation of such a controller, however, is not practical and too complicated. Provisional outcome of their investigation states that it could be promising to measure the geometrical dimension of the melt pool during the process using a CMOS camera.

Römer [34] used temperature information of the melt pool obtained by a pyrometer to control the laser alloying process. He also successfully implemented a control strategy based on the combination of the temperature pyrometer and the size of the melt pool as observed by a CCD camera. Both the laser power and scanning speed were used simultaneously as actuators. Using those control strategies he was able to control the thickness of the alloyed layer despite the fact that he did not measure the thickness directly.

Toyserkani et al. [35, 18] used a CCD camera to control the height of the clad layer in real-time. The clads height measured by an optical CCD-based detector is fed into a PID-based controller to tune the laser pulse energy in order to keep the clads height in a desired threshold. Closed loop

control significantly improved the height of the layer in case of changes in the absorption of the base material. Table 2.5 summarizes the control strategies as discussed above. Extensive research in the field of closed loop

Table 2.5: Various implemented control strategies.

	Objective	Sensor	Actuator
Bi et al. [32]	Dilution	Infrared temperature	laser power
Salehi [6]	Dilution / clad geometry	Pyrometer / photodiode	laser power / cladding speed
Römer [34]	Thickness of alloyed layer	CCD camera & Pyrometer	laser power / speed
Toyserkani et al. [35]	Track height	CCD camera	laser pulse energy

control of the laser cladding process has been performed. Further industrial application of the laser cladding technique requires the availability of such online controlled cladding systems. However, none of the aforementioned control strategies have found their way into industry because of the complicated nature of most control systems and the lack of robustness.

2.5 Motivation for the current research

It is evident from the information presented in the previous section that many aspects of the laser cladding process have been investigated already. Nevertheless, there are aspects that require attention in order to make the laser cladding process mature for industrial application.

The laser cladding process is highly complex. The different physical aspects, like for instance laser-workpiece interactions, laser-powder interactions and melt pool flow phenomena are only basically understood. In the present research work, several of these aspects are investigated and analyzed by means of a finite element model.

Both single track and overlap cladding experiments are used to determine the influence of the process settings on the clad characteristics. The experimental data is used to validate the finite element model predictions.

Not all the clad layer features (Figure 2.3), for example the extent of dilution, can be measured online. It is therefore of great interest to establish a good correlation between observable and controllable features and the dilution, which will allow real-time control of the dilution levels. Such a control system should be robust and easy to implement in industry.

In this research work, such a real-time controller has been developed and extensively tested.

Residual stresses are an important factor influencing the quality of clad layers. Due to the nature of the laser cladding process, high local temperature gradients exist. During the cool-down phase, these gradients combined with dissimilar material properties result in high differential thermal contractions and high residual stresses are found in clad layers [36]. It is hard to investigate experimentally the temperature gradients in the cladding zone and alternative solutions such as finite element method modeling can be of aid.

The objectives of this research are:

- Obtaining a better fundamental understanding of the laser cladding process.
- The development of a dedicated optical system for the laser beam delivery.
- The development of a Finite Element Method (FEM) model of the laser cladding process.
- Experimental and simulation analysis of the influence of the main process parameters on the clad characteristics.
- The development of a camera based feedback control system suited for industrial use.
- The evaluation of the influence of the main process parameters on the development of residual stresses.

Chapter 3

Experimental setup

3.1 Introduction

In this chapter the experimental setup used in this research is presented. This chapter starts presenting the used Nd:YAG laser and the manipulator system. In section 3.3 the tele-zoom optical system developed and used in this work is presented. The last section of this chapter describes the powder feed system including the developed nozzle and the flow of the particle jet.

3.2 Laser and manipulator

The experimental work described in this thesis is performed using a lamp-pumped Nd:YAG rod laser (figure 3.1) with an CW output of 4 kW. The wavelength of 1064 nm is well suited for transport by optical fibers, which is an advantage for situations where a flexible beam delivery system is required. The laser is equipped with four fibres, which serve four different work cells. One of the work cells is solely used for laser cladding. Figure 3.2 shows a photograph of this cell. This cell is equipped with a six-degree of freedom industrial robot (Cloos Romat 310). The robot is controlled by the CLOOS ROTROL II robot controller and use the CAROLA operating system. The optical system is mounted on this robot, enabling the cladding of complicated three dimensional product surfaces. Experiments on cylindrical bars are performed using an external rotation table. The powder delivery system consist of a Twin 10C dual hopper powder feeder from Sulzer Metco, with independent powder volume feed and carrier gas feed controls. The powder is transported to the processing zone by a 3

mm inner diameter tube. An in-house developed nozzle focuses the powder in the melt pool. Using a second gas stream at high velocity around the powder jet results in a converging powder stream.



Figure 3.1: The HL 4006D Nd:YAG laser.



Figure 3.2: The Clad cell.

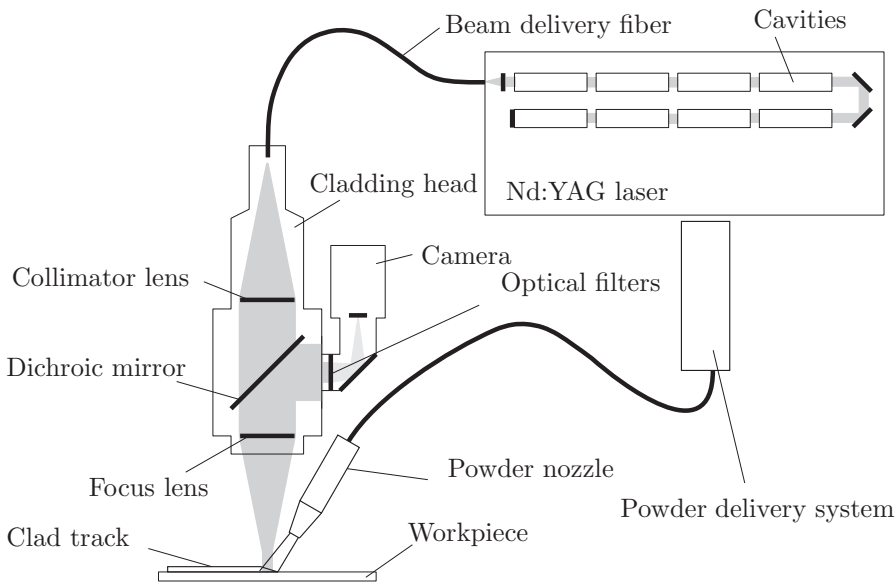


Figure 3.3: Schematic overview of the laser cladding system.

Upon exiting the beam delivery fiber, the laser beam diverges with an angle of about 9° . To reach the high intensity levels needed for laser material processing, the beam is focussed on the workpiece using an optical

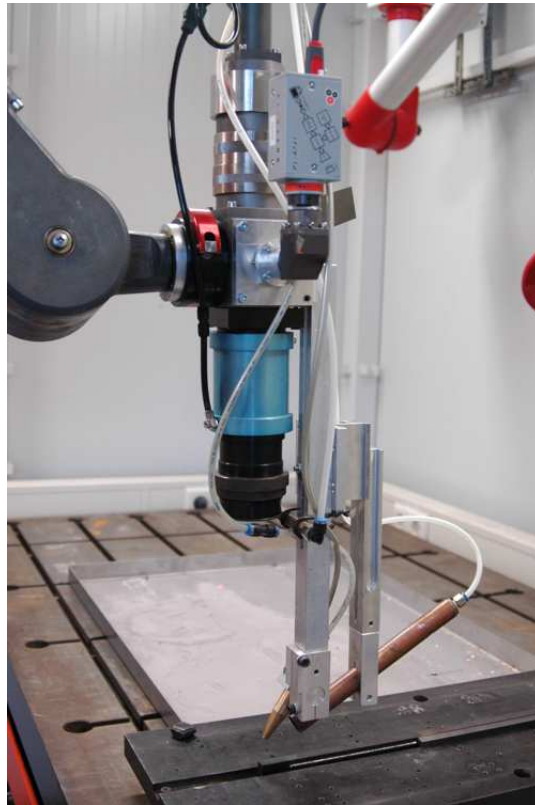


Figure 3.4: The laser cladding setup, showing the optical system as well as the powder nozzle mounted on a robot.

system. This system consists of a collimator lens which changes the diverging beam to a parallel beam. A focus lens then focusses the beam imaging the fiber end on the workpiece. A dichroic mirror is placed at an angle of 45° to the optical axis in the parallel beam. This mirror is transparent for the Nd:YAG laser radiation, but reflects visible light. In this way a camera or sensor system can "view" the cladding process coaxially with the laser beam. Usually the cladding area is covered with an inert gas to prevent oxidation and pore formation during cladding. Throughout this research work, mostly N_2 shielding gas is used. Figure 3.3 gives a schematic overview of the laser cladding setup.

3.3 Optical systems and energy distributions

Laser cladding, in contrast to laser cutting or welding, requires a large laser spot. This is often realized by working out of the focal plane. As a consequence, a far from uniform energy distribution is obtained. In this section, two optical systems are presented. The first system is a standard laser welding head, which is used for cladding by defocussing the laser beam. The second one is a newly developed system for producing large Top-hat energy distributions. The caustics of both systems are analyzed by means of a Primes focus measurement system (figure 3.5).

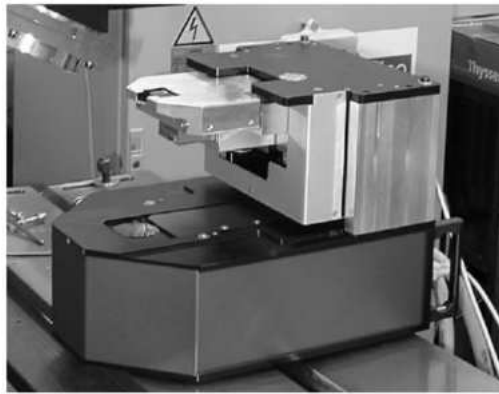


Figure 3.5: Photo of the Primes focus monitor system.

3.3.1 Standard optical system

A standard optical system developed for the laser welding process which is also used for cladding consists of a 200 mm collimator lens and a 200 mm focus lens. Since the laser fiber has a core diameter of 0.6 mm, an image with a Top-hat distribution of the same size (0.6 mm) is realized. Figure 3.6 shows a photo of this optical system. In the cladding experiments where a laser spot of 3 mm diameter is needed, it was realized by working out-of-focus. In principle, with this system a spot of 3 mm diameter can be obtained at about 16 mm below or above the focal plane. However, the energy distribution is far from the uniform distribution that is found in the focus. To investigate the intensity distribution in the working planes at varying distance from the focal plane, the laser beam caustics were analyzed using the Primes laser beam analyzer. The intensity distribution was mea-

sured at 15 parallel planes located at evenly distributed distances from the focal plane over an interval of 35 mm around the focal plane. At each plane a number of intensity measurements were made and averaged to reduce the measurement noise. In Figure 3.7 the intensity distribution for three of the



Figure 3.6: A standard 200 mm optical system.

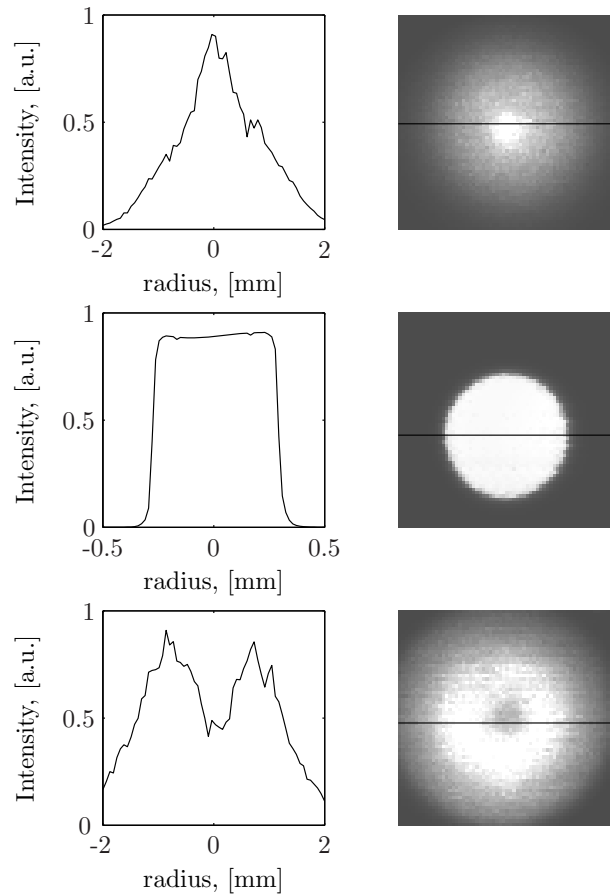


Figure 3.7: Intensity distributions of the standard optical system at 16 mm above, in, and 16 mm below the focal plane. (Note the different x-axis scales.)

measured planes are shown. In the focal plane, the energy is uniformly distributed. At 16 mm above the focal plane, the energy distribution is almost cone shaped. At 16 mm below the focal plane, a ring shape is observed. This asymmetry in the distribution above and below the focal plane might

be due to the effect of thermal-lensing. Apart from an axial focus shift, this causes some spherical aberration leading to an increase of the center intensity in the plane above the focus and a decrease of the center intensity below the focal plane resulting in the observed ring shape. This effect is schematically expressed in Figure 3.8. With increasing laser power, the ring shape energy distribution becomes more prominent. Due to higher energy densities on the lenses, the effect of thermal-lensing increases as thermal gradients trough the lenses in radial direction increases.

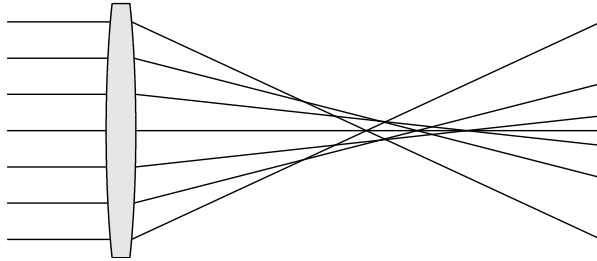


Figure 3.8: Spherical aberration. Light through the outer side of a positive lens focusses somewhat before light through the center of the lens

3.3.2 Tele-zoom optical system

The size of the laser spot on the workpiece (which is an image of the fiber exit) depends on the diameter of the fiber, the used collimator and focussing lens. For laser cladding, an energy distribution with a diameter of about 2 to 5 mm is commonly used. To obtain a Top-hat energy distribution on the workpiece with such diameters, an optical system was designed, developed and used throughout the work as described in this theses. A fiber image of 3 to 6 mm can be realized using a lens with a focal length of 1000 to 2000 mm. This is schematically expressed in Figure 3.9 on the left. Using such long focal lengths in combination with a manipulator for the optical system is not practical. To overcome this long focal lengths, a system is developed which combines the effective focal lengths and corresponding large images with a practical working distance. This is realized by first strongly focussing the beam (Figure 3.9 on the right). After a small beam is realized, a negative lens provides the same beam profile as the left picture. By adjusting the position of the negative lens along the main axis of the beam, the diameter of the laser spot can be changed. The design of the system

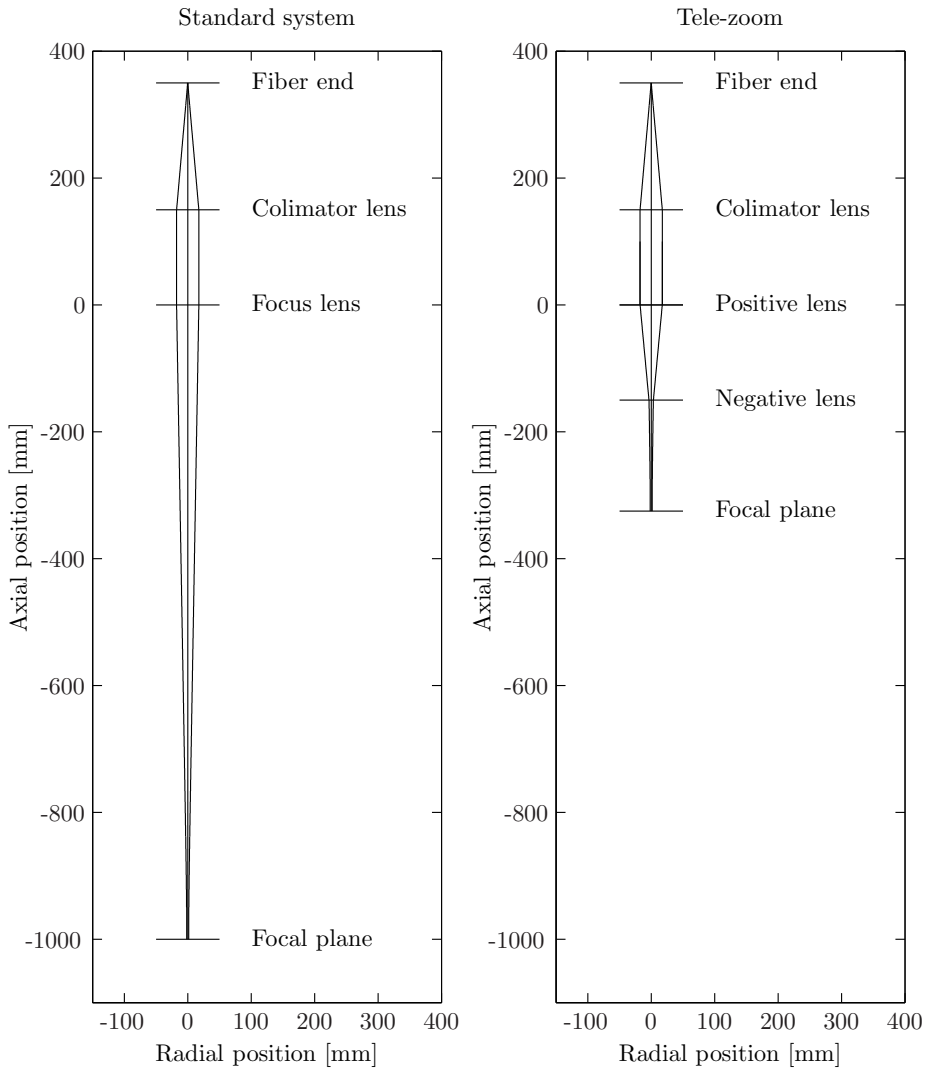


Figure 3.9: Obtaining a large spot using standard (left) and tele-zoom lens systems (right).

is based on commercially available lenses. Using the Opdesign ray-tracing software program, the design was optimized to give minimal aberrations at a wavelength of 1060 nm. Appendix A shows the ray pattern of the laser beam through the lenses. The lenses are mounted in a cylindrical system which is directly mounted on the standard optical system. Figure 3.10 on



Figure 3.10: Photo of the optical system.

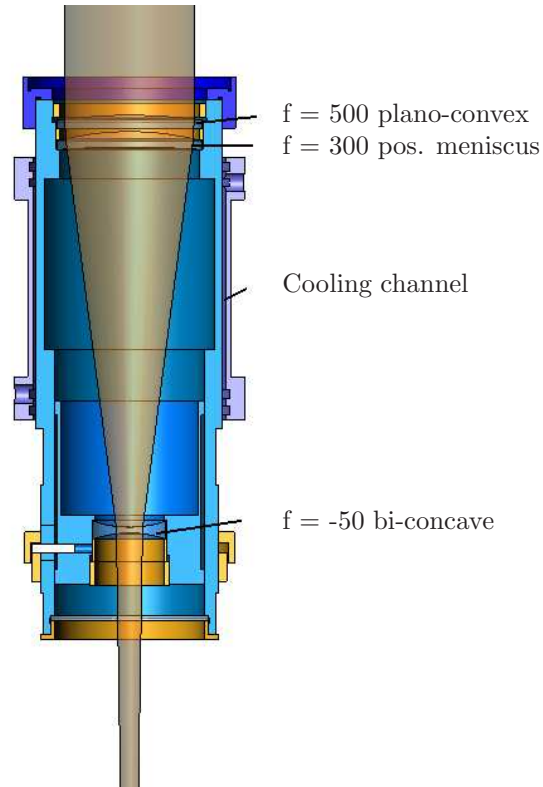


Figure 3.11: Schematic cross-section of the optical system.

the left shows a photograph of this system. On the right, a CAD drawing of this system is displayed. The housing consists of an inner part which holds the lenses which are water cooled by a cooling channel around the system. The position of the negative lens can be moved axially by means of two adjustment rings. At the bottom of the system a shielding window protects the lenses from spatter. The overall length of the system is 200 mm. The distance between the first positive and negative lens is 150 mm. An effective focal length from about 650 mm up to 2000 mm can be obtained (See Table 3.1. The Rayleigh length for a spot diameter of 3 mm is about 90 mm. Hence, small fluctuations in the order of millimeters will hardly influence the Top-hat distribution.

The caustic of the laser beam has been measured for several focal lengths. Figure 3.12 (left) shows the caustic (98% radius) for of the op-

Table 3.1: Focal lengths and working distances.

Focal length [mm]	Working distance [mm]	Spot diameter [mm]
666	250	2.0
1000	325	3.0
1500	430	4.5
2000	560	6.0

tical system set at a spot diameter of 3 mm (focal length was 1000 mm). In the focus plane, a Top-hat distributions is observed, with a radius of 1.5 mm. At 15 mm above the focal plane, a Gaussian distribution is observed, whereas 15 mm below the focal plane the distribution shows a combination of a Top-hat and a Gaussian profile. This asymmetry is caused by spherical aberration of the negative lens. However, since the practical working range is in the proximity of the focal plane small variations in the axial position will hardly disturb the Top-hat energy distribution. Figure 3.13 shows comparable distributions (in the focal plane) for spots of 3.0 mm and 4.5 mm in diameter. These energy distributions have been used in this research.

3.4 Powder delivery nozzle

The powder is transported to a nozzle by a 3 mm inner diameter tube. The nozzle has a central (\varnothing 2 mm) jet opening delivering a low speed powder stream surrounded by a concentric ring shaped gas nozzle. The ring nozzle delivers a high speed gas stream which converges the powder stream. Figure 3.14 shows a photograph of the nozzle as well as an additional shielding gas tube. Figure 3.15 shows the cross-section of the nozzle.

To investigate the speed and distribution of the particle jet as well as the influence of the convergence stream, a high speed camera was used. The powder nozzle is positioned at an angle of 45° . The camera is placed under the same angle. At a frame rate of 10,000 Hz, 25,000 frames of 256×128 pixels are recorded. Figure 3.17 shows two situations. In the first situation no convergence gas is used. The jet diameter increases. Also visible is the influence of the gravity, pulling the jet downwards. The second situation shows the jet when the convergence gas is turn on. In this case, the jet diameter is almost constant over a distance of about 15 mm . Also the influence of the gravity is significantly reduced. The particle speed

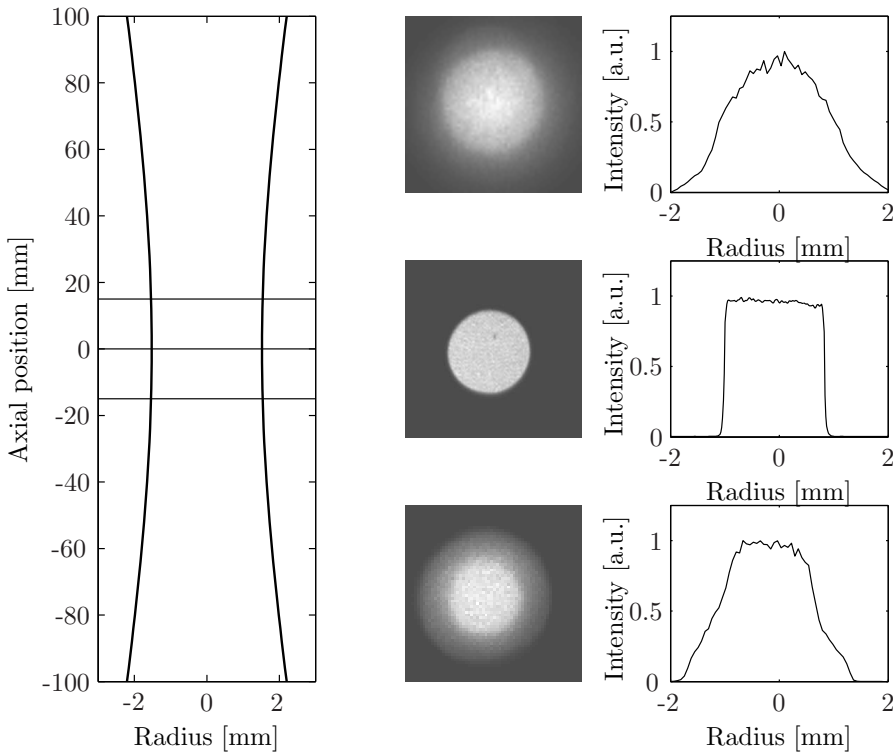


Figure 3.12: Caustic of the laser beam for a 3 mm diameter Top-hat spot (left), Intensity profiles at three locations (center) and cross-sectional intensity distributions (right).

distribution is obtained by image correlation of successive images. A small window (11×11 pixels) around each pixel is compared to the same window of the previous image. By convolving these two sub-images the shift in x- and y-direction giving the highest correlation is found. From this, the local speeds in two directions is obtained easily. This process is repeated for 1000 frames resulting in an average velocity in the x- and -y-directions. Figure 3.16 demonstrates the developed procedure. The developed matlab script for this purpose is presented in appendix B.

The measured particle speed distribution is shown in Figure 3.17. The use of a focusing gas is crucial to obtain a small powder jet. The particle speed is in the order of 1 m/s . The powder jet diameter is about 3 mm.

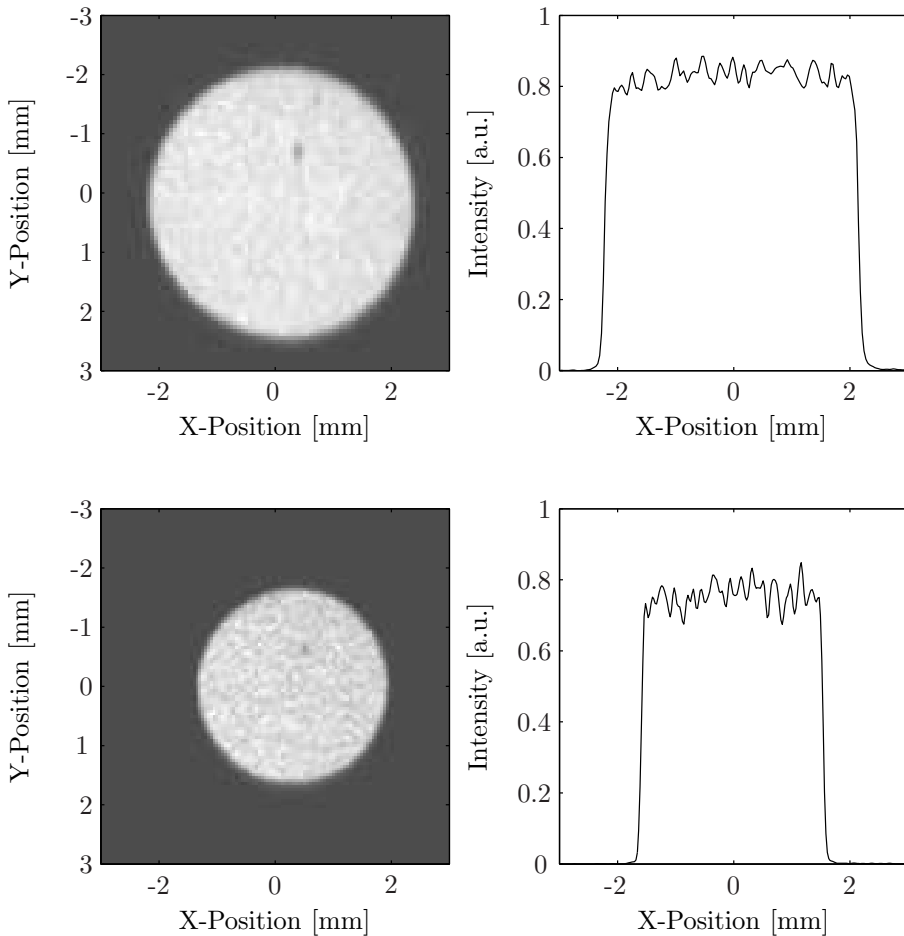


Figure 3.13: Energy distribution of the Top-hat spot. Top: 4.5 mm diameter. Bottom: 3.0 mm diameter.

3.5 Review and conclusions

In this chapter, details of the used experiential setup are described. The laser cladding setup uses a six-degree-of-freedom robot to manipulate the laser beam over the cladding substrate. The Nd:YAG laser beam is focused onto the substrate using a novel optical system. This system combines the advantages of a large Top-hat energy distribution with a practice working distance. The speed of the powder jet as delivered by the developed powder nozzle is analyzed. The average powder speed is about 1 m/s. The

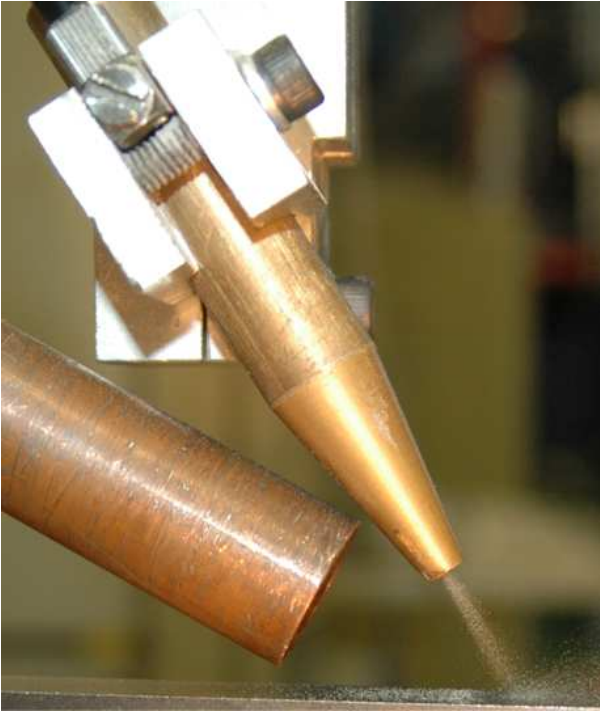


Figure 3.14: The powder nozzle and additional shielding gas tube.

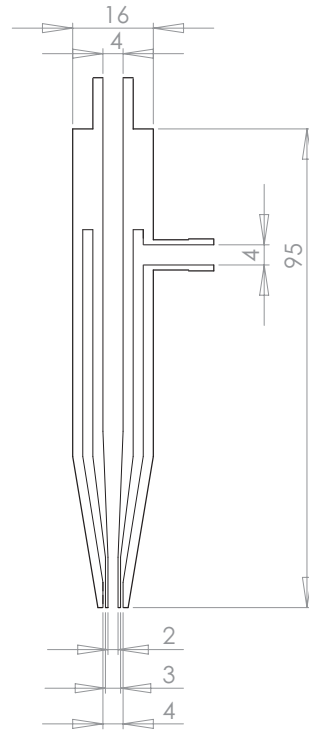


Figure 3.15: Drawing of the powder nozzle.

convergence gas highly decreases the divergence of the jet, enabling the powder jet to be fully directed into the melt pool.

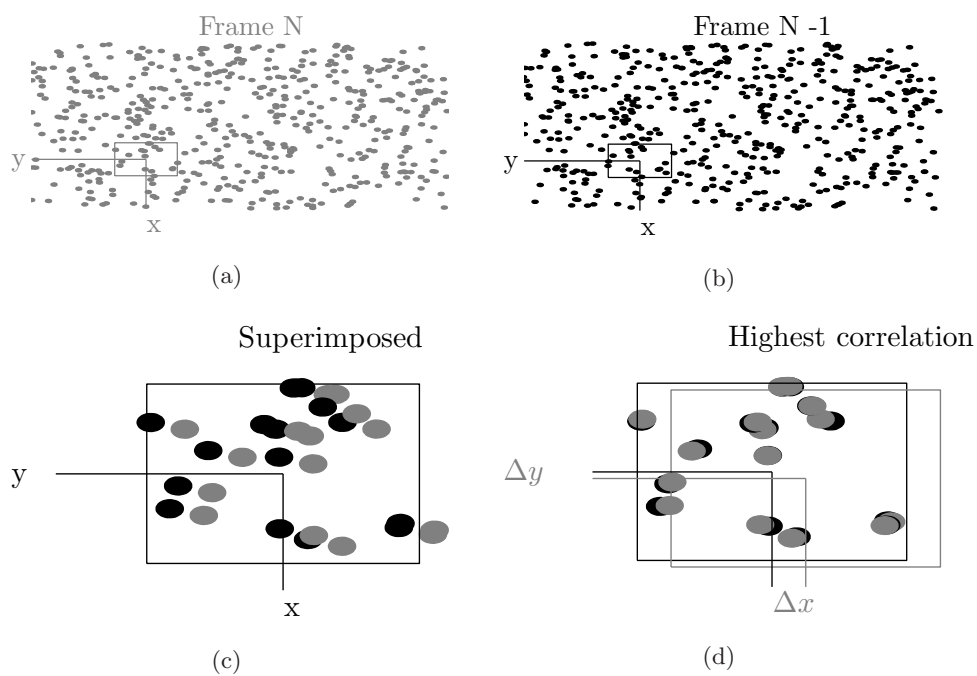


Figure 3.16: Procedure for determining the particle displacements.

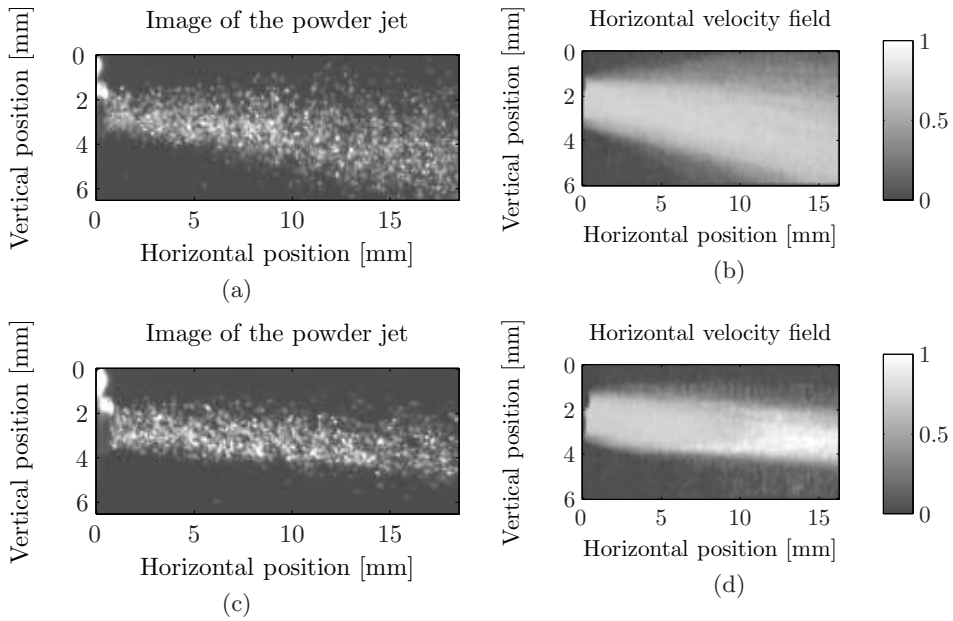


Figure 3.17: The powder jet as seen by a high speed camera (left) and the calculated particle velocity field (right) when the focusing gas is turned off (top) or turned on (bottom).

Chapter 4

Influence of process settings on the heat flow and clad characteristics

4.1 Introduction

Many parameters influence the laser cladding process. Figure 2.4 on page 12 gives an overview of some of these. Several parameters vary during the cladding process such as the substrate temperature and substrate geometry that is, its heat sink capacity. For instance, the temperature of the substrate can increase from room temperature up to several hundreds of degrees Celsius during the process. As a result, the dimensions of the melt pool and the dilution will increase. Changes in the geometry and consequently the heat sink capacity can be significant.

The dilution of the clad material is of main interest. A situation in which the base material surface just melts enough to get a good bonding between the clad and the base material, is preferred (see Figure 4.1.a). In practice, with a Gaussian laser intensity distribution overheating happens easily in the center of the clad track. This results in a deep melt pool or burn-in and dilution of the substrate material into the clad material. However, reduction of the power to avoid such a burn-in is not the solution since this results in a lack of bonding at the edges of the track. A typical burn-in shape, which can be expected in this situation is shown in Figure 4.1.b (e.g. [37, 36]). Sometimes a double-peaked burn-in has been observed (see Figure 4.1.c). This happened in a series of cladding experiments with Stellite 6

on a C45 substrate, using the standard optical system and working at 16 mm below the focal plane. As shown in Figure 3.7, in this configuration the intensity distribution has a ring shape.

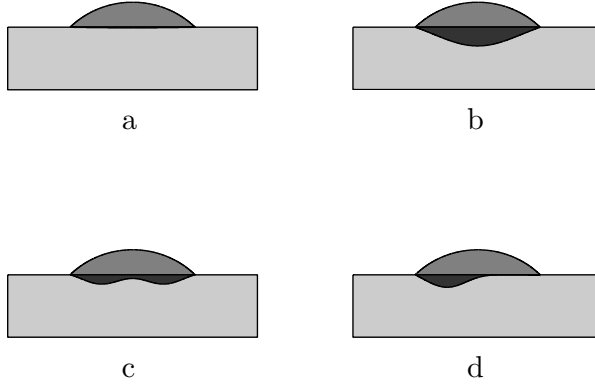


Figure 4.1: Typical burn-in shapes observed under specific conditions.

In this chapter, the heat flow and temperature in the melt pool area are discussed. First, the governing equations are presented in section 4.2. Next, the influence of the main process parameters on the clad characteristics, with an emphasis on the dilution, is discussed from a physical point of view. The influence of the main process settings on the heat flow behavior and the clad and melt pool dimensions is discussed in section 4.3. The influence of the energy input distribution, i.e. the clad surface boundary condition on the melt pool shape is discussed using experimental results in section 4.4. The chapter finalizes with conclusions in section 4.5.

4.2 Heat balance and boundary equation

The temperature distribution in the clad area follows from the heat balance and the boundary equations;

$$\rho c_p \frac{\partial T}{\partial t} + \rho c_p \vec{v} \cdot \nabla T = \nabla \cdot k \nabla T, \quad (4.1)$$

and

$$k \frac{\partial T}{\partial n} = q, \quad (4.2)$$

where k (thermal conductivity), c_p (heat capacity) and ρ (density) are material property coefficients, which can be functions of the temperature T and/or space. Quantity q is the heat flux at the surface and n is the inward normal of the surface. The velocity vector \vec{v} is the velocity of the material with respect to a coordinate system fixed to the laser beam. This velocity introduces a large convective heat flux. The heat equation does not include the effects of latent heat of fusion. It can be included by incorporating it in the heat capacity c_p over a small temperature range around the melt temperature. By doing so, the heat capacity becomes a strong function of the temperature.

Equation 4.2 shows that by increasing the input heat flux q into the material (i.e. higher laser power) the temperature gradients (and as such the temperature itself) increase. The heat dissipates into the substrate material due to conduction and convection. The heat conduction flux is a diffusion flux, effectively homogenizing the temperature. Heat convection takes place in the melt pool where external forces, such as the momentum of the powder particles, as well as surface tension cause a flow.

With increasing cladding speed, the convective term of equation 4.1 becomes more dominant. This effect can be expressed by the dimensionless Péclet number Pe , which gives the ratio between convective and conductive heat transport and is defined as:

$$Pe = \frac{L V_c \rho c_p}{k}. \quad (4.3)$$

Here, L is a characteristic length scale. A typical value for L is the spot diameter d_{spot} . Using representative values for the material properties, cladding speed and spot size as indicated below, give a Péclet number of about 7. This implies that for laser cladding the convective heat flow dominates the conductive heat transport.

$$\begin{aligned} L &= 3 \cdot 10^{-3} [m] \\ V &= 10 \cdot 10^{-3} [m/s] \\ \rho &= 8500 \cdot [kg/m^3] \\ c_p &= 400 [J/kg/K] \\ k &= 15 [W/m/K] \\ Pe &\approx 7 [], \end{aligned}$$

With increasing heat input (i.e. the laser power), the temperature and temperature gradients at the surface increase (Eq. 4.1). This in turn increases the conductive and convective heat flux. The temperature depends on the cladding speed as well. Therefore we define a specific heat input E_s :

$$E_s = \frac{P_l}{v_c}. \quad (4.4)$$

Increasing the specific heat input by raising the laser power increases both the convective and conductive heat fluxes. Increasing the specific heat input by decreasing the cladding speed will result in higher temperatures in the melt pool. This will raise the conductive heat flux in the melt pool resulting in larger melt pool dimensions. On the other hand, the convective heat flux decreases. As such, the Pe number reduces. By increasing the Péclet number and keeping the specific heat input constant (i.e. increasing the cladding speed and laser power simultaneously) the convective heat flux increases fast while the conductive heat flux increases only marginally. These effects are summarized in Table 4.1.

Table 4.1: Influence of the laser power P_l and cladding speed V_{clad} . \uparrow , \downarrow and \cdot indicates the value increases, decreases and remains unchanged respectively. $\uparrow\uparrow$ means large increase, \uparrow means small increase.

	E_s	Pe	(F_{conv})	(F_{cond})
$P_l \uparrow \quad V_{clad} \cdot$	$\uparrow\uparrow$	\cdot	$\uparrow\uparrow$	$\uparrow\uparrow$
$P_l \cdot \quad V_{clad} \uparrow$	\downarrow	\uparrow	\uparrow	\downarrow
$P_l \uparrow \quad V_{clad} \uparrow$	\cdot	\uparrow	$\uparrow\uparrow$	\uparrow

4.3 Influence of process settings

The influence of several of the process settings on the clad characteristics are presented in this section. The following parameters are discussed: cladding speed, laser power, laser spot diameter, powder jet and the initial substrate temperature. For a number of cases the effect of the Pe number and the specific heat input E_s will be discussed.

4.3.1 Influence of the cladding speed and laser power

The cladding speeds are typically 5 to 25 mm/s. When increasing the cladding speed, generally the laser power and powder feed rate are (linearly)

increased as well. With increasing cladding speed the heat losses due to conduction decrease. This implies that for the same specific heat input, the heat losses into the substrate reduce. As a consequence, the temperature and size of the melt pool will increase. Generally this leads to a higher powder efficiency as more powder is trapped into the melt pool. However, due to the increasing size of the melt pool, the dilution will also increase. To prevent excessive dilution the laser power should be increased less than proportional to the cladding speed.

By increasing only the cladding speed and keeping all other process settings unchanged, the specific heat input E_s reduces while the Pe number increases. This results in a smaller melt pool, lower temperatures and less heat losses into the substrate.

Increasing the laser power while keeping the other process settings unchanged, the specific heat input E_s increases. This results in larger melt pool dimensions and higher temperatures. The dilution will increase as well. These predicted trends based on the heat equation, E_s and Pe are found with experiments and simulations as presented in chapter 7.

4.3.2 Influence of the powder jet on the heat input distribution

The energy input on the clad surface depends on the laser beam distribution, the powder distribution and the shape of the clad layer. Figure 4.2 shows the heat input distribution on the clad surface as obtained from the FEM model which is described in chapter 6. On the front of the melt pool the laser power intensity is more reduced compared to the back of the melt pool due to the higher density of the powder jet. The powder jet is preheated by the laser beam which results in an additional energy contribution on the clad surface. The combined input of the laser beam and the powder jet shows that the input on the clad surface has shifted considerably to the back side.

Increasing the powder feed while keeping all other parameters fixed will lead to an increased clad height, as long as the laser power is sufficient to fully melt the powder. The heat input into the substrate will be shifted further backwards by an increased powder feed rate. The depth of the melt pool is only marginally affected by the powder feed rate. The dilution in general decreases with increasing powder feed rate.

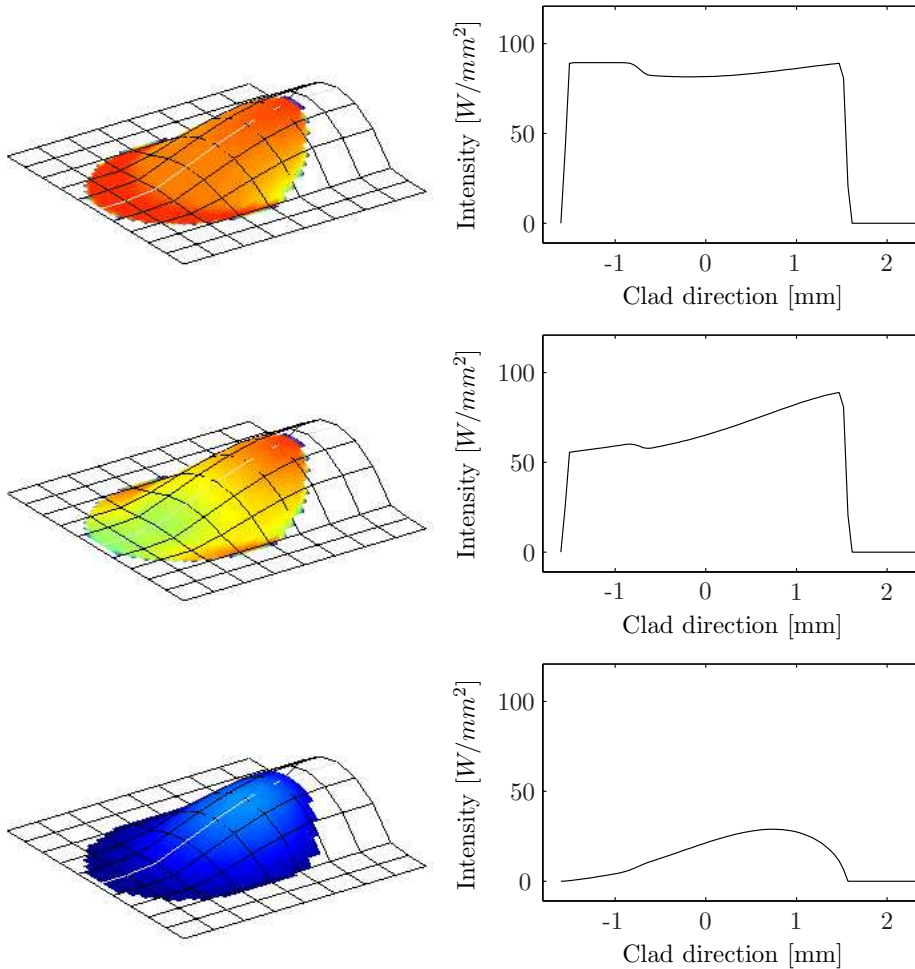


Figure 4.2: Contribution of the laser beam and powder jet to the heat input on the clad surface. On the left side surface plots of the distributions are shown. On the right side the intensity distributions along the center of the tracks are shown. From top to bottom; the laser beam, the powder jet and the combined contributions are shown.

4.3.3 Influence of the initial substrate temperature

The temperature of the substrate will generally be above room temperature because of the pre-heating effect of the previous tracks. Sometimes products are preheated to reduce the residual stresses and cracking. With unchanged

process settings this leads to larger melt pool dimensions, wider tracks and an increased dilution. Since the substrate temperature generally increases further as a function of the cladding time, the dilution will increase as well. To compensate for this temperature increase either the laser power should be reduced or the cladding speed increased to prevent excessive dilution.

4.4 Influence of the laser beam distribution

In this section the influence of the heat input from the laser beam into the melt pool area is discussed. First, the influence of the beam diameter will shortly be discussed. The energy distribution of the laser beam is discussed in more detail. Several cladding experiments demonstrate the effect of the energy distribution on the melt pool depth, i.e. the dilution levels.

4.4.1 Laser beam diameter

The width of the melt pool highly depends on the laser beam diameter. The laser radiation heats and melts the surface. The higher the laser power, the larger the melt pool will be. Since the center of the tracks have a higher energy input than the sides, there will be a conductive heat flux from the center to the sides of the track. At low laser powers, increasing the power will result in a fast increase of the melt pool width while a high laser powers, when the width of the pool is already close to the spot diameter, further increasing the power will only marginally increase the melt pool width due to a limited conductive heat flux.

Increasing the laser beam diameter has some advantages with respect to the production rate. First, a larger spot leads to a larger melt pool, assuming the laser power is sufficient. Secondly, a larger spot leads to a longer interaction time, allowing higher cladding speeds. In the third place thicker clad layers can be produced. Generally, the ratio between clad width and height is kept at about 0.3, to avoid inter-run porosity during cladding of successive tracks. Increasing the spot diameter results in a larger Pe number. This means that the conductive heat losses are less.

4.4.2 Laser beam energy distribution

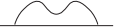

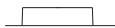
The energy distribution influences the depth of the melt pool and the dilution. A more or less uniform heat input over the width of a track is preferred. An increased heat input at the sides is even better to compensate for

the higher conduction heat losses. Unfortunately, in many cases [6, 5] the intensity distribution at the work plane is "Gaussian". This means that the centerline is overheated, whereas the sides remain cool. This happens even with a fiber coupled Nd:YAG system when it is out-of-focus. Using an analytical model, Römer [34] determined that for a flat temperature distribution, an energy distribution with higher intensities at the edges is required. This model does not take into account the effect of the powder jet through the beam nor melt flow. To study this effect, experiments were performed with two optical systems. The first system has a ring shape energy distribution as presented in section 3.3.1 on page 26. The second system has a 3 mm Top-hat distribution obtained with the new optical system as presented in section 3.3.2 on page 28.

Experiments

Single tracks were produced with three energy distributions. Two series were produced with the standard optical system, working at 16 mm below and above the focal plane. As clad material, Stellite 6 was used. The last series was produced using the optical zoom system in the focal plane with Stellite 12. All laser spots were 3 mm in diameter. Table 4.2 shows the settings for the performed experiments. Also some tracks were produced with powder feed from the side instead from the front. In Figure 4.3 cross

Table 4.2: Process settings.

	Standard optics		Zoom optics
Work piece position	16 mm above focal plane	16 mm below focal plane	In focal plane
Cladding speed [mm/s]	10, 15, 20	10, 15, 20	10, 15
Specific power [J/mm]	100, 120, 150	120	135 / 123
specific powder [mg/mm]	10	10	14.5
Power distribution			

sections are shown in which the melt interface and the extent of the HAZ can be seen. In the left column, a double-peaked burn-in can be recognized, whereas in the center column images, the burn-in is deeper at the center. The images on the right side show that with a Top-hat energy distribution the burn-in is less, resulting in a more uniform melt pool depth. Note that the process settings are slightly different in the latter experiments. Figure 4.4 shows a cross-section of a clad track produced with the ring

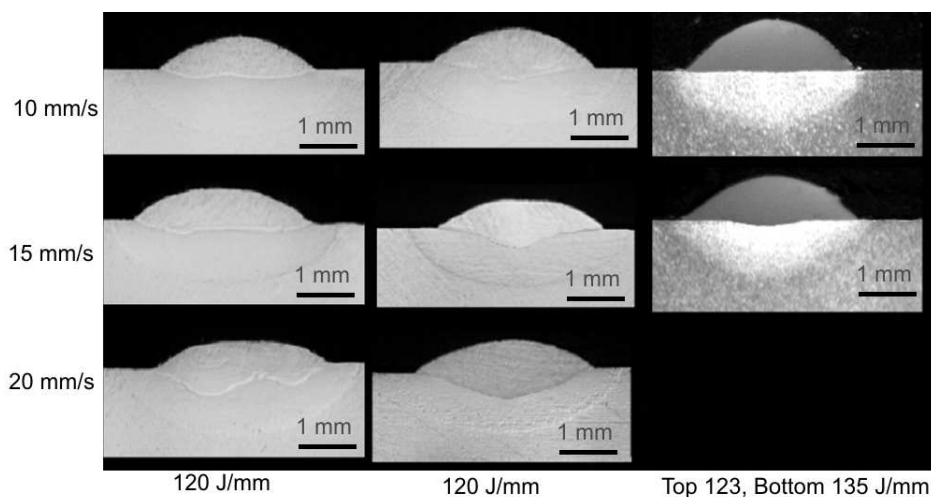


Figure 4.3: Cross sections of eight clad layers, produced with different laser beam energy distributions. Left: ring shape. Center: peak shaped. Right: Top-hat.

shape energy distribution at 100 J/mm. Although the burn-in is reduced due to the lower heat input, two recirculation flow patterns can clearly be recognized. Another type of burn-in is shown in Figure 4.5 in which case the powder supply was transverse to the cladding direction (from the right).

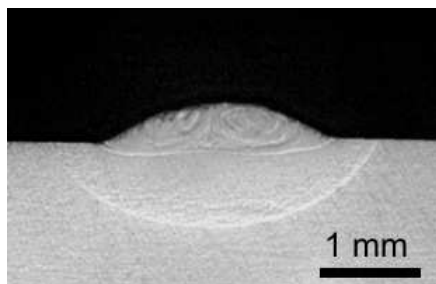


Figure 4.4: Cross section of a track, produced at a process speed of 20 mm/sec, specific power of 100 J/mm and specific powder mass rate of 10 mg/mm.

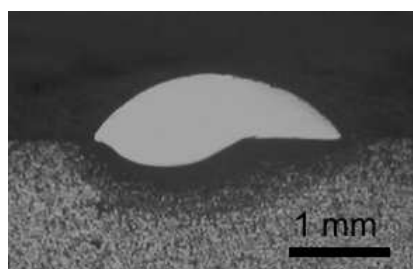


Figure 4.5: Cross section of a track with lateral powder supply from the right, showing a one sided burn-in shape. Process speed: 10 mm/sec; specific power: 110 J/mm; specific powder mass rate: 12.5 mg/mm.

Discussion

It is clear that depending on the process settings, especially the energy distribution, large differences in the melt pool shape can be observed. The possible cause of these melt pool shapes are discussed.

The cross-sections in the first two columns of Figure 4.3 show increasing dilution with the cladding speed. This is due to the fact that the specific energy is kept constant. The relative conductive heat losses decrease with increasing velocity, resulting in larger melt pool dimensions.

The burn-in shape found in the experiments with the ring shape distribution has two maxima, which become more pronounced at higher speed. This is because to maintain the constant specific power (J/mm) with increasing cladding speed (mm/s) the absolute power (W) has been increased. This coincides with the observation that precisely for the higher power levels, the intensity distribution deforms increasingly from a Gaussian into a ring shaped distribution. An immediate conclusion that this intensity distribution is the direct cause of the double-peaked burn-in shape is premature. As Figure 4.4 shows, the convective heat transport by melt flow may also play an important role. In this figure, two recirculation patterns which correspond with the burn-in peaks can be recognized.

It is known from literature that the driving force for this melt flow patterns is the Marangoni force which is directly related to temperature gradients in the melt pool surface. Limmaneevichitr et al. [38] investigated the effect of Marangoni force on the flow in a melt pool. They show that the resulting flow causes a recirculation pattern which can explain the double-peaked burn-in shape. Apart from a material dependency, the Marangoni forces depend on the tangential surface temperature gradient. This underlines the importance of the melt pool surface temperature and therefore the laser intensity distribution. Another driving force, which has a significant influence on the melt flow pattern, is the force due to the powder flow jet which hits the melt pool surface. This force is a combination of the contributions from the pressure and frictional forces by the gas flow, and the momentum transfer of the powder particles.

The forces exerted by the powder flow may be stronger than the Marangoni forces. The asymmetrical burn-in shown in Figure 4.5 follows from the powder flow which is fed from the right side (transverse to the cladding direction) contrary to the other experiments where the powder is fed from the front.

Heat input

The power intensity distribution and the corresponding heat input has a large influence on the melt pool depth. The heat input is obtained by integrating the intensity distribution on the surface over time:

$$\begin{aligned} H(y) &= \int I_s(y, t) dt \\ &= \int \frac{I_p(y, x)}{V_c} dx. \end{aligned} \quad (4.5)$$

Here, $H(y)$ is the heat input along the y -direction (transverse to cladding direction). Quantity $I_s(y, t)$ is the power intensity on the surface as function of the y -direction and time. Similarly $I_p(y, x)$ is the laser beam intensity distribution and V_c is the cladding speed. The solution for the ring shape energy distribution is shown in Figure 4.6.

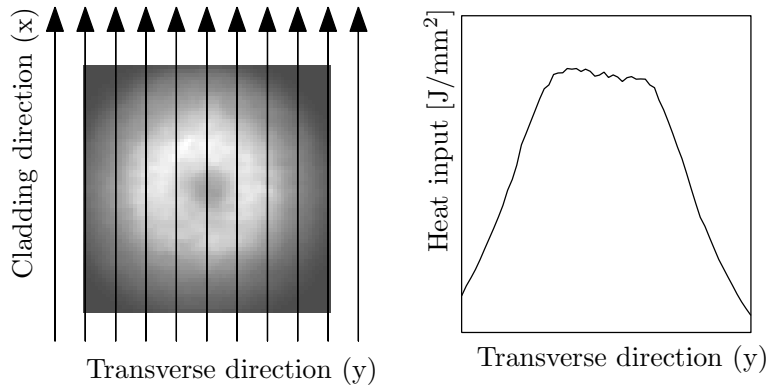


Figure 4.6: The heat input on the surface can be obtained by integrating the laser beam energy distribution along the cladding direction.

In Figure 4.7 the cross section of the intensity profile is shown (left) together with the heat input (right). The first and second rows show the profiles for the out-of-focus work positions as shown in figure 3.7. The bottom row shows the results for the in-focus zoom optics, which had a Top-hat distribution. It should be noticed that the ring shaped intensity profile turns out to be quite uniform over the central part of the track. The power distribution of Top-hat distribution shows a semi-elliptical shape, with a maximum power input on the centerline.

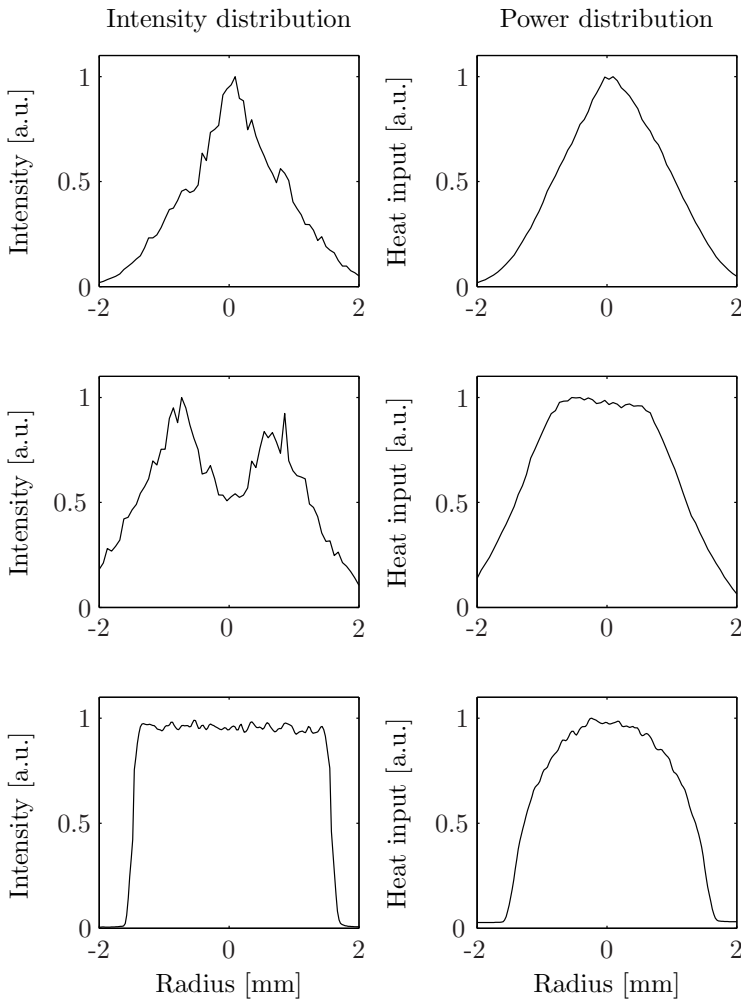


Figure 4.7: Intensity distribution in a cross section (left column) and the corresponding heat input as function of the transverse position on the clad track (right column). Rows: above focus (top), below focus (middle) for the 200 mm focus lens, and in-focus (bottom) using the zoom system.

The distribution of the powder flow plays also an important role in the energy distribution. The powder distribution is more dense at its centerline and less dense towards the sides. Also a clad track is higher in the center, having a semi-elliptical shape. This implies that more power is required at the centerline of the track.

4.5 Review and conclusions

In the above sections, the influence of the main process variables on the clad track characteristics were discussed. The melt pool, dilution and clad track geometry increase with increasing laser power or initial substrate temperature. Increasing the cladding speed has a decreasing effect on all these characteristics.

The influence of the laser beam intensity profile on the clad shape, in particular the burn-in shape, is evident. However, the presence of melt recirculation flow patterns may have a larger influence. These flow patterns appear to be driven more by the momentum transfer from the powder jet than by Marangoni forces alone.

A Gaussian intensity distribution is least preferable as it causes either a burn-in in the center of the clad track, or insufficient heating at the sides of the track. Clad tracks produced by the ring distribution show a double-peaked burn-in. The burn-in depth is minimal and most constant along the transverse direction when a laser beam with a top-hat distribution is used.

Chapter 5

Monitoring system

5.1 Introduction

To monitor the laser cladding process several sensors are available. Römer [34] used the temperature of the melt pool obtained by a pyrometer to control the temperature by adjusting the laser power. He also used a CCD camera to control the area of the melt pool. Toyserkani [35, 18] used a CCD camera to control the height of the clad layer in real-time. A camera system offers two-dimensional information of the cladding process and has an advantage over photodiode detectors, since the latter only provides information of the average radiation within its field of view. A camera based monitoring system has been developed as part of this research work, delivering in-situ images of the cladding process, especially the melt pool zone.

In this chapter, the development of the camera based monitoring system is presented. First, the radiation as emitted and reflected by the melt pool area and the optical path from the melt pool to the camera is discussed. The applied optical filtering and the consequences of the optical path on the detectability of the melt pool is presented in section 5.2. The digital image processing technique which is developed to determine the melt pool dimensions is presented in section 5.3. The accuracy of the sensor system and the influence of the clad material (properties) are analyzed and discussed in the sections 5.4 and 5.5. Finally, the conclusions are presented in section 5.6.

5.2 Optical path

Light from the cladding area consisting of heat radiation, reflected ambient light and laser radiation, passes upwards through the laser focussing lens (see Figure 5.1). Then it is deflected by a dichroic mirror to the camera optics consisting of a diaphragm, an optical filter and the camera focus lens. It is required that the spacial and temporal resolution of the camera are

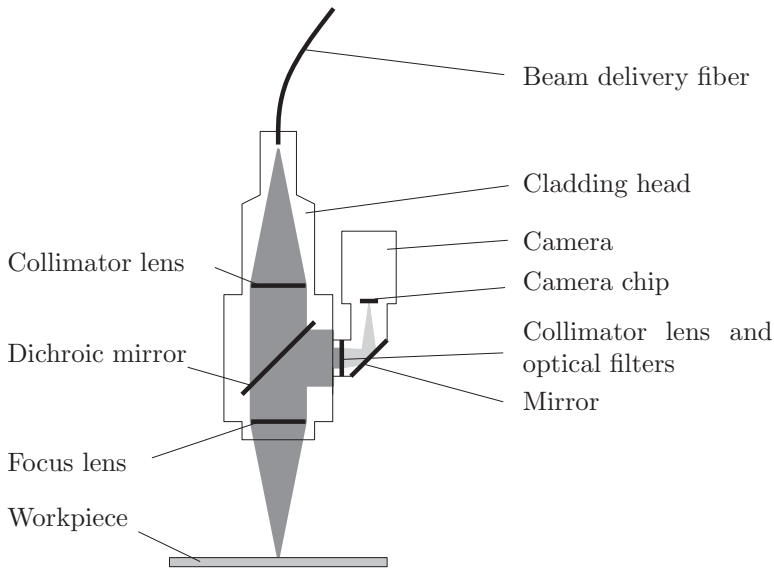


Figure 5.1: Schematic overview of the monitoring system.

adjustable and that the sensor chip is insensitive for blooming. Therefore, a CMOS camera is used instead of a CCD camera. In this work, a PixeLINK PL-A741 monochrome CMOS camera is used, which has an IBIS5-A-1300 CMOS chip with 1024x1024 pixels, sensitive within a wavelength range of 400 to 1000 nm and a dynamic range of about 42 dB in 8-bit grayscale mode (Figure 5.2). The spectral response of this camera is shown in figure 5.5. The images from the camera are transferred to a computer by its IEEE 1394 interface. The camera chip is illuminated by the radiation from the process zone, i.e. melt pool as well as the reflected laser radiation. To obtain information about the melt pool shape, reflected laser radiation is suppressed by placing an optical filter in front of the camera chip (Thorlabs FES0950). The transmittance of this filter is analyzed in section 5.2.2.

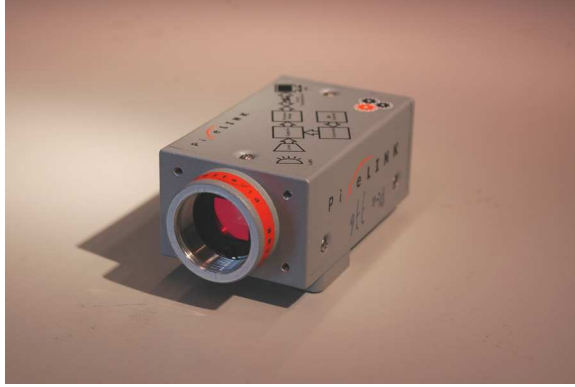


Figure 5.2: Photo of the PixeLINK PL-A741 CMOS camera.

5.2.1 Process radiation

The spectral radiance (E_λ^b) of a black body at a temperature T per unit area is described by Planck's law as;

$$E_\lambda^b = \frac{8\pi hc^2}{\lambda^5 (e^{\frac{hc}{\lambda kT}} - 1)}, \quad (5.1)$$

where

$$\begin{aligned} E_\lambda^b &= \text{radiant intensity [W/m}^3\text{]} \\ \lambda &= \text{wavelength [m]} \\ T &= \text{temperature [K]} \\ h &= 6.63 \cdot 10^{-34} \text{ Js, Planck's constant} \\ c &= 3 \cdot 10^8 \text{ m/s, speed of light} \\ K &= 1.38 \cdot 10^{-23} \text{ J/K, Boltzman's constant} \end{aligned}$$

An increase of the temperature corresponds to an increase of the spectral radiance. Wien's displacement law gives the wavelength where the radiation has its maximum:

$$\lambda_m = \frac{hc}{5KT} \approx \frac{2.87 \cdot 10^{-3}}{T} \text{ [m]} \quad (5.2)$$

The spectral radiance of a non-black body is:

$$E_\lambda^{real} = \varepsilon \cdot E_\lambda^b \quad \varepsilon \in [0, 1] \quad (5.3)$$

The emissive power or irradiance I of a black body is the integral of equation 5.1 over all wavelengths and is known as the Stefan-Boltzmann law:

$$I = \sigma T^4, \quad (5.4)$$

$$\sigma = \frac{2\pi^5 k^4}{15c^2 h^3} \approx 5.67 \times 10^{-8} \text{Wm}^{-2}\text{K}^{-4}$$

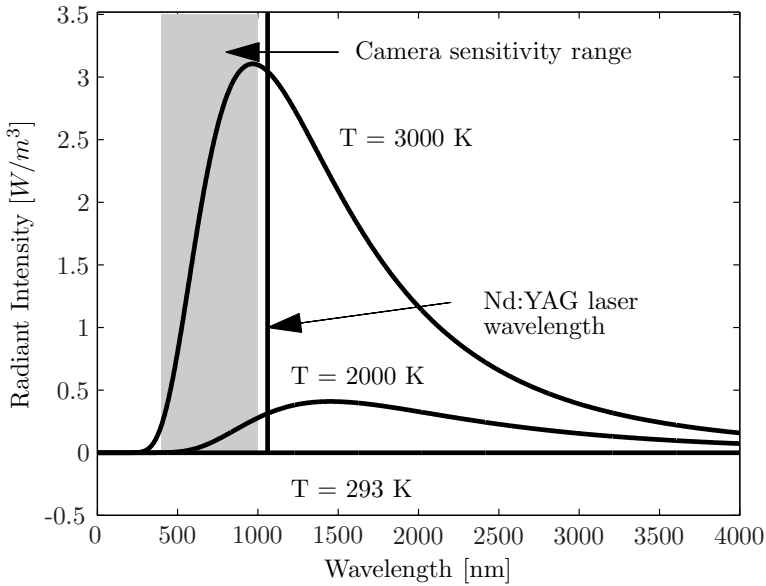


Figure 5.3: Plank curve for two temperatures and the sensitivity area of the camera.

The melt pool has a temperature of approximately 2000 – 3000 K. The maximum radiance at such temperatures are in the near infrared region ($\lambda_m \approx 1\mu\text{m}$). Figure 5.3 shows the Plank curve for 2000 and 3000 K. Also indicated are the sensitivity range of the camera and the laser wavelength. As this figure shows, only a small fraction of the light is detected by the camera. Also the optical components like lenses and filters influence the fraction of the emitted light which reaches the camera.

5.2.2 Spectroscopic analysis

The spectroscopic measurements of the melt pool emissions were performed by a calibrated HR4000 Ocean Optics spectrometer with a 0.2 mm optical

fiber and a small quartz lens (Figure 5.4). This spectrometer is equipped with a 3648-element CCD array and a grating with 300 lines/mm, which is sensitive in a wavelength range of 200 to 1050 nm with an optical resolution of 1 nm.



Figure 5.4: Photo of the Ocean Optics HR4000 spectroscopy with measurement fiber.

Optical components

The spectrometer was first used to measure the transmittance of the optical system. Therefore the spectrometer was placed at the camera position. The radiation through the optical system was measured using a calibrated light source. Also the radiation from the light source itself was measured. The transmittance of the optical system is the ratio of both measurements. In the same way the transmittance of the Thorlabs FES0950 filter was determined. Figure 5.5 shows the results as well as the spectral response of the camera. The filter has a transmission range of 450 to 950 nm.

Process radiation

During the measurements of the melt pool radiation, the spectrometer was placed at the camera position. The wide band-pass Thorlabs FES0950 filter was in front of the fiber to protect the spectroscopy from reflected Nd:YAG radiation. The cladding experiments were performed using Stellite 12 powder on a C45 steel substrate with a laser power of 1000 W.

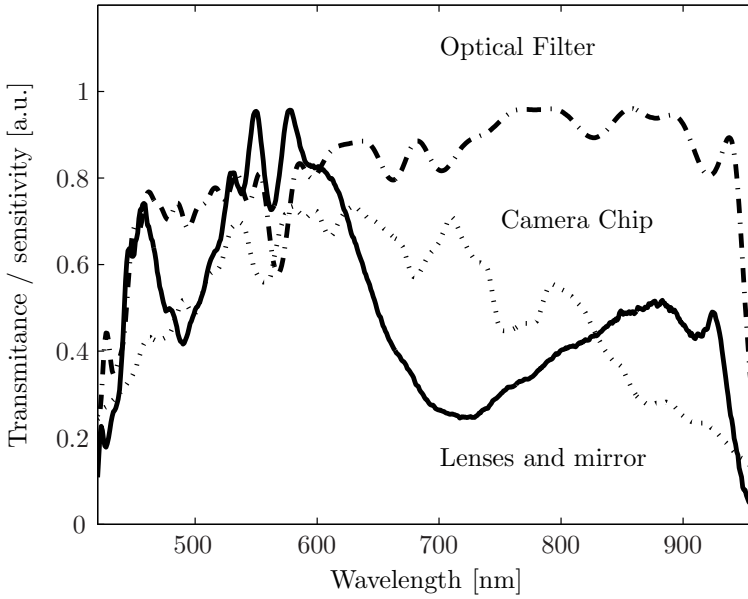


Figure 5.5: Spectral response of the PixeLINK PL-A741 CMOS camera (Courtesy of PixeLINK) as well as the transmittance of the optical filter and the optical system.

Since the transmittance of all components are known, the measured process radiations could be corrected accordingly. Figure 5.6 shows the spectral distribution of the radiation from the melt pool as measured by the spectrometer directly, as well as the resulting distribution on the camera chip. The real process intensity distribution is obtained by correcting. This data is obtained from a cladding experiment with Stellite 12. Other materials show a (slightly) different spectral distribution. The intensity distribution of the real process emission has a maximum at a wavelength of 900 nm, which accordance to Wien's law, corresponds to a temperature of 3200 K.

5.2.3 Intensity as function of the temperature

As discussed in section 5.2.1, the camera chip collects only a small fraction of the radiation from the melt pool. From the spectroscopic measurements, the transmittance of the optical system has been determined. The response of the camera chip is known as well. Using this spectral data, the irradiation on a camera image pixel as function of the temperature can

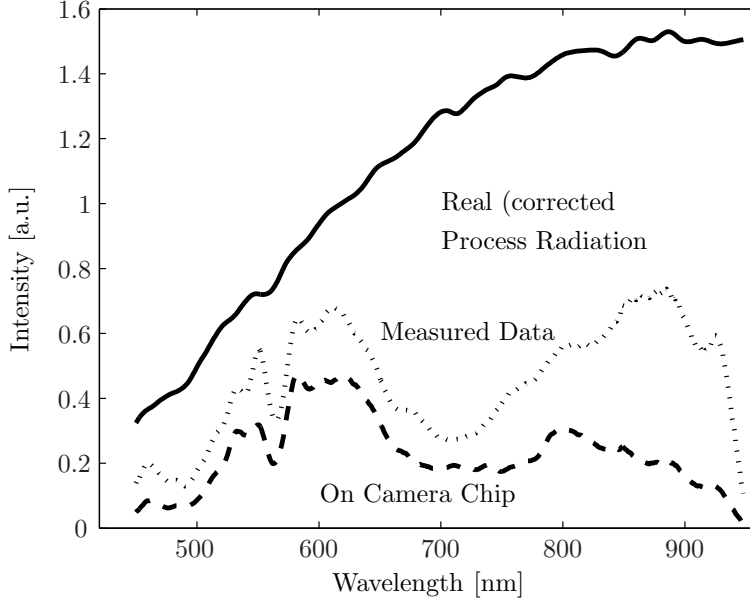


Figure 5.6: Spectral intensity distribution of the melt pool zone.

be determined by integrating Plank's law with respect to the wavelength, taking into account the optical losses and the camera response. Figure 5.7 shows the resulting relation between camera intensity and temperature. As can be seen from this figure, an increase in temperature from 1000 to 3500 K corresponds to range of almost 120 dB. Because the dynamic range of the camera is only 42 dB, it is impossible cover the whole range in one image. The camera's gain and exposure time are generally chosen such that the melt temperature lies around the center of the camera's dynamic range. This way, a temperature range of about 700 K around the melt temperature can be recorded. In the digital images the lower T_{min} and higher T_{max} temperatures correspond with a grayscale value of 2 and 255 respectively.

5.3 Image processing

The melt pool dimensions are determined real-time from the digital images of the melt pool using dedicated software that was written for this purpose. Images from the melt pool are transferred from the camera to the computer

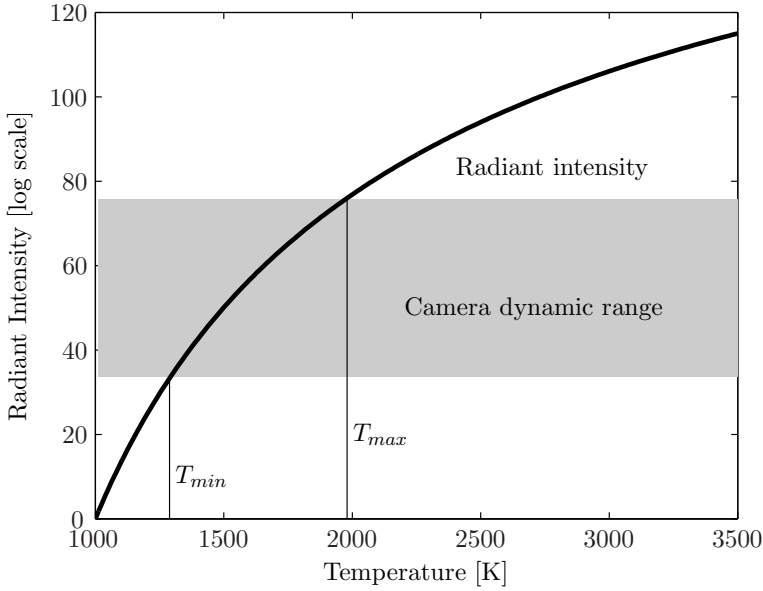


Figure 5.7: Relation between the temperature and the image intensity.

at a frame rate of about 200 Hz. The determination of the melt pool dimensions is explained in the following section.

A camera image can be interpreted as an $M \times N$ matrix $I_{i,j}$, where i, j indicate the position along the main axes of the image and $0 \leq I_{i,j} \leq 255$ the gray value of the pixel at position i, j . The images are first filtered with a 3×3 Point Spread Function (PSF), as expressed by equation 5.5.

$$G_{i,j} = \sum_{k=-1}^1 \sum_{l=-1}^1 H_{k,l} I_{i-k,j-l}. \quad (5.5)$$

Here $H_{k,l}$ is an approximation of the 2-dimensional Gauss function with $\sigma_x^2 = \sigma_y^2 = 0.7\Delta^2$, in which Δ is the distance between two pixels. This filtering removes single bright pixels which may be caused by hot particles. Secondly, the image is converted into a black and white image by means of a user defined threshold value $T_{threshold}$.

$$B_{i,j} = (G_{i,j} \geq T_{threshold}), \quad (5.6)$$

where B is the resulting binary image. The threshold value $T_{threshold}$ is selected such that it corresponds to the melt pool boundary, i.e. the melting temperature. This value is determined by a calibration procedure as

described in section 5.5. Values for several materials are given in Table 5.3. The third step involves the extraction of melt pool features such as orientation, length, width and area. After examining hundreds of images, an ellipse was found as the best approximation of the melt pool shape. The dimensions of such an ellipse are determined by the first and second order moments of area. The moments of order $p + q$, $\mu_{p,q}$ around the centers of

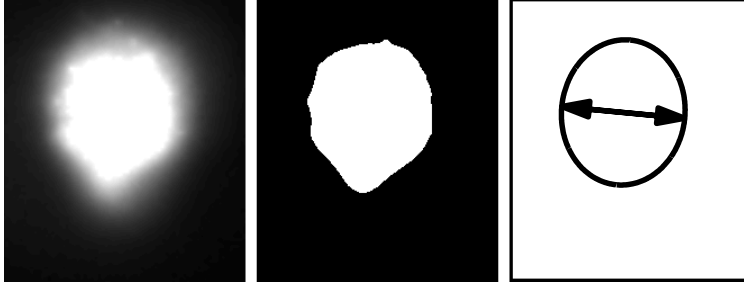


Figure 5.8: Left: original image, Center: lowpass filtered and thresholded image, Right: fitted ellipse.

gravity of the image are defined as:

$$\mu_{p,q} = \sum_{i=0}^{M-1} \sum_{j=0}^{N-1} (i - \bar{i})^p (j - \bar{j})^q B_{i,j} \quad (5.7)$$

where \bar{i} and \bar{j} are given by:

$$\begin{aligned} A &= \sum_{i=0}^{M-1} \sum_{j=0}^{N-1} B_{i,j} \\ \bar{i} &= \sum_{i=0}^{M-1} \sum_{j=0}^{N-1} i B_{i,j} / A, \\ \bar{j} &= \sum_{i=0}^{M-1} \sum_{j=0}^{N-1} j B_{i,j} / A. \end{aligned} \quad (5.8)$$

To obtain the melt pool width and length, first the central moments are used to calculate the principal moments:

$$\begin{bmatrix} \lambda_{max} \\ \lambda_{min} \end{bmatrix} = eig \begin{bmatrix} \mu_{2,0}, \mu_{1,1} \\ \mu_{1,1}, \mu_{0,2} \end{bmatrix}, \quad (5.9)$$

where λ_{max} and λ_{min} are the principal moments, $\mu_{2,0}$ and $\mu_{0,2}$ are the variances in i- and j-direction respectively, and $\mu_{1,1}$ is the covariance. The length and width of an ellipse can be expressed as function of their main variances as:

$$\begin{aligned}
 \mathbf{L} &= 2 * R_{max} \\
 \mathbf{W} &= 2 * R_{min} \\
 \mathbf{A} &= \pi R_{min} R_{max} \\
 Var_{max} = \lambda_{max} &= \frac{1}{4} \pi R_{min} R_{max}^3 \\
 Var_{min} = \lambda_{min} &= \frac{1}{4} \pi R_{min}^3 R_{max}
 \end{aligned} \tag{5.10}$$

where R_{max} and R_{min} are the two radii of an ellipse. The area \mathbf{A}_m , length \mathbf{L}_m , width \mathbf{W}_m and orientation θ_m of the melt pool can therefore be obtained as:

$$\begin{aligned}
 \mathbf{A}_m &= \mu_{0,0} \\
 \mathbf{L}_m &= 4 * \sqrt{\lambda_{max} / \mathbf{A}_m} \\
 \mathbf{W}_m &= 4 * \sqrt{\lambda_{min} / \mathbf{A}_m} \\
 \theta_m &= \arctan \left(\frac{\lambda_{max} - \mu_{2,0}}{\mu_{1,1}} \right),
 \end{aligned} \tag{5.11}$$

with \mathbf{A}_m , \mathbf{L}_m and \mathbf{W}_m in pixel units, and θ_m in radians. The values of the detected melt pool features are translated from pixel numbers into real units by multiplying with the image scale.

5.3.1 Processing time

The image processing method as described above is implemented in C++. The code is optimized for speed resulting in a typical processing time of 0.4 ms. Typical integration (exposure) times as used for obtaining an image are 1.0 ms. Transferring the image data from the camera to the computer by means of the IEEE 1394 interface, is theoretically limited to 400 Mbps. In practice, a speed of about 250 Mbps of pixel data is realized. This means, that transporting an image with dimensions of 200×200 pixels requires about 1.2 ms. Adding half the exposure, transfer and computing time gives a typical average delay of about 2.1 ms. Figure 5.9 graphically expresses the time line for this process. The time constant for the laser cladding

process is given by:

$$\begin{aligned}\tau &= \frac{R^2}{4 a} \\ a &= \frac{k}{\rho c_p}.\end{aligned}\tag{5.12}$$

Here a , k , c_p and ρ are the heat diffusion coefficient, the thermal conductivity, the heat capacity and the density. The spot radius is about 3 mm. Using the material properties of Stellite 12 (see Table 5.1), the time constant τ is 530 ms. Compared to this number, the total image processing time is fast and can be considered real-time.

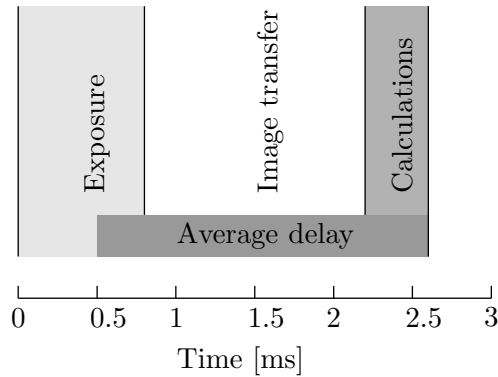


Figure 5.9: Graphical representation of the processing times.

5.4 Accuracy of the measurements

Due to the process dynamics, the measured dimensions will fluctuate over time. To investigate these fluctuations, an experiment was performed using a constant cladding speed, laser power and powder feed rate of 10 mm/s, 1100 W and 21.4 mg/mm respectively. 2000 images were recorded. Figure 5.10 shows the results. The standard deviations are 53×10^{-3} mm and 116×10^{-3} mm for the width and length respectively, which corresponds to about 2 % for both the signals.

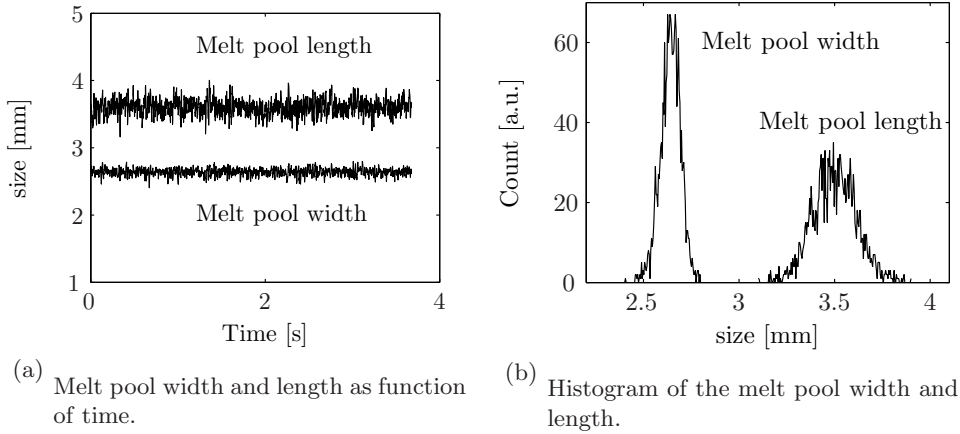


Figure 5.10: Fluctuation of the melt pool width and length as determined from the images obtained by the camera.

5.5 Powder material and required threshold level

The calculated melt pool dimensions depend on the threshold value $T_{threshold}$ which discriminates the area below and above the melt temperature. This value depends on the emission of the melt pool. To investigate the influence of the clad powder material on the corresponding $T_{threshold}$ different powders were tested. With each powder a single track was produced on a steel bar with a diameter of 35 mm. The specific powder flow, cladding speed and laser power were set to $30 \text{ mm}^3/\text{s}$, 10 mm/s , and 1500 W . The physical and chemical composition of these materials are summarized in Table 5.1 and 5.2.

Table 5.1: Material properties of the investigated powders at room temperature.

	Melt Temperature [K]	Conductivity [W/m/K]	Specific Heat [J/Kg/K]	Density [Kg/m ³]
Stellite 12	1528 - 1614	14.8	408	8560
Metco 42c	1755	20	460	7800
Ultimet	1605 - 1627	12.3	456	8470
Metco 51NS	1313	N.A.	N.A.	3700
ALSi12	847 - 855	121	963	2660
Delcrome 200	1528 - 1581	11.3	N.A.	7590

The width of each track was measured at 5 locations along the track

Table 5.2: Chemical composition of the investigated powders in wt %.

	Fe	C	Co	Cr	W	Si	Ni	Mn	Mo	Al	Cu	Mg	Zn
Stellite 12		1.85	Bal	29.5	8.5	1.5							
Metco 42c	Bal	0.2		15.9		0.7	2.43	0.1					
Ultimet	3	0.06	Bal	26	2	0.3	9	0.8	5				
Metco 51NS	1									10	Bal		
ALSi12	0.6					12		0.15		Bal	0.05	0.05	0.2
Delcrome 200	Bal	0.8		4	6				5				

by a microscope. During each cladding experiment images of the melt pool were recorded at a frame rate of 30 Hz resulting in a grayscale image sequence of about 400 frames. The melt pool width is calculated for all the intensity values (possible threshold levels) based on these 400 frames and compared with the actual clad width. Figure 5.11 shows the data of Stellite 12 powder. The real threshold level is the value where the actual and calculated widths cross. In this example the threshold level is 142. Table 5.3 shows the threshold values as determined by the above procedure

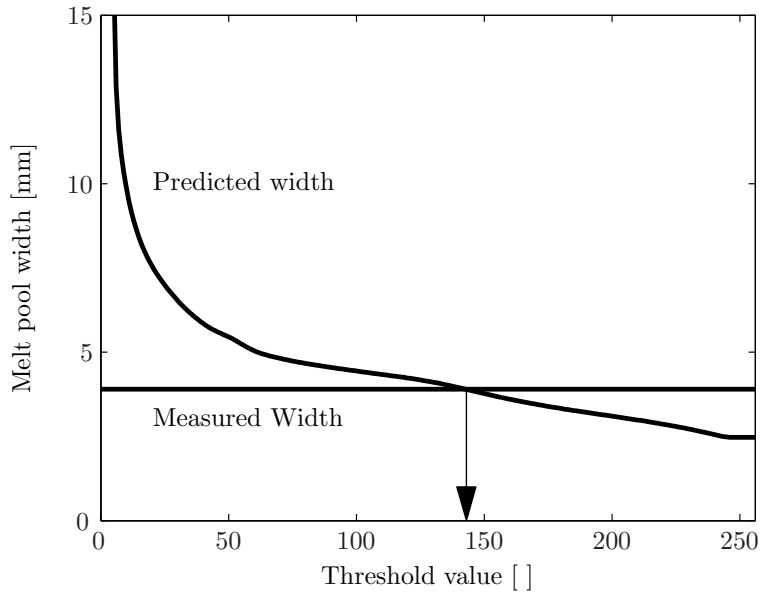


Figure 5.11: Predicted melt pool width at different threshold values based on 400 frames.

for all the investigated powders.

The radiation increases with increasing temperature according to equa-

Table 5.3: Threshold values for the investigated powders.

	Threshold Value []	Track Width [mm]
Stellite 12	142	3.85
Metco 42c	231	4.12
Ultimet	196	4.01
Metco 51NS	142	3.94
ALSi12	117	4.49
Delcrome 200	93	4.10

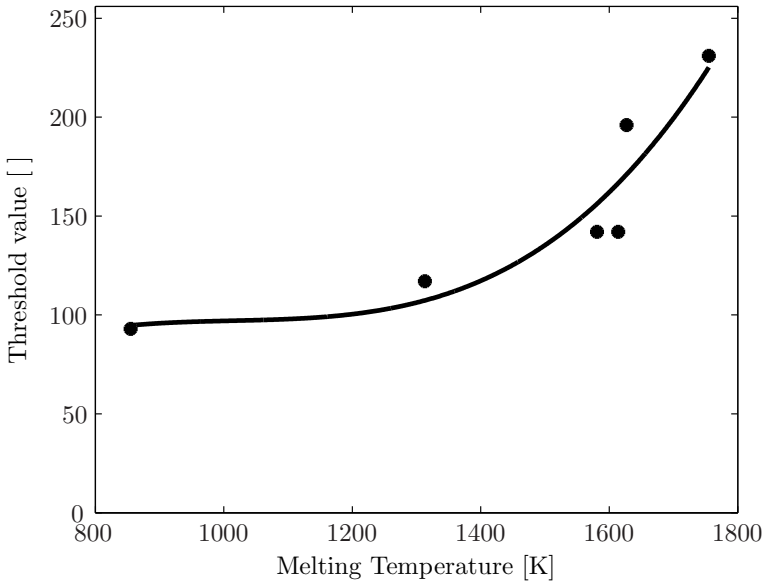


Figure 5.12: Threshold values determined for powders with different melting temperatures.

tion 5.4. As the threshold value is directly linked to the melt temperature of the clad material, a higher melting temperature gives a higher threshold value (assuming that the contributions of all other material parameters are small). Figure 5.12 shows the correlation between the melting temperatures and the corresponding threshold values.

5.6 Review and conclusions

By using a commercial CMOS camera and an optical low pass filter, thermal images of the melt pool area can be captured. A software program has been developed to calculate the dimensions of the melt pool. The procedure involves the determination of the threshold value that corresponds to the melting temperature of the clad material. This value can be determined by measuring the actual width of a track and depends on the material. The system, running at 30 - 300 Hz, is capable to obtain the dimensions of the melt pool in real time thus making it suitable for a real time control strategy.

Chapter 6

Modeling of the melt pool

6.1 Introduction

To study the different aspects of the laser cladding process, process models can be helpful. There are many different modeling methods, all with their specific advantages. In this chapter, a 3D Finite Element Method (FEM) model is described which was developed and used to study the temperature distribution around the melt pool zone and the shape of the clad layer. This model has been used to investigate the influence of process input parameters on the temperature and melt pool shape and to find correlations between melt pool characteristics. For a good bonding, a thin layer of the base material must be melted. To realize this, sufficient laser power is required [39]. However, too much laser power will increase the melt depth resulting in too much dilution. Due to heat accumulation, the dilution increases as well [40]. The developed FEM model of the laser cladding process uses a novel method for the determination of the clad geometry.

This chapter describes first the modeled clad domain. The heat balance and boundary equations which involve the heat fluxes as well as the interaction between the laser beam and powder jet are discussed. Next a mathematical geometrical transformation method is discussed.

6.2 Finite Element Model

The model has been developed using the COMSOL MP 3.2 software package. In the model three domains are distinguished, the substrate, the melt pool and the solidified domain. The process is modeled as a statio-

nary problem, by fixing the frame of reference to the laser beam, i.e. the material flows through the domains. The melt pool flow is not considered in the current model. The laser beam and the powder jet are described by a 2-dimensional source distribution which can be chosen arbitrarily independent of their position along their main axes. Also the orientations and locations of these axes can freely be chosen. Figure 6.1 shows the domains as well as the laser beam and powder jet.

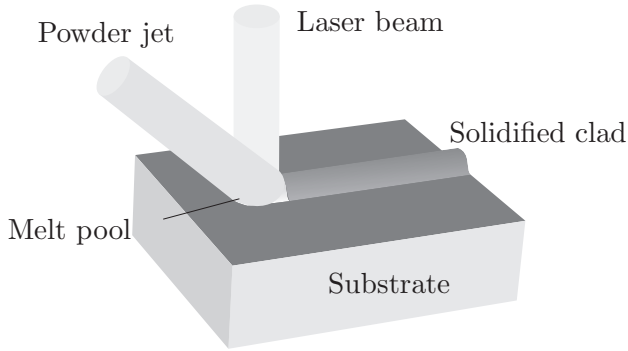


Figure 6.1: Domains, laser beam and powder jet.

6.2.1 Heat balance

For all the domains the basic equation can be written in terms of temperature T as:

$$\rho c_p \frac{\partial T}{\partial t} + \rho c_p \vec{\mathbf{v}} \cdot \nabla T = \nabla \cdot k \nabla T, \quad (6.1)$$

where k (thermal conductivity), c_p (heat capacity) and ρ (density) are material property coefficients, which can be functions of temperature T and/or space. The velocity vector $\vec{\mathbf{v}}$ is the velocity of the material in a coordinate frame which is fixed to the laser beam. This implies that even if the material is solid, the velocity is not zero, but equal to the cladding speed, as this is the relative velocity by which the laser beam "sees" the material moving by. To analyze the balance equation, it is useful to make the equation non-dimensional by introduction of a characteristic temperature level T_0 , length L_0 , and speed U_0 . In this work the following

typical quantities are adopted:

$$\begin{aligned} T_0 &= T_{melt} \quad (\text{melting temperature}) \\ L_0 &= \frac{1}{2}d_{spot} \quad (\text{laser spot radius}) \\ U_0 &= V_c \quad (\text{cladding speed}). \end{aligned} \quad (6.2)$$

By the choice of a characteristic length and speed automatically a characteristic time scale t_0 is defined:

$$t_0 = \frac{L_0}{U_0} \quad (\text{time scale}). \quad (6.3)$$

Substitution of these scaling variables into equation 6.1 and multiplying by $L_0/(U_0T_0)$ results then in the following equation, where \tilde{T} , $\vec{\tilde{\mathbf{v}}}$ and \tilde{t} refer to the non-dimensional variables, and ρ , c_p and k are assumed to be constant:

$$\frac{\partial \tilde{T}}{\partial \tilde{t}} + \vec{\tilde{\mathbf{v}}} \cdot \nabla \tilde{T} = \nabla \cdot Pe^{-1} \nabla \tilde{T}. \quad (6.4)$$

Here Pe is the non-dimensional *Péclet number*, which is the ratio of the convection term to the conduction term:

$$Pe = \frac{L_0 U_0 \rho c_p}{k}. \quad (6.5)$$

In general, the material properties such as density, conductivity and heat capacity are not constant, but depend on the temperature. The geometry of the clad domain is fixed, meaning that thermal expansion is not allowed. Therefore, also the density is modeled to be independent of the temperature.

The specific heat capacity $c_p(T)$ depends highly on the temperature. Therefore it has been split up into a non-dimensional time dependent part and a constant value $c_{p,0}$ (at the room temperature). The constant part can now be used for scaling the heat equation. This results in:

$$\begin{aligned} c_p(T) \frac{\partial \tilde{T}}{\partial \tilde{t}} + c_p(T) \vec{\tilde{\mathbf{v}}} \cdot \nabla \tilde{T} &= \nabla \cdot Pe^{-1}(T) \nabla \tilde{T} \\ Pe(T) &= \frac{L_0 U_0 \rho c_{p,0}}{k(T)}. \end{aligned} \quad (6.6)$$

Here, $c_p(T)$ now refers to the scaled (non-dimensional) heat capacity.

6.2.2 Boundary equations

To solve the heat balance in a domain, it is necessary to prescribe the boundary conditions along the complete boundary of the domain. The heat fluxes and temperatures at the boundaries are:

1. Initial temperature of the substrate,
2. Heat losses due to radiation,
3. Heat flux from the laser and
4. Heat flux associated with the hot particles arriving in the melt pool.

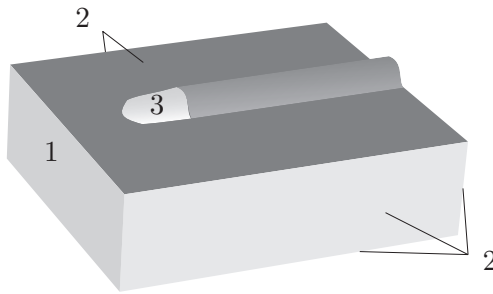


Figure 6.2: Boundaries of the clad model.

Radiation losses occur on all boundaries, especially in the melt pool area. The radiation losses Q of a surface can be expressed using equation 5.4 and 5.3 (on page 54) as:

$$Q = \varepsilon(T) \cdot A_s \cdot \sigma(T_m^4 - T_a^4),$$

where A_s , T_m and T_a are the surface area, the temperature of the surface and the ambient temperature respectively. The melt pool size will be in the order of 10 mm^2 and its average temperature is about 3000 K. Assuming maximum emissivity ($\varepsilon(T) = 1$) and an ambient temperature of 293 K, the heat losses become about 45 W. Compared to the laser power in the order of 1000 W, the radiation losses are neglectable.

The initial temperature of the substrate is used at the inflow boundary (area 1 of figure 6.2) of the substrate domain. On the other boundaries of the substrate as well as the outer surface of the solidified clad (area 2 of Figure 6.2), the heat flux is assumed to be zero. This assumption is valid as long as the dimensions of the substrate in the model are relatively large and the boundary temperature does not increase much. At the top surface

of the melt domain (area 3 of figure 6.2) the boundary condition is given by the interaction with the laser beam and the powder jet.

The heat input is split-up into two parts. Firstly, the laser radiation passes through the powder jet and arrives in the melt pool attenuated. Secondly, the supplied powder after passing through the laser beam arrives at the melt pool at an elevated temperature. As these boundaries are generally at elevated temperatures, an energy flux associated with material flowing through this surface has to be taken into account. This results in the following boundary condition:

$$k \frac{\partial T}{\partial n} + q_{mass} = q_{laser} + q_{powder}. \quad (6.7)$$

Here $q_{laser}(\vec{\mathbf{x}})$ is the heat flux associated with the laser radiation and $q_{powder}(\vec{\mathbf{x}})$ is the heat flux associated with the pre-heated powder. The convective heat flux $q_{mass}(\vec{\mathbf{x}})$ at the left side of the equation can be expressed as:

$$q_{mass}(\vec{\mathbf{x}}) = -\vec{\mathbf{v}} \cdot \vec{\mathbf{n}} \int_{T_0}^{T(\vec{\mathbf{x}})} \rho c_p dT, \quad (6.8)$$

where $\vec{\mathbf{v}}$ is the speed of the material, $\vec{\mathbf{n}}$ is the outward normal vector of the surface and $\int_{T_0}^{T(\vec{\mathbf{x}})} \rho c_p dT$ is the heat of the material at elevated temperature $T(\vec{\mathbf{x}})$. The laser power $q_{laser}(\vec{\mathbf{x}})$ absorbed at the surface can be expressed as:

$$\begin{aligned} q_{laser}(\vec{\mathbf{x}}) &= C \cdot \alpha(\vec{\mathbf{x}}) q_{0,laser}(\vec{\mathbf{x}}) \\ \alpha(\vec{\mathbf{x}}) &= \exp \int_S -\frac{A_p \Phi(\vec{\mathbf{x}}(s))}{V_p v} ds. \end{aligned} \quad (6.9)$$

Here, C is the absorption coefficient and $\alpha(\vec{\mathbf{x}})$ is the optical density of the powder jet at point $\vec{\mathbf{x}}$. The function $q_{0,laser}(\vec{\mathbf{x}})$ is the intensity of the original laser beam and $\Phi(\vec{\mathbf{x}}(s))$ is the powder jet intensity. Values A_p , V_p and v_p are the projection surface, volume and speed of the powder particles respectively. (See appendix C for the derivation of these formulas.)

The heat flux associated with the arriving powder particles can be expressed as:

$$q_{powder}(\vec{\mathbf{x}}) = C \frac{A_p \Phi(\vec{\mathbf{x}})}{V_p v} \int_M \alpha(\vec{\mathbf{x}}(m)) q_{laser}(\vec{\mathbf{x}}) dm. \quad (6.10)$$

The trajectory M is the path of the particles through the laser beam, parallel to the powder jet axis, running from the powder jet origin to the point $\vec{\mathbf{x}}$. The heat flux of the powder has a significant influence on the boundary condition, especially when the powder jet is dense as the laser beam can hardly penetrate the powder jet. The boundary equation is made non-dimensional by means of the previously defined characteristic values:

$$Pe^{-1} \frac{\partial T}{\partial n} = \frac{1}{\rho c_{p,0} T_0 U_0} (q_{laser} + q_{powder} - q_{mass}). \quad (6.11)$$

A more detailed description of the laser beam and powder interaction, as well as the mathematical derivation of the equations is given in appendix C.

6.2.3 Geometrical transformation

While the geometry of the substrate domain remains fixed, the geometry of the other two domains will depend on the temperature T and the powder jet distribution. The temperature on the other hand depends on the geometry. This interaction makes it hard to determine a-priori the clad shape. The shape of the melt pool domain can be determined by an initial guess for its shape, and iteratively determine the temperature field along this surface and adjust the geometry accordingly. This involves a high computational load, as every time the geometry has to be adjusted, the FEM model needs to be re-meshed and solved. An interesting approach to deal with the complication of this unknown boundary geometry in a numerical method is to mathematically transform the physical relations rather than the geometry. This mathematical approach can be described as follows; *The physical domain is transformed through a properly selected transformation which is directly linked with the unknown surface onto a computational domain which has a fixed shape. The balance equations describing the physical effects are also transformed and solved in the fixed computational domain. The solution is then transformed back to the original physical domain, providing the final solution.*

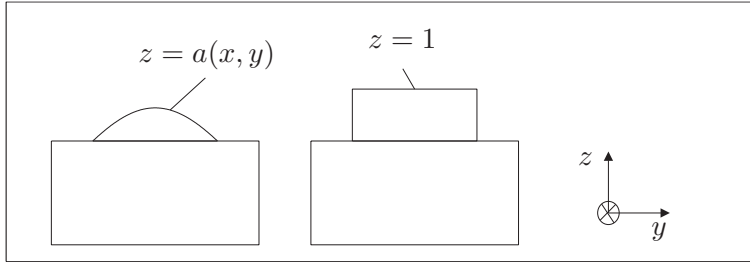


Figure 6.3: Physical (left) and computational (right) domains.

The clad surface is described by a function $z = a(x, y)$ (see Figure 6.3 left). The x and y axes are taken parallel and transverse to the cladding direction respectively. The z direction is normal to the original substrate top surface. In the computational domain, the height of the clad layer has a fixed thickness of unity (right graph in Figure 6.3). The height $a(x, y)$ of the layer in the physical domain is determined by integrating the local powder flux arriving at the surface. This powder flux is only absorbed if the local temperature at the contact surface is above the melting temperature. Using the Heaviside function H_{hs} this results in the following equation:

$$\vec{\mathbf{U}} \cdot \vec{\mathbf{n}} = (\vec{\mathbf{P}}_{\text{powder}} \cdot \vec{\mathbf{n}}) \Phi(\vec{\mathbf{x}}) H_{hs}(T - T_0), \quad (6.12)$$

where $\vec{\mathbf{U}}$ is the cladding speed and $\vec{\mathbf{P}}_{\text{powder}}$ is the main axis of the powder jet. The left side of this equation represents the mass flux leaving the clad surface and the right side represents the mass flux arriving at the clad surface. The vector $\vec{\mathbf{n}}$ is the unknown outward normal of the clad surface which is to be solved. This is illustrated in Figure 6.4. Because the

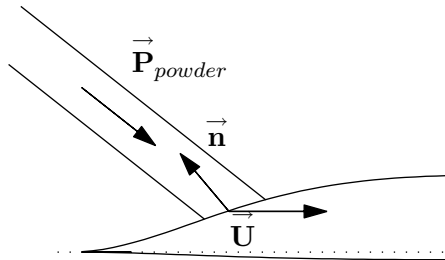


Figure 6.4: The mass balance on the clad surface.

melt pool flow is not taken into account, the effects of surface pressure and surface tension are neglected.

The transformation in the melt pool and solidified clad domains is described by:

$$\begin{aligned} x &= \xi \\ y &= \eta \\ z &= \alpha(\xi, \eta)\zeta. \end{aligned} \tag{6.13}$$

The Jacobian and inverse Jacobian matrices are:

$$\begin{aligned} J &= \begin{bmatrix} \frac{\partial x}{\partial \xi} & \frac{\partial x}{\partial \eta} & \frac{\partial x}{\partial \zeta} \\ \frac{\partial y}{\partial \xi} & \frac{\partial y}{\partial \eta} & \frac{\partial y}{\partial \zeta} \\ \frac{\partial z}{\partial \xi} & \frac{\partial z}{\partial \eta} & \frac{\partial z}{\partial \zeta} \end{bmatrix} = \begin{bmatrix} 1 & 0 & 0 \\ 0 & 1 & 0 \\ \zeta \frac{\partial \alpha}{\partial \xi} & \zeta \frac{\partial \alpha}{\partial \eta} & \alpha \end{bmatrix} \\ J^{-1} &= \begin{bmatrix} \frac{\partial \xi}{\partial x} & \frac{\partial \xi}{\partial y} & \frac{\partial \xi}{\partial z} \\ \frac{\partial \eta}{\partial x} & \frac{\partial \eta}{\partial y} & \frac{\partial \eta}{\partial z} \\ \frac{\partial \zeta}{\partial x} & \frac{\partial \zeta}{\partial y} & \frac{\partial \zeta}{\partial z} \end{bmatrix} = \begin{bmatrix} 1 & 0 & 0 \\ 0 & 1 & 0 \\ -\zeta \frac{\partial \alpha}{\partial \xi} & -\zeta \frac{\partial \alpha}{\partial \eta} & \frac{1}{\alpha} \end{bmatrix}. \end{aligned} \tag{6.14}$$

Using the inverse Jacobian matrix, the heat equation is expressed in the computational domain. The gradient operators in the physical and computational domain, i.e. ∇T and $\nabla_c T$ respectively, are related to each other as:

$$\begin{aligned} \nabla T &= \left[\frac{\partial T}{\partial x}, \frac{\partial T}{\partial y}, \frac{\partial T}{\partial z} \right]^T \\ \nabla_c T &= \left[\frac{\partial T}{\partial \xi}, \frac{\partial T}{\partial \eta}, \frac{\partial T}{\partial \zeta} \right]^T \\ \nabla T &= (J^{-1})^T \nabla_c T. \end{aligned} \tag{6.15}$$

By using this relation, the heat equation (Equation 6.6) is redefined as:

$$\begin{aligned} c_p(T) \frac{\partial T}{\partial t} + c_p(T) \vec{\mathbf{v}} \cdot (J^{-1})^T \cdot \nabla_c T &= \nabla_c \cdot \left(Pe^{-1}(T) J^{-1} \cdot (J^{-1})^T \nabla_c T \right) \\ Pe(T) &= \frac{L_0 U_0 \rho c_{p,0}}{k(T)}. \end{aligned} \tag{6.16}$$

The boundary equation (Equation 6.11), represented here, has to be transformed as well:

$$Pe^{-1} \frac{\partial T}{\partial n} = \frac{1}{\rho c_{p,0} T_0 U_0} (q_{laser} + q_{powder} - q_{mass}). \quad (6.17)$$

The derivative on the left side of the equation is then expressed as:

$$\frac{\partial T}{\partial n} = \vec{\mathbf{n}} \nabla T. \quad (6.18)$$

The normal vectors in the physical and computational domains, $\vec{\mathbf{n}}$ and $\vec{\mathbf{n}}_c$ are related by:

$$\begin{aligned} \vec{\mathbf{n}} &= [\vec{\mathbf{n}}_x, \vec{\mathbf{n}}_y, \vec{\mathbf{n}}_z]^T \\ \vec{\mathbf{n}}_c T &= [\vec{\mathbf{n}}_{c,x}, \vec{\mathbf{n}}_{c,y}, \vec{\mathbf{n}}_{c,z}]^T \\ \vec{\mathbf{n}} &= J \vec{\mathbf{n}}_c. \end{aligned} \quad (6.19)$$

The boundary equation in the computational domain can now be expressed as:

$$\begin{aligned} Pe^{-1} \vec{\mathbf{n}}_c \cdot J^T \cdot (J^{-1})^T \nabla_c T &= \frac{1}{\rho c_{p,0} T_0 U_0} (q_{laser} + q_{powder} - q_{mass}) \\ Pe^{-1} \vec{\mathbf{n}}_c \cdot \nabla_c T &= \frac{1}{\rho c_{p,0} T_0 U_0} (q_{laser} + q_{powder} - q_{mass}) \quad (6.20) \\ Pe^{-1} \frac{\partial T}{\partial n_c} &= \frac{1}{\rho c_{p,0} T_0 U_0} (q_{laser} + q_{powder} - q_{mass}). \end{aligned}$$

As a result of the applied transformation method, the temperature distribution within melt and clad domains depend on the (unknown) clad height $a(x, y)$ and vice versa. Now within the FEM code, these two unknowns are solved simultaneously, providing the temperature distribution and the clad height.

6.3 Review and conclusions

In this chapter, the developed FEM model of the laser cladding process is presented. The model incorporates the effect of the powder jet on the heat balance as well as its influence on the laser beam radiation. Using

a mathematical transformation, the temperature solution is solved in the computational domain. With this solution, the real temperatures are obtained using the corresponding transformations. This approach solves the clad geometry and temperature field simultaneously. Results of this approach and a comparison with experimental results are given in chapter 7.

Chapter 7

Clad characteristics and correlations using FEM model simulation and experiments

7.1 Introduction

In this chapter the influence of the main process settings on the clad characteristics as studied by simulations (based on the FEM model of chapter 6 and experimental verification is discussed.

The process conditions vary during the cladding process. Such variations are the substrate temperature, the geometry, the heat sink capacity and the material combination. During continuous cladding, the temperature of the substrate close to the cladding zone will increase from room temperature up to several hundreds of degrees Celsius. As a result, the dimensions of the melt pool and the dilution will increase. Changes in the geometry and consequently the heat sink capacity can be considerable. For instance, cladding toward the end of a shaft will lead to a significant heat build up. All these factors influence the clad quality, especially the dilution. To control this an adequate online control of one of the process settings by real-time control strategies is necessary.

The dilution plays an dominant role in the properties of the clad layer. For online control of the dilution, one or more real-time measurable features which correlates well with the dilution have to be identified. For this purpose, the influence of the main process parameters, i.e. laser power, cladding speed, powder feed rate and the spot diameter on the clad charac-

teristics is investigated. These investigations were performed using FEM simulations. Clad experiments were performed to compare and validate the simulation results.

This chapter starts by describing the simulation and experimental procedures in section 7.2. Section 7.3 presents the correlations between the process settings and the clad track characteristics. From such correlations, the width of the melt pool is selected as control parameter. This choice is discussed in section 7.5. The next section, 7.6 discusses the cooling rates in the clad layers and the influence of the process settings on these cooling rates. This chapter finalizes by presenting the major conclusions in section 7.7.

7.2 Simulation and experimental procedures

In chapter 4, the influence of the process settings like laser beam energy distribution, cladding speed and laser power on the melt pool and clad track characteristics were discussed. Using the FEM model as described in chapter 6 and using clad track experiments these effects are investigated in more detail. The experimental results are used to compare and validate the FEM model simulation results. From the results, correlations between the dilution and measurable clad characteristics are investigated and discussed.

7.2.1 Simulations procedure

The material properties applied in the simulations (based on 0.2 %C steel and Stellite 12) are shown in Table 7.1. The absorption coefficient is set

Table 7.1: Values for the most important parameters used during the experiment.

Property	Value
Latent heat of fusion	$270 \cdot 10^3$ [J/kg]
Specific heat Solid	460 [J/(kg.K)]
Specific heat Liquid	750 [J/(kg.K)]
Melting temperature	1350 [$^{\circ}$ C]
Density	8000[kg/m^3]
Absorption coefficient	0.5

to 50 % for both the substrate and the powder jet, yielding an overall efficiency of 50 % in correspondence with data from Gedda [7] (Table 2.3).

The latent heat of fusion has a significant influence on the heat balance. For comparison, for a low alloyed steel, the latent heat of fusion is about 270×10^3 J/kg. The energy required to heat up the same material from room temperature to melting temperature, is about 612×10^3 J/kg. The latent heat of fusion is included in the specific heat by distributing it over a certain temperature range which corresponds with the fact that alloys have no sharp defined melting point. Although in reality this range can be relatively small, due to numerical stability this temperature range is chosen to be 100 K below and above the melting temperature. Figure 7.1 shows the specific heat and the thermal conductivity as function of the temperature [41].

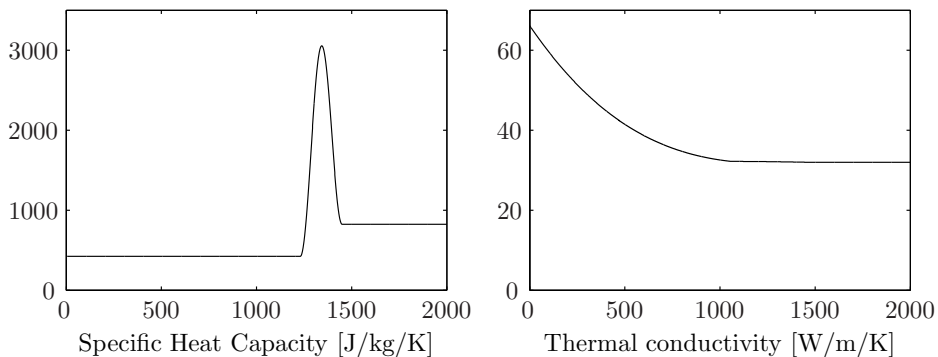


Figure 7.1: The specific heat capacity including the latent heat and the thermal conductivity as function of temperature ([41]).

The lateral powder jet is modeled from the front at an angle of 50° to the substrate surface. The laser beam is positioned perpendicular to the substrate surface. The main axes of the powder jet and the laser beam coincide at the substrate surface. The laser power is modeled to be a close to real Top-hat distribution which drops smoothly to zero at the edge. The powder distribution is taken to be axial symmetric with a high intensity at the center and decreasing to zero by a square root function. The diameter of the powder jet is taken equal to the laser beam diameter.

The geometry of the clad track and the temperature distribution are solved simultaneously by a Generalized Minimal Residual (GMRES) iterative solver. The temperature and geometry solutions are obtained in the computational domain. This domain uses a fixed constant shape for the clad track as explained in section 6.2.3 starting on page 72. The solution is transformed using the geometric and temperature scaling constants and

the calculated geometry of the clad track. This is graphically show in figure 7.2.

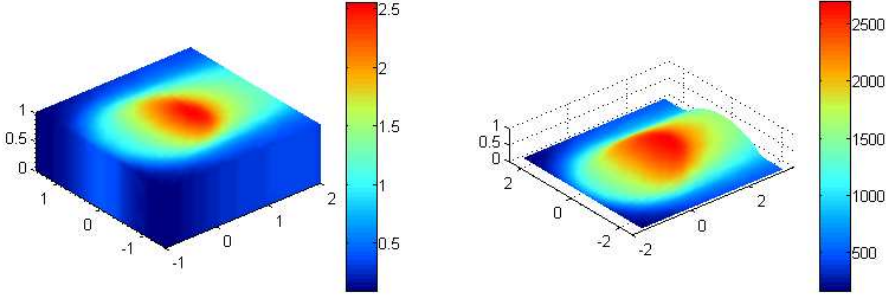


Figure 7.2: Temperature solution of the melt pool domain. On the left side the solution obtained by the model is presented. The right side shows the solution in the physical domain after transformation. The laser spot diameter is 3 mm, the laser power 1600 W and the cladding speed 10 mm/s.

7.2.2 Experimental procedure

Clad tracks of Stellite 12 were produced on a mild steel substrate using the setup described in chapter 3 (Figure 3.3 on page 24). A robot with six degrees of freedom is used for the movement of the laser cladding head over a stationary substrate bar of $200 \times 12 \times 12$ mm. The powder is fed by nitrogen as carrier gas from the front with the nozzle as described in chapter 3 at an angle of 50° to the substrate. The melt pool area is shielded by nitrogen gas.

During each experiment, the laser power is increased linearly between two levels, while the cladding speed and the powder feed rate were kept constant. The dimensions of the clad tracks were obtained from cross-sections. The width and length of the melt pool are obtained from the monitoring system as described in chapter 5.

The laser power P_l , cladding speed V_c , specific powder feed rate $F_{s,powder}$ and the laser beam diameter d_{spot} have been varied in accordance with Table 7.2. The specific powder feed rate is the powder feed per unit length:

$$F_{s,powder} = \frac{F_{powder}}{V_c}. \quad (7.1)$$

A constant specific feed rate implies that the cross-section areas are cladding speed independent.

Table 7.2 gives an overview of the process settings. In the experiments, the laser power is increased linearly from a low to a high value over the full length of the tracks. Cross-sections were cut at distinct locations along the track where the lasers power coincides with the simulations. Both simulations and experiments were performed using two different spot sizes and four cladding speeds.

Table 7.2: Input parameters

Spot diameter [mm]	Simulations		Experiments	
	3.0	4.5	3.0	4.5
Laser power [W]	600,850,1100 1350,1600,1850	600,1000,1400 1800,2200,2600 3000,3400,3800	500 - 2000	500 - 4000
Cladding speed [mm/s]	5, 7, 10, 15	5, 10, 15, 20	5, 7, 10, 15	5, 10, 15, 20,
Specific powder feed rate [mg/mm]	20.4	34.0	20.4	34.0
Initial substrate Temperature [C ⁰]	20,50,100, 150,200,250	20	room temperature	room temperature

7.3 Results and discussion

Figure 7.3 shows cross-sections of some simulated clad tracks as well as optical photographs of corresponding experiments. The upper left image shows that the simulated track width (white lines) is smaller than the experimental track width. The width of the track from the simulations is determined by the width of the melt pool where powder is only added to the substrate if its temperature is above the melting point. Although the width of the track from the experiment is larger, there is no good metallurgical bound at the sides of the track. This indicates that molten powder flows over a solid substrate. So the real width of the melt pool of the substrate is smaller than that observed by the camera. The dimensions of the track increase with increasing specific heat input. The dimensions from simulations and experiments match very well, although the molten substrate material (hence dilution) is slightly larger in the simulations.

Photographs of all the cross-sections can be found in the appendices D and E.

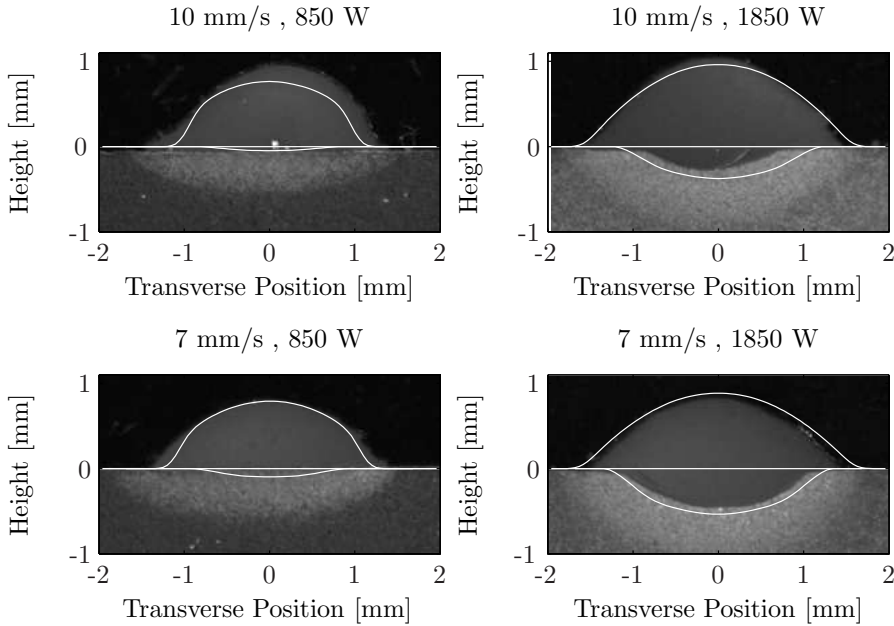


Figure 7.3: Cross-section of some clad tracks. The cladding experiments were performed at speeds of 7 and 10 mm/s and laser powers of 850 and 1850 W respectively, using a spot diameter of 3.0 mm and a specific powder feed rate of 20.4 mg/mm. The white lines are the corresponding modeling results.

Melt pool width and length

Both the length and width of the melt pool are candidate as sensors for a feedback based control strategy. In the Figures 7.4(a) and 7.4(b) the melt pool width and length both from simulations and experiments are compared. Each dot corresponds to one simulation (x-axis) and the corresponding experiment (y-axis). There is a good match between simulation and experiments. The width varies from about 2 mm for low specific energy up to 5 mm for high specific energy. At high specific energy (upper right), the simulated width is slightly larger than the experimental width. At low specific energy (lower left), the width and length of the melt pool are somewhat larger in experiments than in the simulations. At high specific energy, the length of the melt pool shows larger deviations. This might be caused by the way in which the melt pool lengths are obtained from the camera images. The length of the melt pool is given by the larger radius of

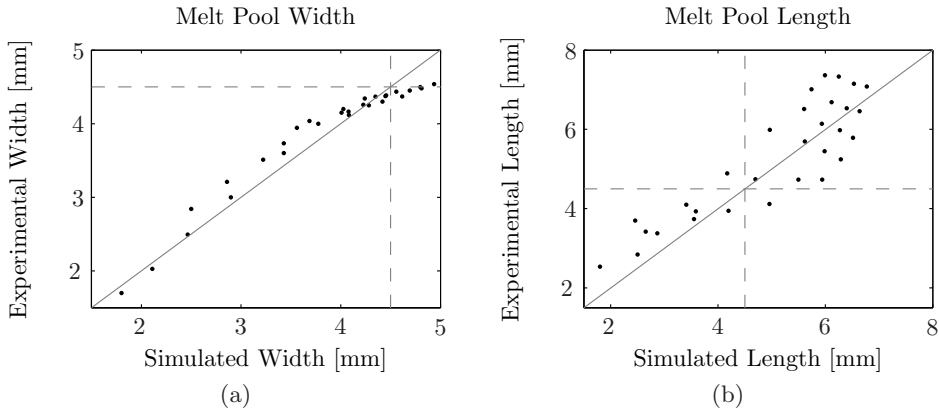


Figure 7.4: Correlation between the simulated and experimental melt pool width (left) and length (right). In all these simulations and experiments, the spot diameter equals 4.5 mm (dashed lines).

the fitted ellipse. Since in reality the melt pool shape will not be perfectly elliptical, some deviations in the length of the melt pool can be expected.

Track height

In Figure 7.5(a) the track height as determined from simulations and experiments are compared, showing a good agreement. At low energy input, the actual height is somewhat larger than the simulated heights. As seen in Figure 7.4(b), the real melt pool lengths are slightly larger in these situations as well. A longer melt pool results in an increased powder efficiency, as more powder is trapped into the melt pool which results in a higher track, explaining the difference between simulated and experimental track heights.

Dilution

Since the dilution is important for the quality of the clad layer, more detailed analyzes of the influence of the process settings is presented. The micro hardness of the clad layers is linked to dilution as well. The model predictions are in good agreement with experimental data as presented in Figure 7.5(b). The dilution levels vary between 10 % for low specific energy to 80 % for high specific energy.

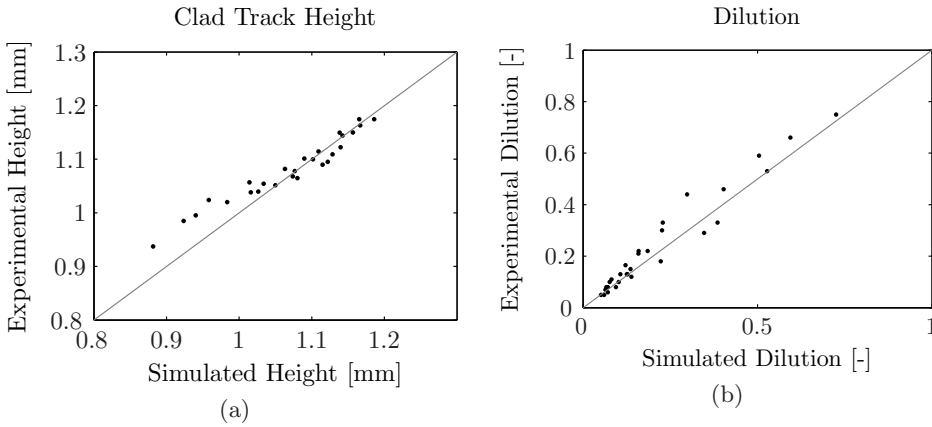


Figure 7.5: Correlation between the simulated and experimental track height (left) and dilution (right). In all these simulations and experiments, the spot diameter equals 4.5 mm (dashed lines).

7.3.1 Influence of the process settings on the clad characteristics

Melt pool and track characteristics

The width of the track in simulations equals the melt pool width, as they are related according to equation 6.12. The width of the melt pool is shown in Figure 7.6 for two cladding speeds, i.e. 10 mm/s (black lines) and 15 mm/s (gray lines) and two spot sizes, i.e. 3.0 mm (\diamond) and 4.5 mm (*). Also included are two dashed lines indicating the spot diameters.

The width increases with increasing laser power. At low power the width increases fast as a function of the power. At high power, the width becomes closer to the diameter of the laser spot and increases only marginally. By only increasing the laser power the specific heat increases. As discussed in chapter 4 this results in larger melt pool dimensions. The width of the tracks depends on the spot diameter. In the simulations with a 3.0 mm diameter spot, the maximum achievable melt pool width is limited to about this 3.0 mm as well. The same has been found with other diameters. This means that the spot diameter is the limit for the achievable melt pool width as was already explained in chapter 4 by means of the limited heat conductivity.

The length of the melt pool increases with laser power as well. At low laser power, the length is closer to the width of the melt pool, i.e. a

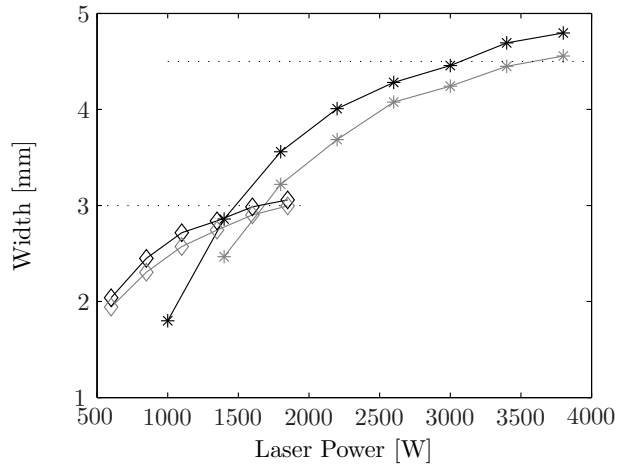


Figure 7.6: The melt pool width as function of the laser power for simulations performed at a cladding speed of 10 mm/s (black lines) and 15 mm/s (gray lines), using a 3.0 mm (\diamond) and 4.5 mm ($*$) laser spot.

somewhat circular melt pool is formed. At higher laser power, the melt pool becomes longer (about $1.5 \times$ the width).

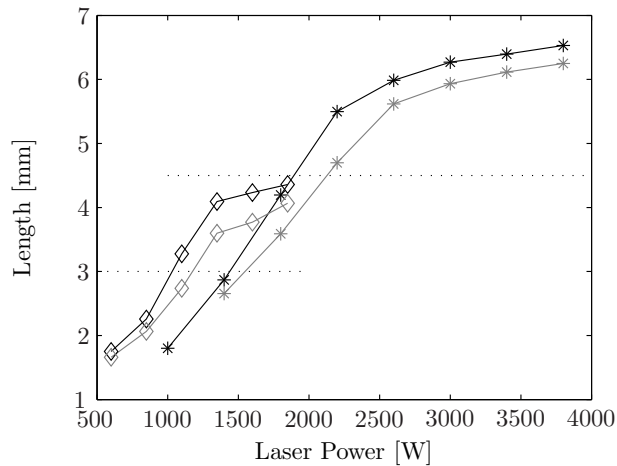


Figure 7.7: The melt pool length as function of the laser power. The presented data are from simulations performed at a cladding speed of 10 mm/s (black lines) and 15 mm/s (gray lines), using a 3.0 mm (\diamond) and 4.5 mm ($*$).

The cladding speed is less important than the laser power. The width of the melt pool reduces with increasing cladding speed because of the reduced specific heat input as explained in chapter 4. The length of the melt pool reduces with increasing cladding speeds.

The track height as function of the laser power is presented in Figure 7.8 for two cladding speeds (10 mm/s, black lines and 15 mm/s, gray lines) and two spot sizes (3.0 mm, \diamond and 4.5 mm *). The heights obtained using a 4.5 mm spot are larger than the heights obtained using a 3.0 mm spot diameter. This is caused by the different specific powder feeds used in the simulations. As the width is limited to the spot diameters, the height of the simulated tracks are somewhat larger in case of the 4.5 mm spot. Increasing

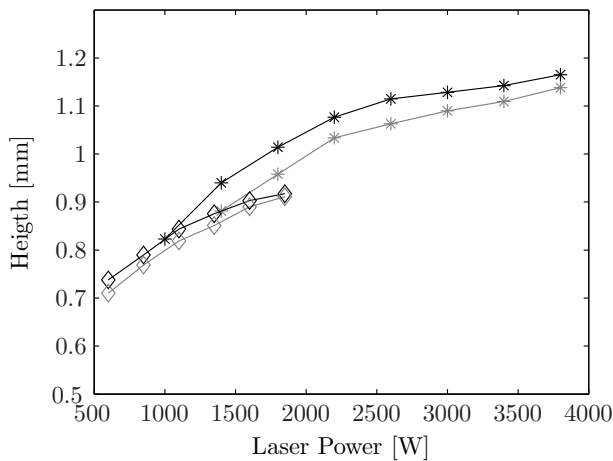


Figure 7.8: The clad track height as function of the laser power. The presented data are from simulations performed at cladding speeds of 10 mm/s (black lines) and 15 mm/s (gray lines), using a 3.0 mm (\diamond) and 4.5 mm (*).

the laser power results in a higher powder efficiency because an increasing melt pool length allows more powder to be trapped into the melt pool. The cladding speed has a negative influence on the height of the tracks.

Melt pool temperature

The melt pool temperature is relatively easy to measure and could be a control parameter. By using for instance a pyrometer, the temperature in the melt pool can be measured real-time. Various process controllers have been designed to adjust the laser power on this basis [33, 42]. From

the FEM simulations, the temperature of the center of the melt pool is obtained by averaging the simulated temperature over a circular area of 0.5 mm in diameter coaxial with the laser beam which corresponds to a typical field of view of a pyrometer. Figure 7.9 shows the results for a spot diameter of 4.5 mm. The temperature increases from close to the melt temperature at low laser power to about 3000 °C and 2500 °C for the low and high cladding speeds respectively. G. Bi [32] et al. performed cladding experiments using a photodiode as temperature sensor. The temperatures reported in their work are somewhat lower than the simulated temperatures in Figure 7.9. This is because the simulated temperatures are obtained in the center of the melt pool and the photodiode measures an average temperature over a larger area, resulting in lower temperatures. However, despite these differences, they found similar trends between the temperature and laser power as well as cladding speed.

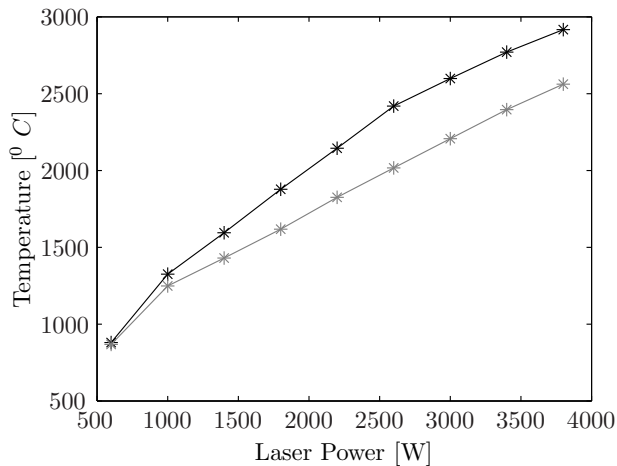


Figure 7.9: The melt pool temperature as function of the laser power as obtained from simulations for a cladding speed of 10 mm/s (black lines) and 15 mm/s (gray lines).

Dilution

The dilution depends on the amount of molten substrate material and molten powder which is fed into the melt pool as defined by equation 2.2 in chapter 2. With increasing laser power, both fractions will increase. With higher specific energy, the temperature gradients and therefore the heat

conduction will increase and the melt pool will grow in depth. At high powder efficiency further increasing the laser power will only lead to an increasing amount of molten substrate material, resulting in a fast increasing dilution level. Figure 7.10 shows the dilution obtained with a 3.0 mm

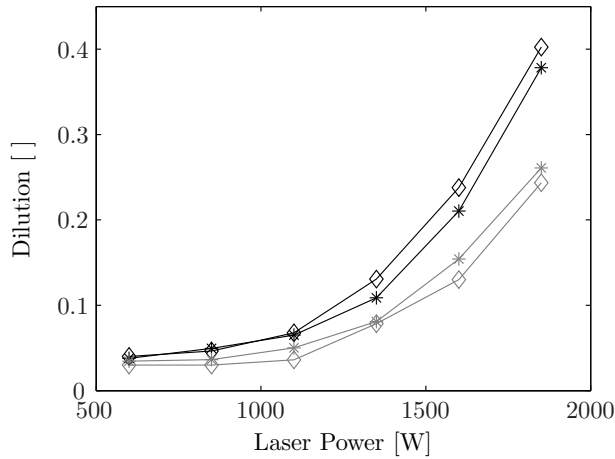


Figure 7.10: The dilution as function of the laser power. The presented data are from simulations (\diamond) and experiments ($*$) at a cladding speed of 10 mm/s (black lines) and 15 mm/s (gray lines). The spot diameter is 3.0 mm.

diameter spot. Both experimental and simulation data are plotted in this graph. Figure 7.11 shows the dilution level as function of the laser power using a 4.5 mm diameter spot. The dilution as obtained from the simulations increases exponentially with the laser power. At low energy input, a dilution level of about 5 to 10 % is obtained. At higher cladding speed, the FEM model predictions of the dilution level are below the experimentally obtained values whereas for lower cladding speed, the predictions are above the experiment results. This might be because the model does not take into account melt flow meaning the flow is fully determined by heat convection. With increasing speed, the relative effect of conduction decreases as explained in chapter 4. In reality however, a convective heat flux associated with the melt flow is present. This flow is enhanced by the momentum of the powder jet and results in a higher heat transport into the substrate. This results in a larger and deeper melt pool and more dilution. At low cladding speeds, the effect of the convective heat flux is less, and the experiments show less dilution. The observed differences between simulations and ex-

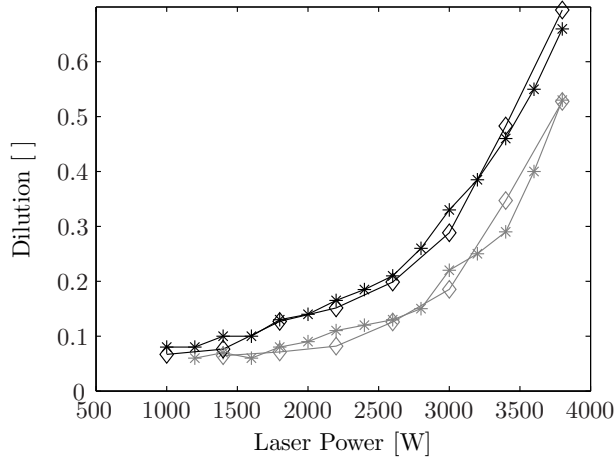


Figure 7.11: The dilution as function of the laser power. The presented data are from simulations (\diamond) and experiments ($*$) at a cladding speed of 10 mm/s (black lines) and 15 mm/s (gray lines). The spot diameter is 4.5 mm.

periments are less with a spot size of 4.5 mm (Figure 7.11) as compared to a 3.0 mm spot (Figure 7.10).

Conclusions

In the above sections, the influence of the main process parameters on clad and melt pool characteristics have been investigated. The observed relations can be well understood from a physical point of view. The general trends show that the dimensions of both the clad track and the melt pool increase with increasing laser power. The cladding speed has an opposite effect. The width of the melt pool and the clad track is highly determined by the laser spot size. At high specific energies, the width increases close to the diameter of the laser beam. The dilution increases with laser power, and the rate of increase becomes larger for higher laser powers. The results as predicted by the FEM simulations are in good agreement with the experimental results.

7.4 Influence of the dilution on the hardness

More dilution of substrate material into the clad material will generally reduce the advantages of the new surface. Especially the micro hardness of

the layers depends on the dilution. This section describes the influence of the process setting on the hardness of the clad layers and the heat affected zone.

Micro hardness measurements have been performed on selected samples using an automated indenter system (Buehler micromet[®] Hardness Tester) with a load of 200 gram force. The process settings of these samples are presented in Table 7.3. The hardness is measured at the center of the tracks from the base material through the heat affected zone and clad layer. As could be expected from the settings in Table 7.3 the dilution will vary considerable. The Figures 7.12(a) and 7.12(b) show the micro indentations as well as the hardness for two of the analyzed samples. The first sample shows a hardness of 460 HV0.2 in the clad layer. The second sample, produced with a lower laser power has almost no dilution. The hardness obtained in that clad layer is 610 HV0.2 which is considerably higher than that of the first one. Over the full height of the clad layers, an almost constant hardness has been obtained in both cases. The hardness

Table 7.3: Process settings of the samples used for hardness measurements.

	Laser Power [W]	Cladding Speed [mm/s]	laser spot diameter [mm]
1	1350	5	3
2	1350	7	3
3	1350	10	3
4	1350	15	3
5	1850	5	3
6	1850	7	3
7	1850	10	3
8	1850	15	3

profiles for all the samples of Table 7.3 are presented in the Figures 7.13 and 7.14. The hardness in the substrate is about 200 HV0.2. In the clad layer however, the hardness increases with increasing cladding speed which can be fully explained by the reduced dilution. The influence of dilution on the hardness of the clad layer is demonstrated by the average hardness as shown in Figure 7.15. The hardness decreases from 660 HV0.2 (1350 W, 15 mm/s) to 450 HV0.2 (1350 W, 5 mm/s) while the dilution increases by 50 % (from 10 % to 15 %). The same is observed for the samples produced at 1850 W. A dilution increase of 50 % leads to a hardness reduction of 200

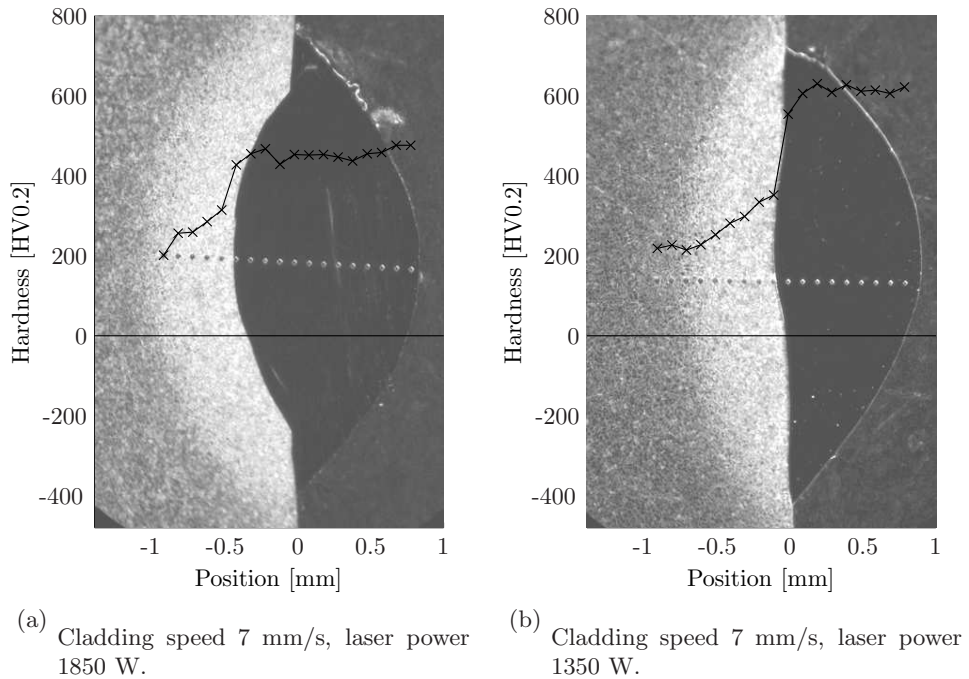


Figure 7.12: Two samples showing the indentations and the corresponding micro hardness.

HV0.2. Since an increase in dilution is caused by a decrease in cladding speed, the conclusion that the hardness drop is caused by the increase in dilution alone is premature. The average hardness of the samples produced at 1850 and 1350 W equal 509 and 593 HV0.2 respectively. The average dilution levels in these cases are 12 % and 37 %. This means an hardness increase of 16 % when the dilution increases by a factor of 3.

7.5 Sensor for real-time dilution control

As seen in the previous section, several melt pool characteristics increase with the laser power in a progressive manner. This indicates that they could be used to adjust the laser power using feedback control strategies. To control the dilution, it is important to identify a feature which yields a good and well defined relation with the dilution.

The width, length and temperature of the melt pool are relatively easy

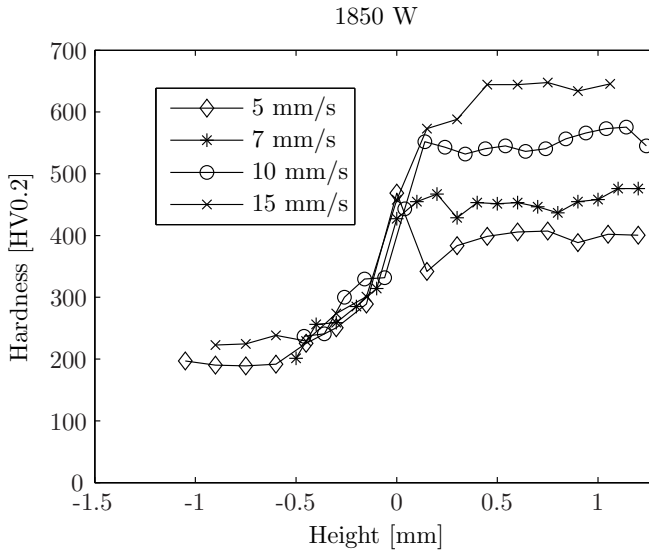


Figure 7.13: Micro hardness as function of the clad height and cladding speed. These tracks were produced using a laser power of 1850 W. The height of zero is the original surface.

to measure characteristics. A method based on camera images of the melt pool and a software algorithm to determine the geometrical features has been developed and presented in chapter 5. A pyrometer can be used to determine the temperature of the melt pool. As seen in the previous section, the determination of the melt pool width and length are good candidates as well. Figure 7.16 shows the dilution levels for all the simulations and experiments as function of the melt pool width. Figure 7.17 shows these values as function of the melt pool length. Figure 7.18 shows the same data as function of the temperature.

All the three melt pool characteristics show a progressive relation with the dilution. The dilution is relatively low as long as the width of the melt pool is small. Figure 7.16 shows that, by increasing the melt pool width to above about 2.8 mm and 4.1 mm for the 3.0 mm and 4.5 mm diameter laser spots respectively, the dilution increases rapidly. These values are determined by determining the crossing point of the asymptotes as indicated in Figure 7.16. Such a critical value for the melt pool width can be used for online control. Similar critical values can also be found for the melt pool length and temperature in case a 3.0 mm diameter laser spot is used.

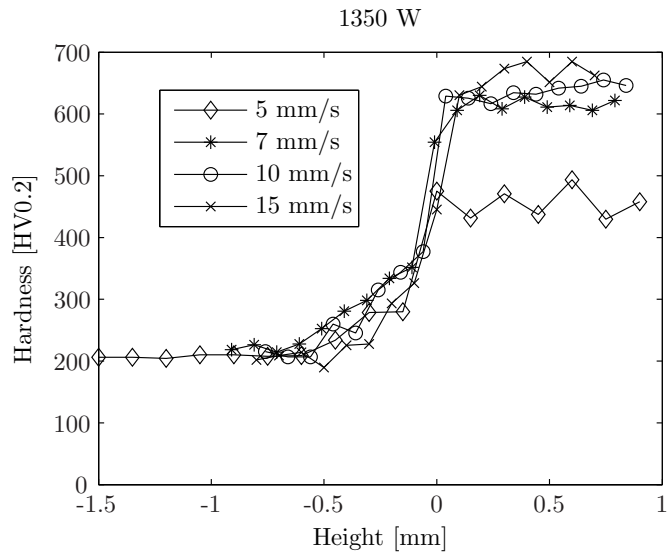


Figure 7.14: Micro hardness as function of the clad height and cladding speed. These tracks were produced using a laser power of 1350 W. The height of zero is the original surface.

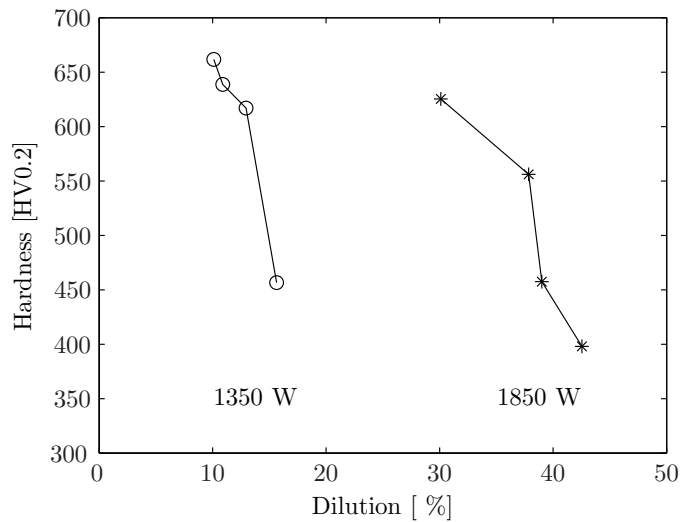


Figure 7.15: Micro hardness in the clad layer as function of the dilution. A dilution increase of 50 % leads to a hardness reduction of about 200 HV0.2.

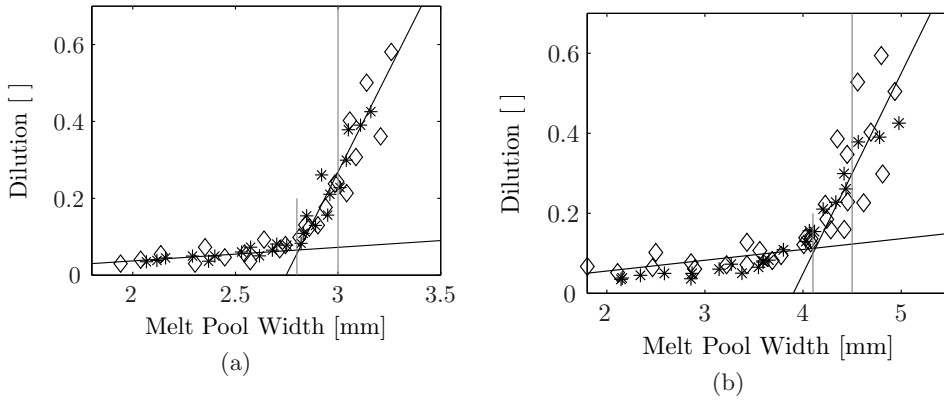


Figure 7.16: Correlation between the melt pool width and the dilution. The presented data are from simulations (\diamond) and experiments ($*$) using a 3.0 mm (left) and 4.5 mm (right) diameter spot.

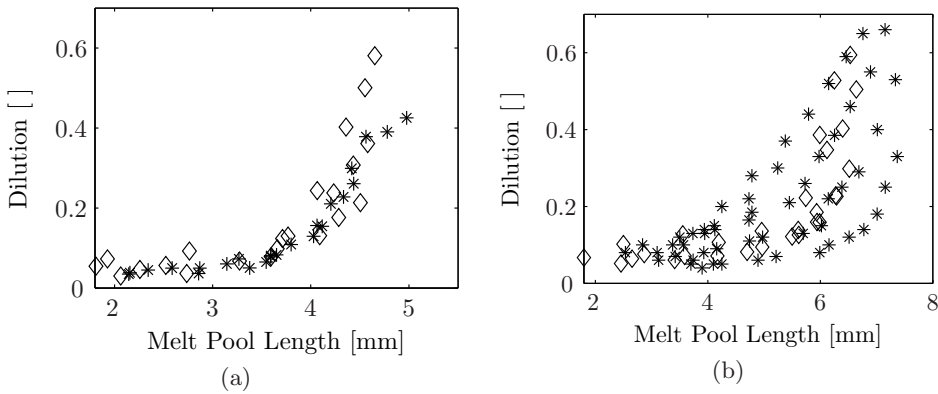


Figure 7.17: Correlation between the melt pool length and the dilution. The presented data are from simulations (\diamond) and experiments ($*$) using a 3.0 mm (left) and 4.5 mm (right) diameter spot.

However when a larger spot (4.5 mm) is used, such a relation can not be found because the influence of the cladding speed on the relations becomes more prominent. For instance, the dilution is limited as long as the melt pool length is below 4.0 mm in case the 3 mm laser spot is used, while using the larger laser spot the dilution varies considerably at a melt pool length of 4.0 mm.

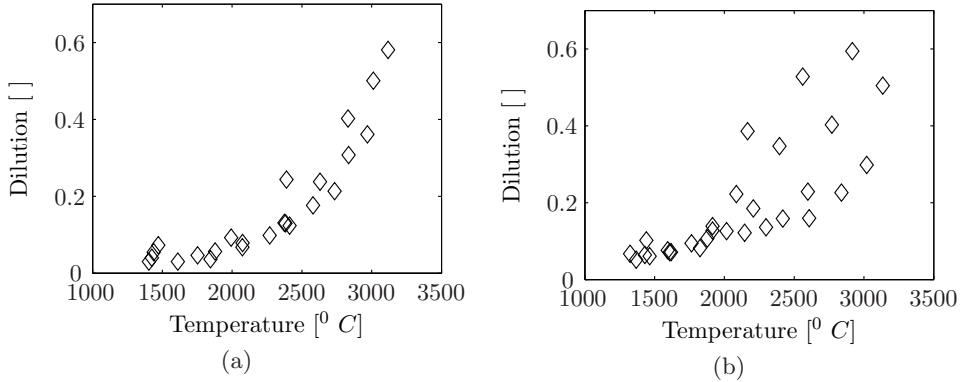


Figure 7.18: Correlation between the melt pool temperature and the dilution. The presented data are from simulations using a 3.0 mm (left) and 4.5 mm (right) diameter spot.

As long as the melt pool width is smaller than a critical value $W_{critical}$ which is about 90 % of the spot diameter, the dilution remains limited, whereas above these values, the dilution increases rapidly. This critical value is independent of the speed. The width of the clad tracks has a high degree of correlation with the melt pool width as shown in Figure 7.19. This makes the online measured melt pool width highly suited for control purposes. One aspect, which has not been addressed so far, is the temperature of the substrate material. Generally, due to the limited dimensions of the substrate, the temperature increases over time. To investigate whether the correlation between melt pool width and dilution, in particularly the critical point remains unaffected by temperature of the substrate, additional simulations were performed. The initial temperature was varied between room temperature and 250⁰ C. The spot diameter used in these simulations was 3.0 mm. The values for the other process settings are presented in Table 7.4. The correlation between the dilution and the melt pool width for these simulations is presented in figure 7.20. Increasing the substrate temperature leads to more dilution. However, the substrate temperature does not effect the aforementioned relation. Below a melt pool width of 2.8 mm, the dilution remains small, and increases fast at larger widths independent of the substrate temperature. This relation is in correspondence with the experimental results obtained from the overlap cladding experiments.

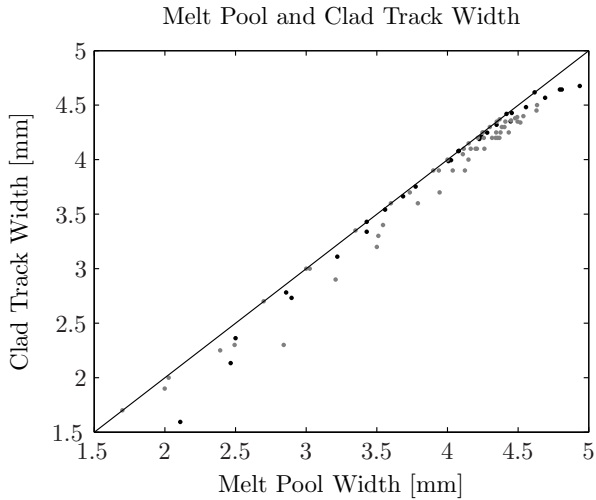


Figure 7.19: Correlation between the melt pool width and clad track width. In all these simulations and experiments, the spot diameter equals 4.5 mm. Both experimental (gray) and simulation (black) data are shown.

Table 7.4: Input parameters for the simulations performed to investigate the influence of the substrate temperature on the correlation between the melt pool width and the dilution.

Powder jet diameter [mm]	3.2
Laser power [W]	600, 850, ..., 1850
Cladding speed [mm/s]	7, 15
Specific powder feed [mm ³ /mm]	2.4
Spot size [mm]	3.0 \varnothing
Substrate temperature [C ⁰]	20, 50, 100, 150, 200, 250

Conclusions

The melt pool width has been found to be a relevant indicator for the dilution. As long as the melt pool width is smaller than 90 % of the laser beam diameter, the dilution levels are small. Increasing melt pool width to values above this critical value leads to a rapid increase of the dilution. This critical value is independent of the cladding speed and the temperature of the substrate. The width of the clad tracks is determined by the melt pool width as well. This makes the melt pool width ideal to be used as a sensor for online control using feedback strategies.

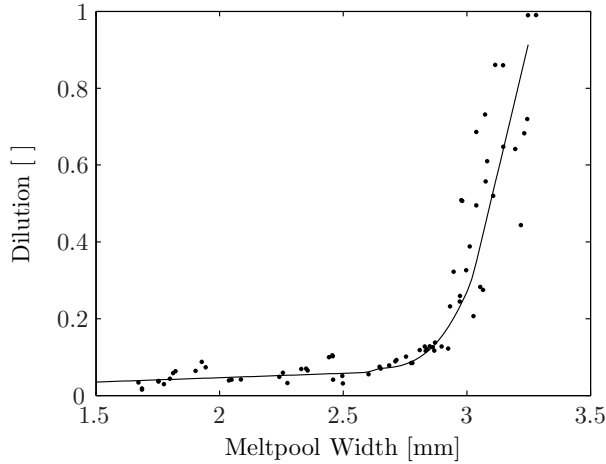


Figure 7.20: The dilution as function of the melt pool width for various cladding speeds, laser powers and initial substrate temperatures.

7.6 Temperature fields and cooling rates

Residual stresses and cracking phenomena are of great importance for the final clad integrity. Residual stresses are caused by location dependent differences in cooling rates which depend on the process settings, in particular the cladding speed. Figure 7.21(a) shows the temperature field along the main axis of simulated clad tracks for two different cladding speeds and two different laser powers. The process settings are equal to the ones presented in Figure 7.3 and discussed in the previous sections. Figure 7.21(b) shows the temperature history at four different clad heights in the center of the track. Also indicated is the period the material passes through the laser beam ($t = 0.32$ to 0.64 s). The melt temperature (1350 °C) is indicated as well. The cooling curves show an exponential like decay. Just above the melt temperature, the cooling rate decreases while below the melting temperature the cooling rate increases. This is caused by the latent heat of fusion, which acts like a heat capacitor in this temperature range. After about 2 s a uniform temperature is realized. The temperature curves from $T = 900$ °C to about $T = 150$ °C can be approximated by an exponential function (7.2).

$$T(t) = a \cdot e^{(-b \cdot t)} + c. \quad (7.2)$$

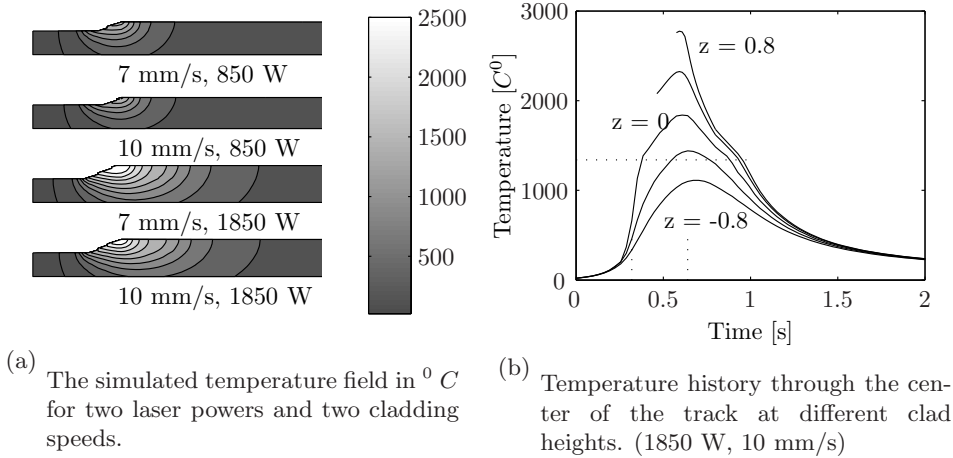


Figure 7.21: Simulated temperature for some process setting combinations using a 3.0 \varnothing spot.

Here, b [$1/s$] is a constant representing the cooling rate. Using this formula, the cooling rate is determined for all the simulated experiments at three different heights ($z = -0.4, 0.0, 0.4$ mm). Figure 7.22 shows the cooling rates b for all the performed simulations.

The cooling rates close to the surface in the clad tracks are slightly higher than these deeper into the substrate. The model does not take into account radiation heat losses at the surface as they are neglectable. With increasing cladding speed, the relative contribution of the conduction term to the temperature distribution diminishes. As a consequence, the cooling rates increase rapidly with the cladding speed from about 2 to 5 s^{-1} . By increasing laser power, a larger area is heated creating a more uniform temperature field as shown in Figure 7.21(a). Although the temperatures in the clad area increase, the temperature gradients in the depth just behind the melt pool become smaller. Therefore, heat conduction which is driven by temperature gradients, reduces resulting in smaller cooling rates. By using a larger spot size, the cooling rates reduce as well.

7.7 Review and conclusions

In this chapter, the results of the simulations and experiments have been presented and discussed. From the analysis of the cross-sections, the in-

fluences of the process parameters on the clad characteristics were determined and compared with simulations.

The width of the clad track is highly determined by the laser power, increasing rapidly at low laser powers and saturating at a value close to the laser beam diameter at high laser powers. The width of the melt pool is found to be dominantly controlled by the laser power. The dilution level is found to have a clear correlation with the melt pool width. This relation is found to be almost independent of the cladding speed and the specific powder feed rate. Based on these results, a control strategy to control the dilution can be developed. Adjusting the laser power real-time to realize a melt pool width of 2.8 and 4.1 mm (crossing of the asymptotes) for the two spot sizes respectively, will lead to limited dilution and large track widths and heights. Such a controller is developed and tested in chapter 8.

The temperature gradients are found to decrease with laser power, and increase with cladding speed. Since residual stresses are highly determined by the cooling rates, the stresses in clad tracks are expected to increase with cladding speed as well. The influence of the cladding speed on residual stresses was further investigated and described in chapter 11.

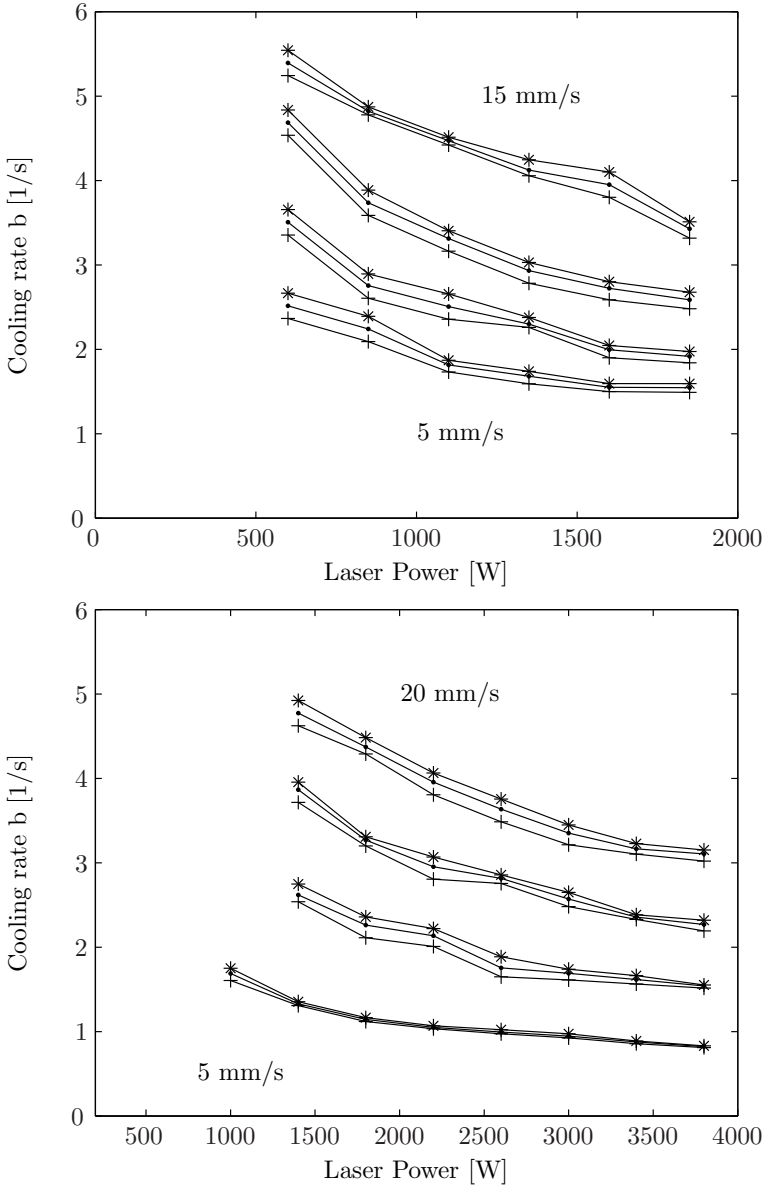


Figure 7.22: Cooling rate as function of the varied process settings. Top: 3.0 \varnothing spot, speed levels (15,10,7,5 mm/s). Bottom: 4.5 \varnothing spot, speed levels (20,15,10,5 mm/s). The different symbols (*, ., +) indicate different heights ($z - 0.4, 0.0, 0.4$ mm).

Chapter 8

Feedback control system

8.1 Introduction

In this chapter the development of a controller is presented. The controller uses the real-time obtained melt pool width as sensor. The laser power is adjusted based on this information. A schematic overview of the control setup is depicted in Figure 8.1. Using a controller to adjust the laser power in real time leads to:

- Reduction of the process optimization time.
- Guaranteed bonding between clad layer and substrate.
- Compensation for changes in geometry.
- Compensation for heat accumulation.
- Minimal dilution.
- Minimal heat input and consequently limited distortions.

8.2 System identification

The dilution is determined by the main process parameters like laser power speed and powder feed. Besides these parameters, material and geometrical changes as well as the temperature of the substrate will have an influence. These influences can be considered as low frequency disturbances. These are the disturbance which require adjustment of the laser power to guarantee

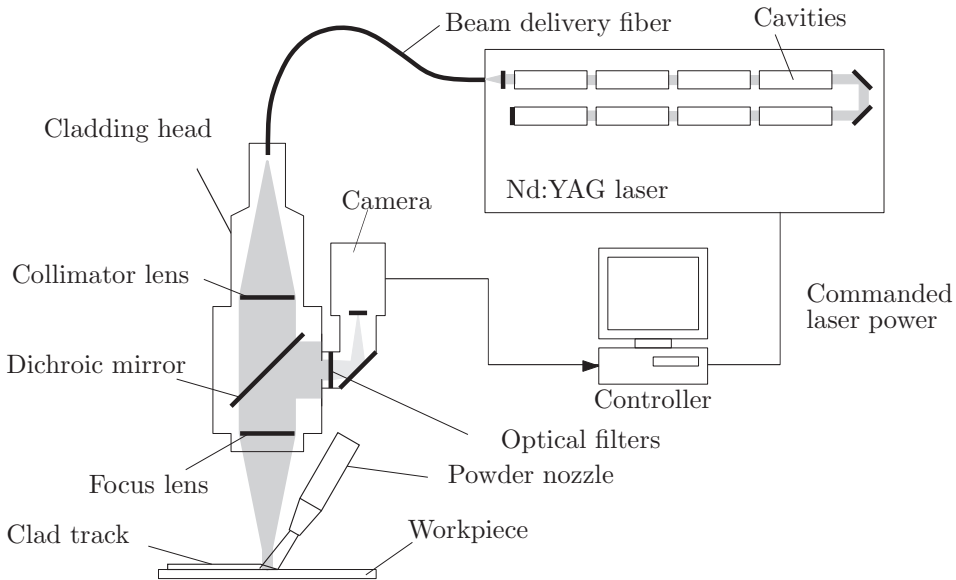


Figure 8.1: Schematic overview of the controlled laser cladding system.

the quality of the clad layer. Since they may be considered as low frequent, only the low frequency behavior of the process dynamics is of interest. The dynamic relation between the laser power and the width of the melt pool is non-linear (see Figure 8.2). In this section, first the static gain behavior of the process is discussed, followed by the low frequency behavior of the process at several operating points of the laser power. The information obtained in this section is then used for the development of a closed loop controller described in section 8.3.

Static gain

The static gain, i.e. nominal relation between laser power and melt pool width, has been investigated for several cladding speeds using a ramped laser power, increasing linearly with time from zero up to several kW. Figure 8.2 shows the measured width of the melt pool for experiments performed at cladding speeds of 5.0, 7.5, 10.0 and 12.5 mm/s. The laser beam diameter was 3 mm in these experiments. These experiments were performed with Stellite 12 as clad material, applied on a low carbon steel bar. The powder feed rate was adjusted with the cladding speed at a constant specific feed rate of 16 mg/mm. At low laser power no melt pool is formed. The power

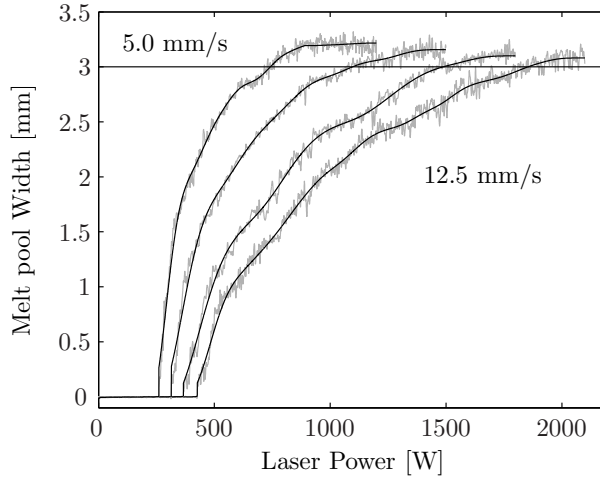


Figure 8.2: Measured melt pool width as function of laser power for four different cladding speeds.

at which a melt pool starts to be formed depends on the cladding speed and increases with higher cladding speeds. After a certain threshold the melt pool size increases rapidly. The slope of the increase in width as function of laser power, $\frac{\partial W}{\partial P}$, reduces to zero ending with a melt pool width which saturates at about 3 mm, which is close to the laser spot diameter.

Dynamic relation

The static gain depends on the laser power. Modeling the dynamics of the process is therefore difficult, as it can not be captured in a linear model. The dynamics of the process are therefore evaluated using linearization around several laser powers and cladding speeds. Since only the low frequency dynamic behavior of the process is of interest, first order discrete models were estimated. They were based on input - output data using the following Autoregressive Exogenous (ARX) model description:

$$\begin{aligned}
 A(q)y(t) &= B(q)u(t) + e(t), \\
 A(q) &= 1 + aq^{-1} \\
 B(q) &= bq^{-1}.
 \end{aligned}
 \tag{8.1}$$

Here, $y(t)$ is the melt pool width as measured using the method defined in section 5.3, $u(t)$ is the laser power and $e(t)$ is process noise. The quantity

$q^{-1}y(t)$ means the signal $y(t)$ is evaluated at its previous sample number, i.e. $y(t - ts)$, with ts the sample time. The ARX model of equation 8.1 can be expressed in the frequency domain as:

$$Plant(s) = \frac{Y(s)}{U(s)} = K \frac{1}{\tau S + 1}. \quad (8.2)$$

Here, $U(s)$ and $Y(s)$ are the frequency domain representations of the laser power and the melt pool width. Typical parameters of this model are the static gain K [mm/W] and the time constant τ [s]:

$$\begin{aligned} K &= b/(1+a) \\ \tau &= -\frac{T_s}{\log(-a)} \end{aligned} \quad (8.3)$$

with model parameters a and b as defined in equation 8.1. The gain K represents the final increase in width of the melt pool at a certain increase in the laser power $\frac{\Delta W}{\Delta P}$. The time constant is a measure for the dynamics of the system. In about 3τ the width of the melt pool will have reached within 5 % of its final value (Figure 8.3).

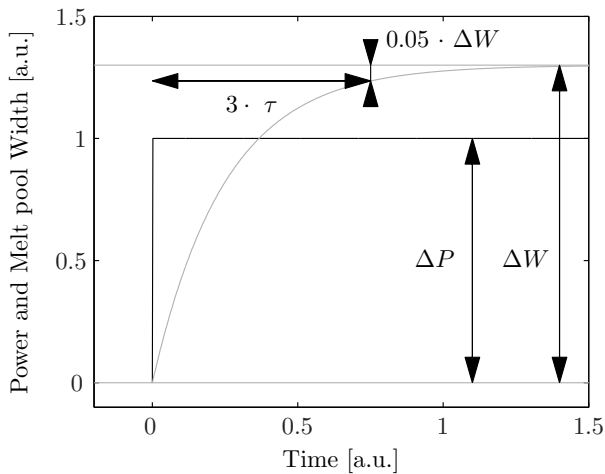


Figure 8.3: Step response of a first order system, indicating the time constant τ .

Identification experiments have been performed at a sample rate of 200 Hz with Stellite 12 as clad material on a low carbon steel bar at speeds of 5, 10, and 15 mm/s. The powder feed rate is adjusted at 16 mg/mm. For each speed, the laser power is alternated between two levels every half

second for a period of ten seconds. Figure 8.4 shows the laser power as well as the measured and model predicted melt pool width as a function of time. This experiment has been performed at a speed of 10 mm/s and a laser power of 900 ± 50 W.

The results of the identified models are given in Table 8.1. It can be

Table 8.1: Characteristic parameters of the identified models for several cladding speeds and linearization points of the laser power.

Experiment / Model number	Cladding speed [mm/s]	Laser Power [W]	K [mm/W]	τ [s/rad]
1	5	500 ± 50	6.3×10^{-3}	40×10^{-3}
2	5	700 ± 50	3.8×10^{-3}	33×10^{-3}
3	5	900 ± 50	1.9×10^{-3}	27×10^{-3}
4	10	700 ± 50	5.3×10^{-3}	29×10^{-3}
5	10	900 ± 50	3.4×10^{-3}	25×10^{-3}
6	10	1100 ± 50	2.4×10^{-3}	22×10^{-3}
7	15	900 ± 50	3.4×10^{-3}	20×10^{-3}
8	15	1100 ± 50	1.8×10^{-3}	14×10^{-3}
9	15	1300 ± 50	1.4×10^{-3}	11×10^{-3}

seen that with increasing speed the time constant τ decreases, which means that the systems response increases with increasing cladding speed. At high cladding speed the effects of conduction losses reduce. Therefore the melt pool size is faster influenced by the laser power. From the time constants it can be seen that even at the low speed of 5 mm/s, a change in melt pool width can be achieved within about 0.1 s (3τ).

8.3 Feedback controller

To control the dilution by the laser power, the system must be controllable and observable. Controllable means that an arbitrary value for the dilution, (within its boundaries) can be realized at a certain value for the laser power. Observability means that the state of the system under consideration (dilution) is measurable. This is the case when the melt pool width is used as sensor signal as evident from section 7.5 in chapter 7. An overview of the controller layout is presented in Figure 8.5. The sensor, cladding process and laser dynamics are incorporated in the Plant. The input for this Plant is the requested laser power P and the output consists of the melt pool

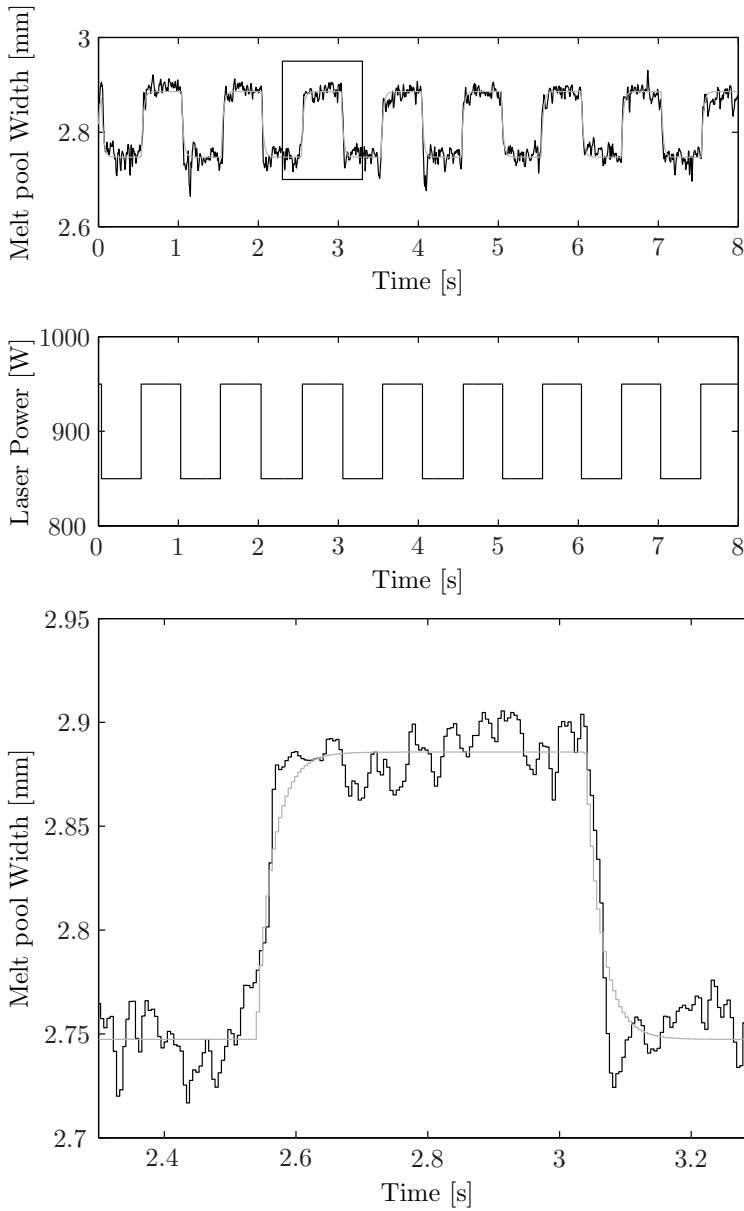


Figure 8.4: The laser power and measured melt pool width as function of the time. The bottom graph shows a detail of the upper graph.

width W as obtained from the camera image processing. Figure 8.6 shows

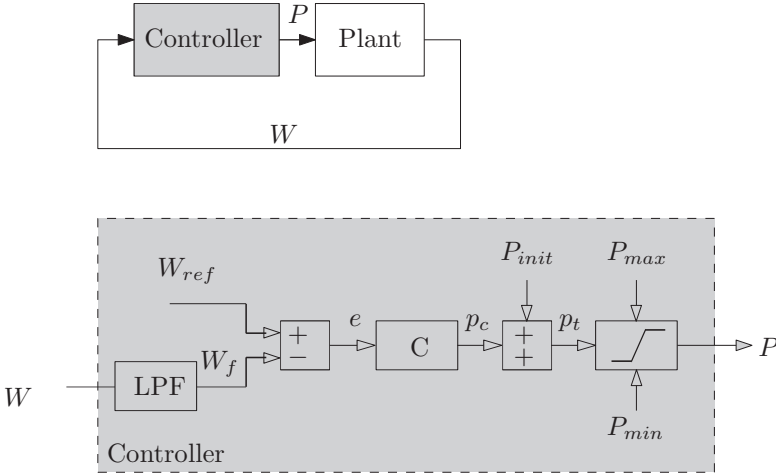


Figure 8.5: Block diagram of closed loop controlled laser cladding process (top) and the controller (bottom).

a Bode diagram of two of the Plant models from Table 8.1 (experiment 1 and 9), as well as a Bode diagram of the average model which is obtained by taking the average gain K (2.9×10^{-3} mm/W) and average time constant τ (24.5×10^{-3} s). All models show a constant gain for low frequencies. At higher frequencies the Bode diagram decays by 20 dB / decade. The phase of all the models are zero for low frequencies, and -90° at high frequencies. All of which is expected from a first order model. The output signal of the plant, i.e. the measured melt pool width W , is sent to the Controller, which subsequently calculates the required laser power input for the Plant. The lower diagram in Figure 8.5 shows the internal structure of the applied Controller. The measured width W contains high frequency noise (section 5.4 on page 61). Using a low pass filter (*LPF*), this noise is suppressed by a second order Butterworth filter as expressed in equation 8.4.

$$LPF(s) = \frac{W_f(s)}{W(s)} = \frac{\omega_c^2}{S^2 + 2\zeta\omega_c S + 1} \quad (8.4)$$

The cut-off frequency ω_c is set as 30 Hz (≈ 190 rad/s) and ζ is set as $\sqrt{\frac{1}{2}}$. The filtered melt pool width W_f is subtracted from the reference melt pool width W_{ref} , resulting in the error signal e . This signal is subsequently sent to a control filter C , which is defined in the following section. The output of this filter is added to a user selected initial laser power P_{init} , i.e. operation

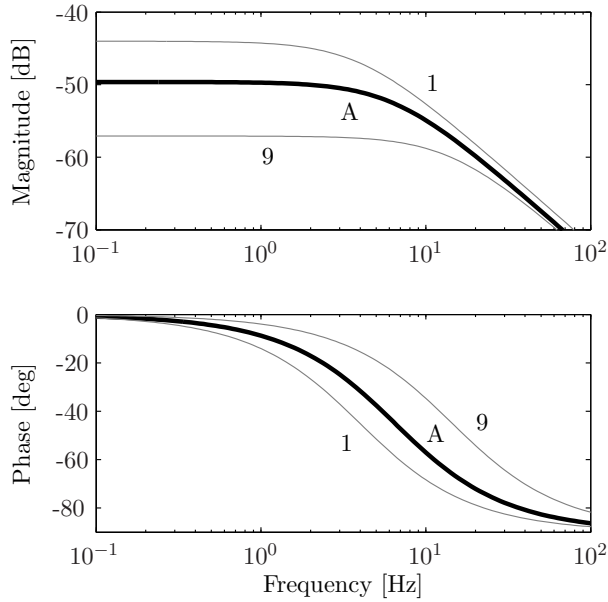


Figure 8.6: Bode diagrams for the Plant (Average (A), Model 1 and Model 9).

point and the resulting signal P_i is compared against boundary values by means of a saturation filter as expressed in equation 8.5. The calculated power P is sent to the laser power controller by an analogue signal.

$$P = \begin{cases} P_{max} & \text{for } P_i \geq P_{max} \\ P_i & \text{for } P_{min} < P_i < P_{max} \\ P_{min} & \text{for } P_i \leq P_{min} \end{cases} \quad (8.5)$$

Control filter

The control filter $C(s)$ has to guarantee that the closed loop control system remains stable at all conditions, i.e. guarantee robustness and reliability. The open loop transfer $C_{ol}(s)$ from reference input to output is expressed as:

$$C_{ol}(s) = C(s) Plant(s) \quad (8.6)$$

The closed loop transfer $C_{cl}(s)$ from reference input to melt pool width output is expressed as:

$$C_{cl}(s) = \frac{C_{ol}(s)}{1 + C_{ol}(s) LPF(s)} \quad (8.7)$$

The closed loop control system has to result in zero steady state error, i.e. after sufficient time the real melt pool width should equal the reference value. Therefore the open loop transfer $C_{ol}(q)$ should have a pure integral action, i.e. a pole at the origin [43]. From the identification experiments described in section 8.2, it is found that the Plant does not have such a pole, as the plant-pole lies somewhere between 25 - 100 rad/s ($= \frac{1}{T}$). It is therefore necessary to implement this in the control filter $C(q)$. The implemented control filter for this control system is therefore chosen as a PI controller. The corresponding filter is expressed in equation 8.8.

$$C(s) = \frac{p_c(s)}{e(s)} = Kp \frac{S + \omega_z}{S}, \quad (8.8)$$

where Kp is the gain of the control filter and ω_z is the corner frequency. At high frequencies the control filter will essentially behave like a constant, whereas at low frequencies (below the corner frequency) the control filter behaves like a pure integrator, having a phase of -90^0 . The two parameters of the control filter have to be chosen such that the closed loop system is stable and has sufficient bandwidth. The bandwidth, defined as the frequency at which the closed loop system C_{cl} has a gain of $\sqrt{0.5}$ (-3 dB), is the highest frequency at which the output of the system will still satisfactorily track sinusoidal input signals [43]. The higher the bandwidth is, the better the control system can compensate for process changes. Stability is guaranteed if the phase of the open loop transfer function does not approach -180^0 when the gain of this transfer function is 1 (0 dB).

The gain of the Plant varies considerably depending on the process settings. As seen from Figure 8.6, all the Plant models have a phase of -90^0 at high frequencies. Because of its integrator, the controller has a phase of -90^0 at low frequencies, up to the corner frequency ω_z . By choosing ω_z equal to 2 Hz (4π rad/s.), the phase of the open loop transfer function will always be larger than -90^0 . In this way, stability of the closed loop system C_{cl} is guaranteed. The gain is chosen such that the average bandwidth of the controller is about 2 Hz. This results in a controller gain Kp of 250 W/mm . As a result, the closed loop system will effectively compensate for disturbances (such as heat sink changes and speed changes) within a

fraction of a second. Figure 8.7 shows the Bode diagram for the control filter (indicated as C in figure 8.5) and the low pass filter. The real bandwidth varies depending on the Plant model between 0.6 and 6 Hz (see Figure 8.8).

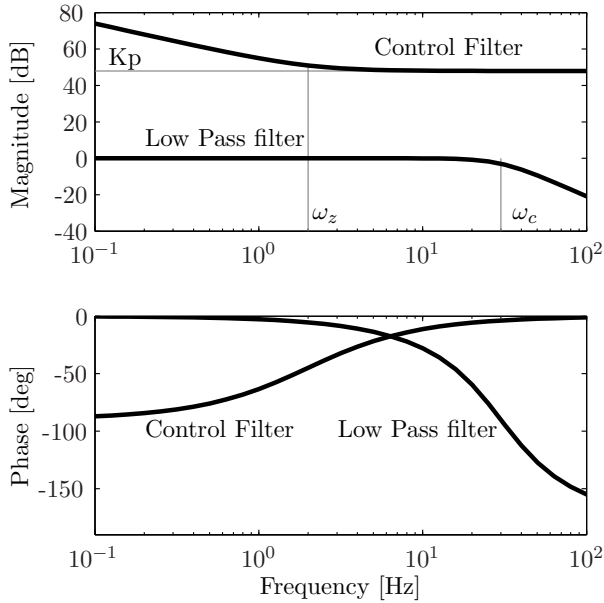


Figure 8.7: Bode diagram of the Control Filter and the Low Pass Filter (indicated as C and LPF respectively in figure 8.5).

8.4 Implementation

The controller is discretized and implemented in `C++` code, running on the WindowsTM operating system at a sample rate of about 200 Hz. When running on WindowsTM, the corresponding sample time of 5.0 ms can not be guaranteed. Due to the multitasking behavior of the operating system, the sample time varies, especially when graphical user interface (GUI) tasks are performed (at 30 Hz). Figure 8.9 shows a typical time plot and histogram of the achieved sample time. The histogram shows a clear separation between GUI updates and no GUI updates. To deal with this fluctuation, the sample time is recalculated for each sample, and the discrete filters are implemented using these varying sample times. The discretized low pass

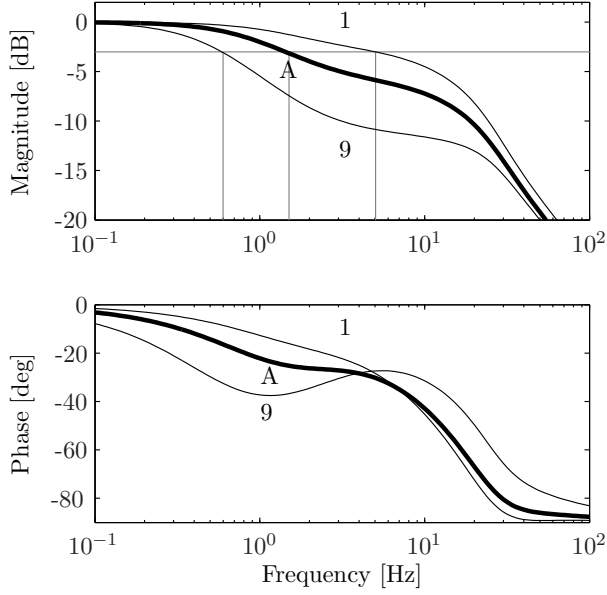


Figure 8.8: Bode diagrams of the closed loop system (Average (A), Model 1 and Model 9).

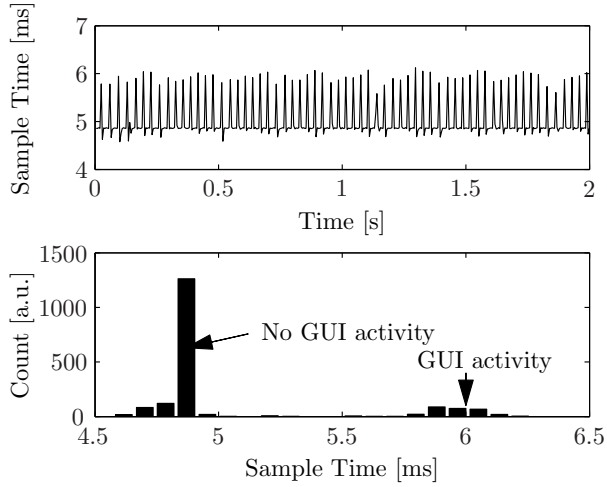


Figure 8.9: Variable sample time. Top: Sample time as a function of time, Bottom: Histogram of the sample time.

filter LPF is implemented as:

$$W_f(k) = \frac{-W_f(k-2) + \left(1 + \frac{T_s2}{T_s1} + 2\zeta\omega T_s2\right)W_f(k-1) + \omega^2 T_s1 T_s2 W(k)}{\frac{T_s2}{T_s1} + 2\zeta\omega T_s2 + \omega^2 T_s1 T_s2} \quad (8.9)$$

where T_{s_1} and T_{s_2} are the last and second last sample times and $W(k)$ and $W_f(k)$ are the input and output values at sample k .

The control filter C is implemented as:

$$p_c(k) = Kp \quad (.5\tau_i T_{s_1} + 1)e(k) + \\ Kp \quad (.5\tau_i T_{s_1} - 1) e(k-1) + p_c(k-1) \quad (8.10)$$

using T_{s_1} as applied in equation 8.9. In this way fluctuations in the sample time are taken into account.

8.4.1 Analogue signal routing

The output of the laser power controller (i.e. the requested power P) is connected to the analogue input of the laser controller. First, the laser power range (0-4000 W) is mapped between 0 and 10. This value is sent to an analogue PCI IO-card (PIO-DA4 card). This card produces an analogue voltage output between 0 and 10 V. This voltage is sent to the laser controller where it results in a power between 0 and 4000 W.

8.5 Review and conclusions

In this chapter, a feed back control strategy for the laser cladding process is developed. This control system adjusts the laser power such that the width of the melt pool is kept at a user defined reference value. The control loop uses a CMOS camera and software algorithms to obtain the width of the melt pool as discussed in chapter 5. Using a discrete control filter, the required laser power to meet the reference melt pool width is determined. This signal is sent to the laser controller using an IO-card. Robustness of the system is guaranteed by designing the phase of the open loop system in such a way that the phase of this system is always larger than -90^0 . The control filter gain is designed such that the closed loop bandwidth of the cladding process is in the order of 5 Hz. As a result, the closed loop system will effectively compensate for disturbances (such as heat sink changes and speed changes) within a fraction of a second.

Chapter 9

Controller performance

9.1 Introduction

The laser power controller as designed and described in chapter 8 is tested under various conditions. In this chapter, the performance of the controller is described. The controller acts on disturbances such as changes in the geometry as well as the material properties. The controller performance with different materials and powders is investigated as well. Full clad surfaces were produced by several overlapping clad tracks. During this process, not only the base material temperature changes, but also the thermal conductivity changes, as a part of the track is already covered by clad material from the previous pass. Several experiments were performed to investigate the influence of these variables on the required laser power.

9.2 Influence of the powder material on the controllability

In section 5.5 the influence of the powder material on the observability of the melt pool has been discussed. The required image intensity threshold value depends on the melting temperature of the powder. Now, the controllability of the melt pool width using different powders is investigated.

For control by means of the laser power, a monotonously increasing relation between power and melt pool width is required. Using the powders listed in Table 5.1 a single clad track is produced, ramping the laser power from 500 to 2500 W. The process settings for these experiments are presented in Table 9.1. Figure 9.1 shows the relation between laser power and

melt pool width for four powders. In all four cases there is a monotonously increasing relation. The powers needed to obtain the 4 mm track width, i.e. melt pool width are 1600, 1600, 1500 and 1700 W for 42C, Ultimet, 51NS and Delcrome 200 respectively.

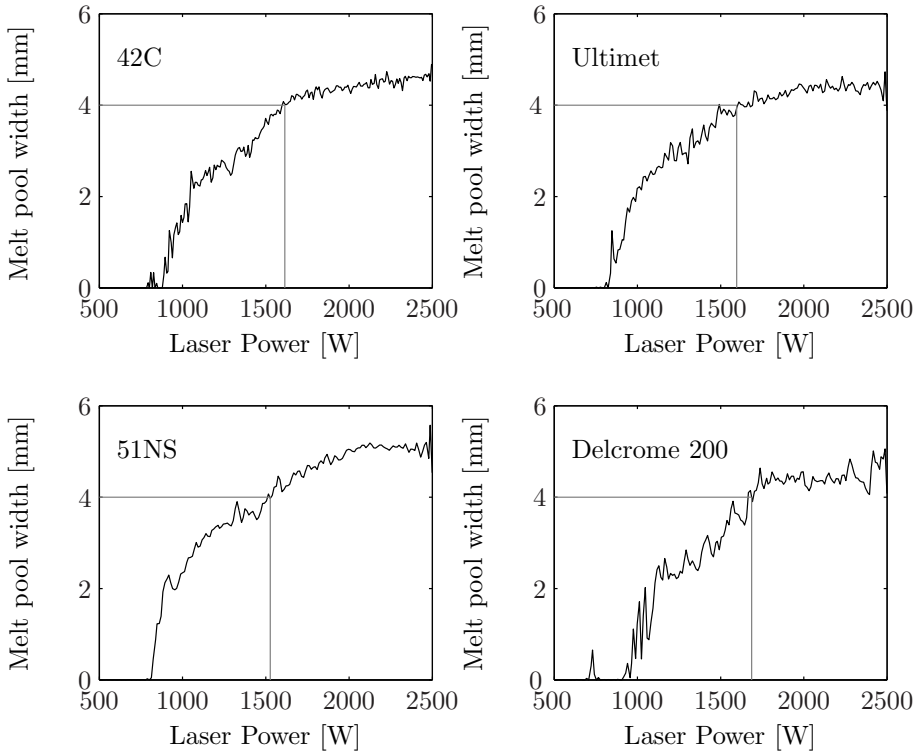


Figure 9.1: Relation between laser power and melt pool width for 42C, Ultimet, 51NS and Delcrome 200 powders on 42CrMo4 steel substrate.

With these four powders clad layers were produced. An initial laser power of 1500 W was chosen for all the experiments. The layers were produced with the feedback controller. The settings for these experiments are presented in Table 9.1. The laser power is adjusted by the controller to maintain a melt pool width of 4 mm. The melt pool width with 51NS powder shows the smallest standard deviation (see Figures 9.2 and 9.3) while with Delcrome 200, the standard deviation is the largest. This corresponds with the high fluctuations of the laser power to maintain the melt pool width. In all cases, the laser power required during the first revolution

Table 9.1: Process settings used for the experiments performed with the four different powders.

	Single track	overlap cladding
Substrate	42CrMo4 bar 35 mm \varnothing	42CrMo4 bar 35 mm \varnothing
Cladding speed	10 mm/s	10 mm/s
Melt pool width	varying	4 mm
Spot size	4.5 mm \varnothing	4.5 mm \varnothing
Laser power	500 - 2500 W in 8 s.	1000 - 1600 W
Overlap ratio	N.A.	33 %
Track /Layer width	0 - 5 mm	30 mm

of the cylindrical steel substrate is much higher than those needed for the successive tracks. Except for Delcrome 200, at around $t = 10$ s the laser power shows a local minimum. This is because of the overlap, which at this point is close to 100 %. In all cases the laser power reduces gradually by about 200 W. At the end, the overlap ratio increases from 33 to 100 %. Due to this change, the laser power reduces rapidly in all cases.

9.3 Controlled cladding of a thin steel plate

Figure 9.4 shows a photograph of a clad layer onto a steel plate substrate. Three successive tracks are produced in an *S*-shaped pattern. The process conditions for this experiment are given in Table 9.2. This experiment demonstrates the influence of the successive clad tracks on the heat flow and therefore the required laser power.

The laser power is adjusted by the controller to meet a required melt pool width $W_{reference}$ of 2.6 mm. An initial power of 1500 W was chosen. Due to heat accumulation in the substrate the required laser power reduces already significantly during the first track, as can be seen in Figure 9.5. This is caused by the temperature increase of the sample. At the first turning point, ($t = 7$ s) the melt pool width increases slightly, due to the reduced clad speed when changing the direction. The second track requires far less energy. This is partially caused by the residual heat of the previous track, but more importantly, it is caused by the 30% overlap with the previous track. Since the previously deposited clad material has a lower heat conductivity, it reduces the heat losses to the base material. As can be seen from Table 9.2, also the melting temperature and the specific heat

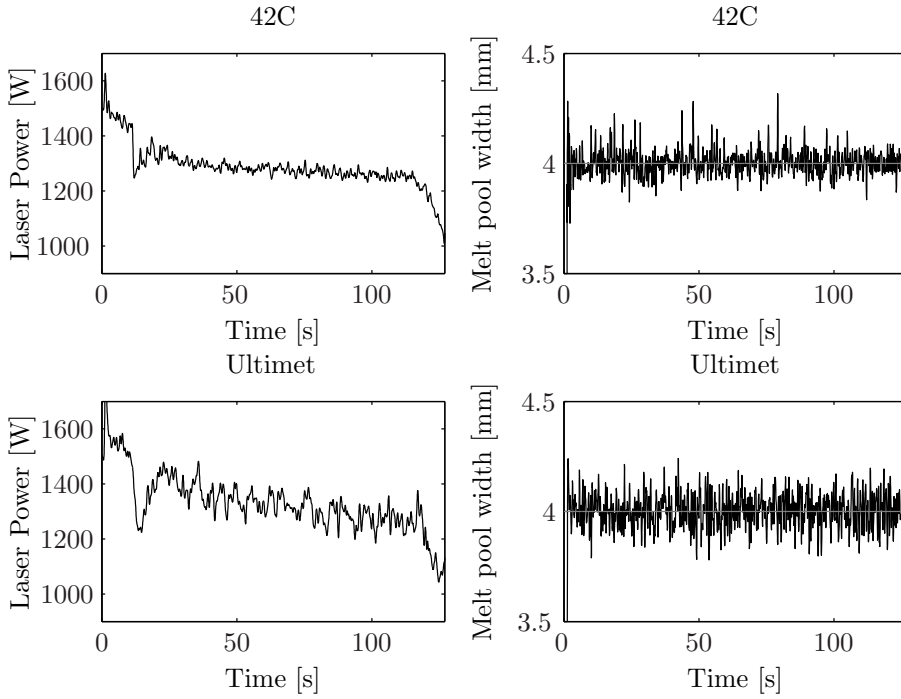


Figure 9.2: Laser power (left) and melt pool width during the cladding of a 30 mm wide overlapped clad layer on a steel bar using two different powders.

of the base material are higher than the clad material. These factors, as well as a change in geometry, contribute to a decrease in laser power. In about half a second, the laser power is adjusted to meet the required melt pool width again. At the third track a more or less steady state situation is reached, causing only minor changes in the laser power. This experiment demonstrates that the controller is capable to respond to changes during the process by adjusting the laser power within a second.

9.4 Influence of heat accumulation and geometry changes

The geometry and therefore the heat sink capacity of the substrate material often changes during cladding. In this section the ability to control the dilution with respect to such disturbances is investigated. The exper-

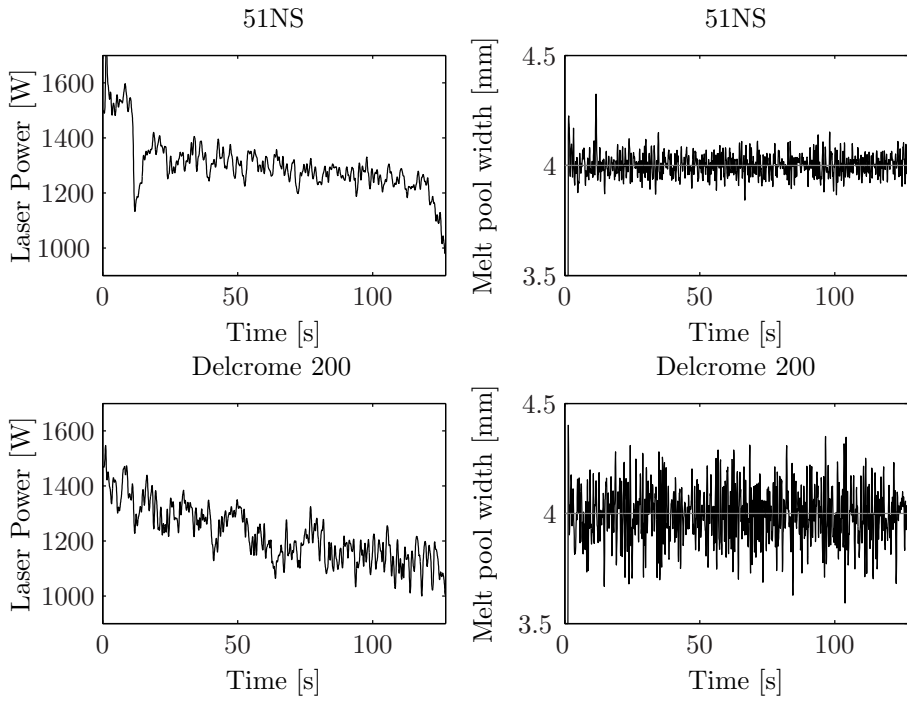


Figure 9.3: Laser power (left) and melt pool width (right) during the cladding of a 30 mm wide overlapped clad layer on a steel bar using two different powders.

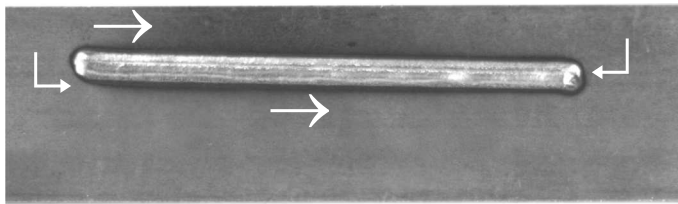


Figure 9.4: Photograph of the triple track experiment (Top view). Starting point: Upper left. End point: Lower right.

periments involve cladding of Stellite 12 on a 42CrMo4 steel bar with a 4.5 mm diameter Top-hat laser spot. The cladding speed is kept constant for all the experiments. Figure 9.6 shows the substrate bar geometry. A hole is drilled in the solid bar to change the heat sink capacity. The dimensions of the resulting bar are presented in Figure 9.6 as well. The wall thickness

Table 9.2: Material properties and process parameters used during the triple track experiment.

Plate material	low carbon steel
Plate dimensions	150×40×3.0 mm
Plate thermal conductivity	46 W/m/K
Plate specific heat	460 J/kg/K
Plate melting temperature	1510° C
Cladding speed	10 mm/s
Powder material	Stellite 6
Specific powder feed rate	16 mg/mm
Powder thermal conductivity	14.4 W/m/K
Powder specific heat	423 J/kg/K
Powder melting temperature	1395 ° C
Carrier / shielding gas	Nitrogen
Laser Spot size	3 mm Ø
Target melt pool width	2.7 mm

of the resulting tube is 2.5 mm. This means a heat sink capacity of about 25 % of the solid bar. One experiments was performed on a solid steel bar for comparison.

First, the monitoring system was calibrated to obtain the optimal threshold ($T_{threshold}$) of the camera images corresponding to the melt temperature. Secondly, the requirement for control is investigated, i.e. the progressive relation between the laser power and the melt pool width. Next, several overlap cladding experiments were performed to demonstrate the effectiveness of online regulation of the laser power. Table 9.3 shows the settings for all the experiments.

9.4.1 Determination of the melt pool width

To determine the width of the melt pool from the camera images, first the scale ratio between real dimensions and camera image dimensions was determined. This value was 10.25 mm/pixel.

A single clad track was produced onto a solid bar using the process settings as presented in Table 9.3 (experiment 1). The monitor system is used to measure the melt pool width. The pixel intensity value which corresponds to the melt temperature ($T_{threshold}$) was determined. The average width of the produced track single clad track was measured to be 4.12 mm.

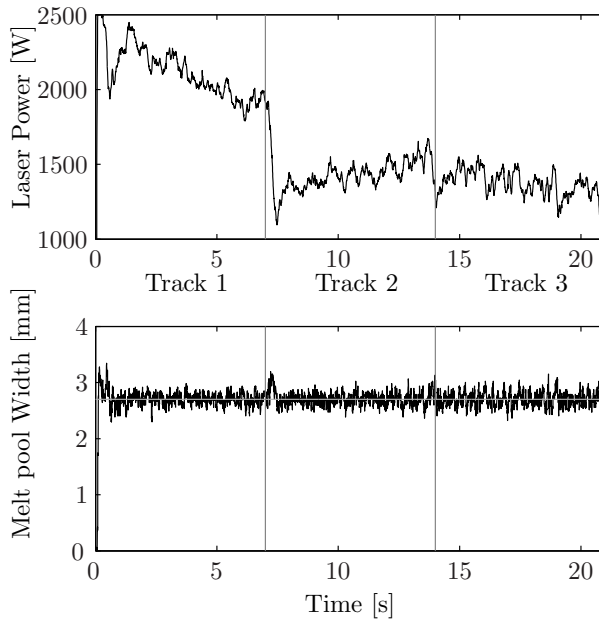


Figure 9.5: Laser power and melt pool width as function of time for the triple clad track experiment.

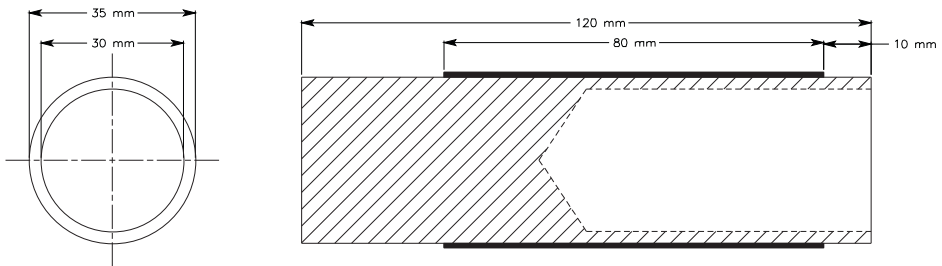


Figure 9.6: Changing heat sink capacity due to partially drilled hole. Also indicated is the clad layer.

The calculated width for all possible pixel threshold values is presented in Figure 9.7. A pixel intensity value of 134 corresponds to the melt temperature, since the width as obtained from the camera images after image processing equals 4.12 mm in this case.

Table 9.3: Process settings used in the bar / tube experiments.

Experiment number	1	2	3	4	5	6
Spot diameter [mm]	4.5	4.5	4.5	4.5	4.5	4.5
Laser power [W]	1600	500-4000	Controlled	1100	1400	Controlled
Melt pool width [mm]	varying	varying	4.1	varying	varying	4.1
Cladding speed [mm/s]	10	10	10	10	10	10
Substrate bar	42CrMo4 solid bar	42CrMo4 Solid bar	42CrMo4 Solid bar	42CrMo4 varying	42CrMo4 varying	42CrMo4 varying
Substrate geometry						
Clad powder	Stellite 12	Stellite 12	Stellite 12	Stellite 12	Stellite 12	Stellite 12
Specific powder feed rate [mg/mm]	34.0	34.0	34.0	34.0	34.0	34.0
Number of tracks	1	1	42	28	28	28
Layer width [mm]	4.12	0-4.8	4.1	4.1	4.1	4.1
Overlap ratio	n.a.	n.a.	34 %	34 %	34 %	34 %
Cladding time [s]	8	8	450	300	300	300

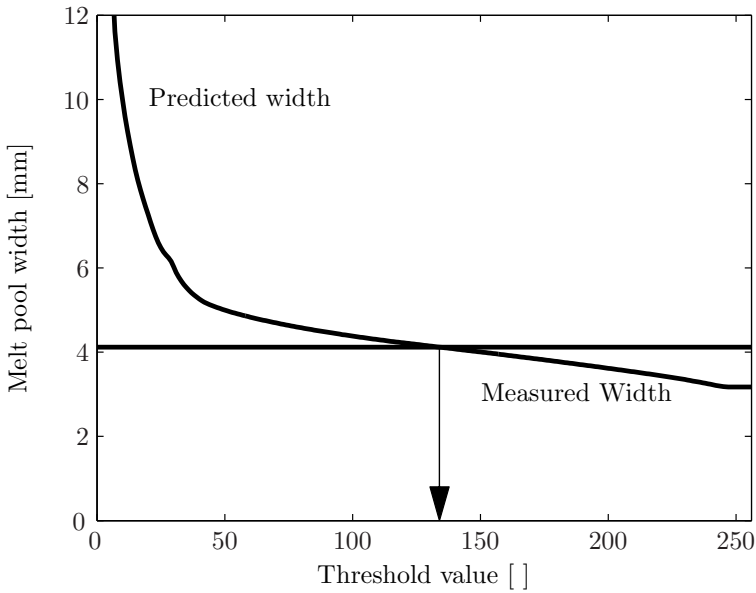


Figure 9.7: Threshold value versus predicted melt pool width.

9.4.2 Monotonous increasing relation between laser power and melt pool

To control the width of the melt pool by means of the control strategy as discussed in chapter 8 requires a monotonous increasing relation between the laser power and the width of the melt pool. To investigate such a relation, a single track was produced, by ramping the laser power from 500

to 4000 W in 8 seconds (experiment 2). Figure 9.8 shows the result. At low laser powers no melt pool is formed. From about 1000 W and up, the required progressive relation is present. The width of the melt pool increases to about 4.8 mm. This is larger than the laser spot diameter. With further increasing of the laser power, the detected width of the melt pool reduces. In Figure 9.8 the top-right corner shows that the brightness of the melt pool is not uniform. This is caused by the increasing melt pool flow resulting in excessive dilution. As long as the laser power is below 2000 W the required monotonous increasing relation exists. For successful control, this implies that starting with a initial laser power of about 1500 W, and aiming for a melt pool width of about 4.1 mm is sufficient.

9.4.3 Controlled cladding on a solid bar

A layer of about one millimeter in thickness was cladded onto a solid bar (experiment 3). An initial laser power of 1500 W was used. The laser power and melt pool width as function of time during the cladding of this bar is presented in Figure 9.9. As soon as a melt pool has developed, the control system adjusts the laser power to a melt pool width of 4.1 mm. Initially, a laser power of about 1600 W was required. After one revolution (about 10 seconds) the required laser power has reduced down to about 1500 W. Due to the long time of the cladding, the bar temperature increased significantly. Due to this heat accumulation the required laser power reduces significantly. The decay in laser power is almost exponential, saturating at a laser power of 1100 W. This power is the steady state laser power. In chapter 7 it was shown that with a melt pool width below 4.2 mm, no significant dilution of substrate material into the clad layer occurs. Since during this experiment the melt pool width is kept at 4.1 mm, no significant dilution is expected. Figure 9.10 shows cross-sections of the produced clad layer. The two sections are from the first and second part of the track. As this figure shows, indeed no significant dilution has occurred. From the beginning up to the end of the layer, a constant small substrate layer has been melted. The heat affected zone increases somewhat caused by the overall increased temperature of the substrate. In Figure F.1 in appendix F more details of the layer can be found.

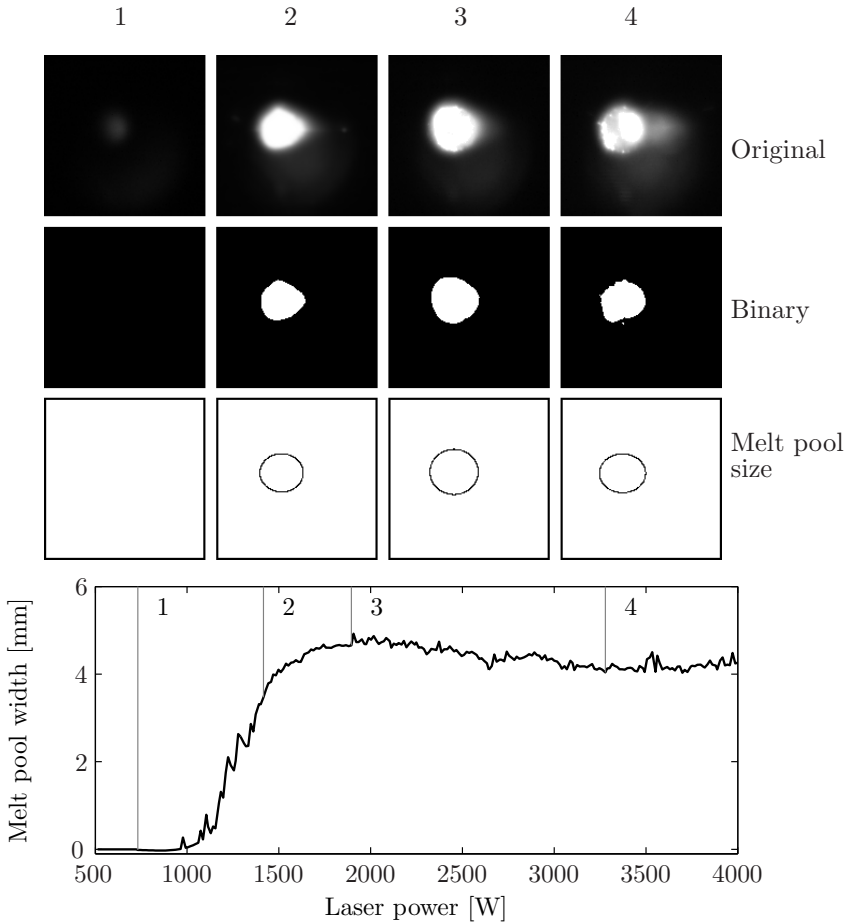


Figure 9.8: Melt pool width as function of the laser power. The original images (top) and the processed images (center) are shown along with the fitted elliptical shapes (bottom).

9.4.4 Fixed laser power cladding on a bar with changing geometry

From the previous experiment it is found that a fixed laser power of 1100 W results in a melt pool width of 4.1 millimeter after the substrate has reached a steady state temperature. Such a laser power however, will be insufficient at the beginning of the cladding process. Two clad layers were produced on a substrate with varying geometry as indicated in Figure 9.6. The first experiment involves a fixed laser power of 1100 W (experiment

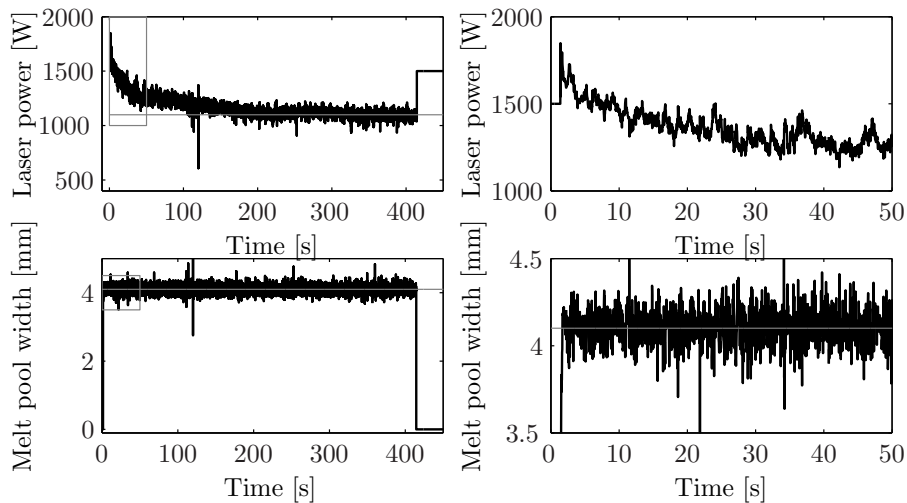


Figure 9.9: Laser power and melt pool width as function of time during controlled cladding on a solid bar. On the right side details of the first few seconds of the power and width are presented.

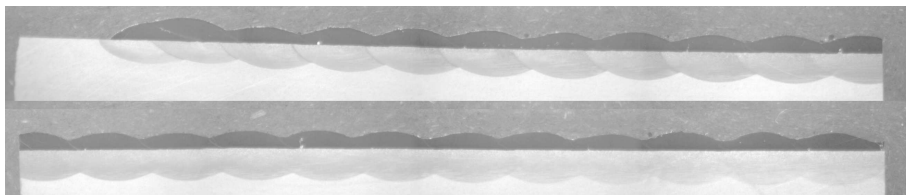


Figure 9.10: Cross-section of the clad layer of experiment 3.

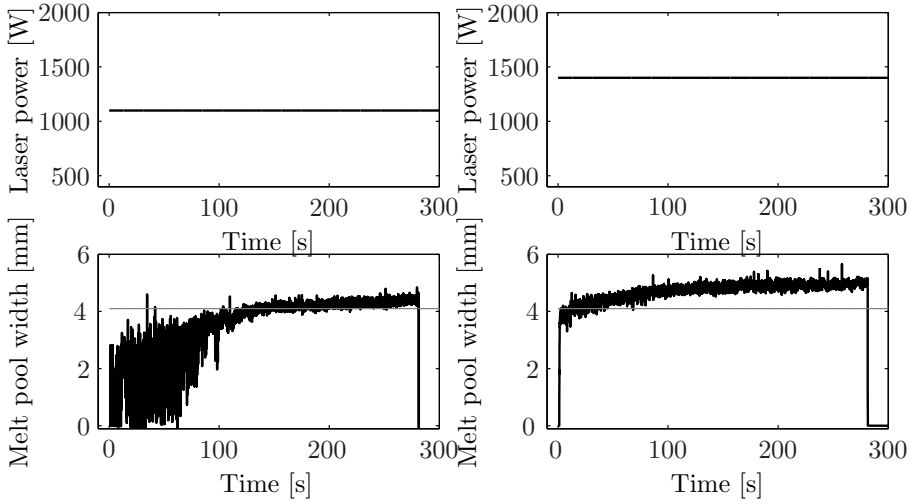


Figure 9.11: Laser power and melt pool width as function of time during cladding onto a varying geometry bar. Left, the laser power is lower, resulting in smaller and more unstable melt pool widths.

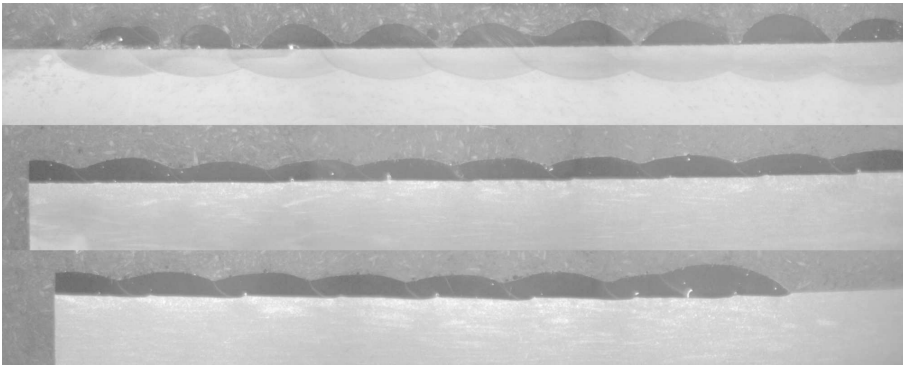


Figure 9.12: Cross-section of the clad layer of experiment 4.

4). The second clad layer was produced using a somewhat higher power of 1400 W (experiment 5).

Figure 9.11 shows the width of the melt pool as function of the time during these cladding experiments. With a power of 1100 W, a small and highly fluctuating melt pool width is obtained during the first half of the cladding time. This is due to the low temperature of the substrate. The melt pool width increases and becomes more stable over time. After about 120 seconds of time, the melt pool width has reached a value of 4.1 mm. This coincides with the change in geometry. From this point up, the width increases only slightly. The cross-sections of the produced layer shown in Figure 9.12 indicate that 1100 W is insufficient to form a continuous clad layer. However, near the end of the bar, where the bar has only a thickness of 2.5 mm, some melting of the substrate material is observed.

With a laser power of 1400 W a stable melt pool width of about 4 mm is realized immediately from the beginning. Over time, this width increases slowly up to about 5.0 mm. Figure 9.13 shows cross-sections of the clad layers. A power of 1400 W results in a stable clad layer. However, over time the dilution increases. Close to the end, a dilution of 50 % has been obtained. In the Figures F.1 and F.2 in appendix F more details of these layers can be found.

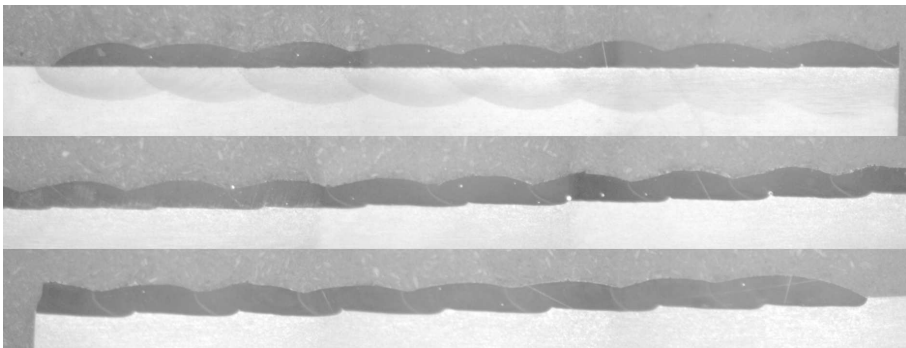


Figure 9.13: Cross-section of the clad layer of experiment 5.

9.4.5 Controlled cladding on a bar with changing geometry

As the previous section demonstrated, using a constant laser power is not adequate. Either the dilution levels reach unacceptable high values toward the end of the bar due to overheating, or the clad tracks are irregular due

to a lack of energy close to the beginning. Real-time adjustment of the laser power is not optional but mandatory in such situations. Analogue to experiment 3, a clad layer was produced in experiment 6 by adjusting the laser power to maintain a melt pool width of 4.1 mm. Figure 9.14 shows both the laser power and melt pool width in this situation. During the first minute, the laser power reduces almost identical to experiment 4. While that experiment showed a steady laser power of about 1100 W is reached after a few minutes of cladding, in this situation a continuous reduction in the laser power is observed. After about 5 minutes the laser power has reduced to 800 W, a reduction of about 50 %. Note that the dilution over the entire layer is uniform and small (Figure 9.15).

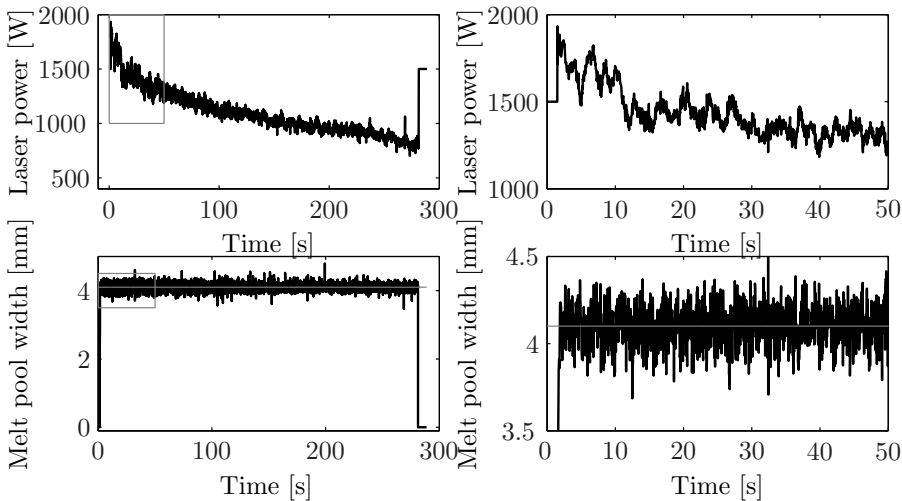


Figure 9.14: Laser power and melt pool width during controlled cladding on a bar with varying dimensions. On the right side details of the first 50 seconds are presented.

9.4.6 Hardness in clad layers with respect to control of dilution.

As already shown in section 7.4, the hardness of clad layers is strongly affected by the dilution. The dilution increases over time with a constant laser power. By controlling the laser power to maintain a constant melt pool width, the dilution was kept minimal over the entire clad layer. From both the layers of experiment 5 and 6 (Table 9.3) three hardness profiles

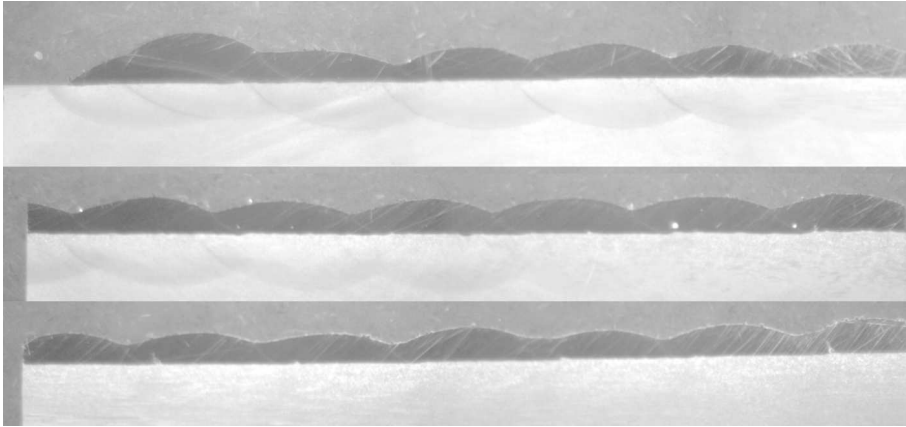


Figure 9.15: Cross-section of the clad layer of experiment 6.

have been measured. The first is close to the beginning of the layer. The second is close to the center and the last one is near the end of cladding. The hardness as function of the depth for all three locations of experiment 5 (fixed laser power) is presented in Figure 9.17. The hardness of the substrate material is about 400 HV0.2 which is typical for a 42CrMo4 steel. In the clad layer, the hardness varies considerably. At the begin of the clad layer (Figure 9.16 marked with asterisks), the hardness increases from about 540 HV0.2 near the original substrate surface up to 640 HV0.2 near the clad surface. The hardness near the center of the track is considerably lower at 570 HV0.2. The substrate-clad layer interface is shifted slightly to the left due to an increase in the dilution. Near the end of the track, the average hardness of the clad layer is further reduced to 480 HV0.2, which is 25 % lower than at the beginning of the clad layer. The dilution as observed in experiment 6 is minimal over the full length of the clad layer. In Figure 9.17 the hardness of this layer at three locations (begin, center and end of the bar) is presented. The hardness in the substrate is about 400 HV0.2. The hardness in the clad layer is about 610 HV0.2 for all three measurement locations. Both experiments clearly show that a constant laser power will not lead to constant clad properties. On the other hand, controlled laser power as shown here enables constant clad quality.

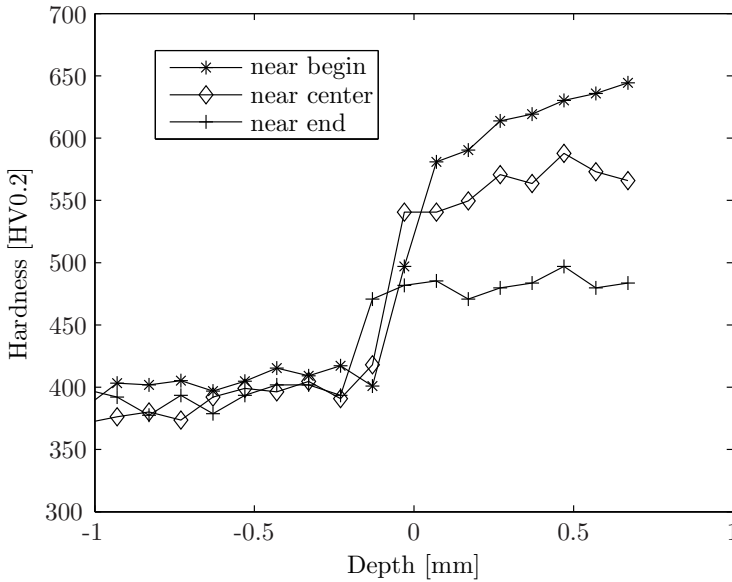


Figure 9.16: The hardness as function of the depth from the original substrate interface for three locations along the clad layer of experiment 5. (fixed laser power)

9.5 Review and conclusions.

This chapter described the performance of the control system. Several experiments were performed, investigating the influence of the powder material, changes in the geometry and the heat accumulation. The main conclusions are:

- The melt pool with is successfully controlled by adjusting the laser power by the controller.
- The controller performs well independent of the powder material used.
- The controller successfully adjusts the laser power to compensate for changes in the heat conduction
- Changes in the substrate geometry and temperature make it necessary to adjust the laser power.
- A constant laser power leads to an excessive dilution and reduced hardness of the clad layer towards the end due to heat accumulation.

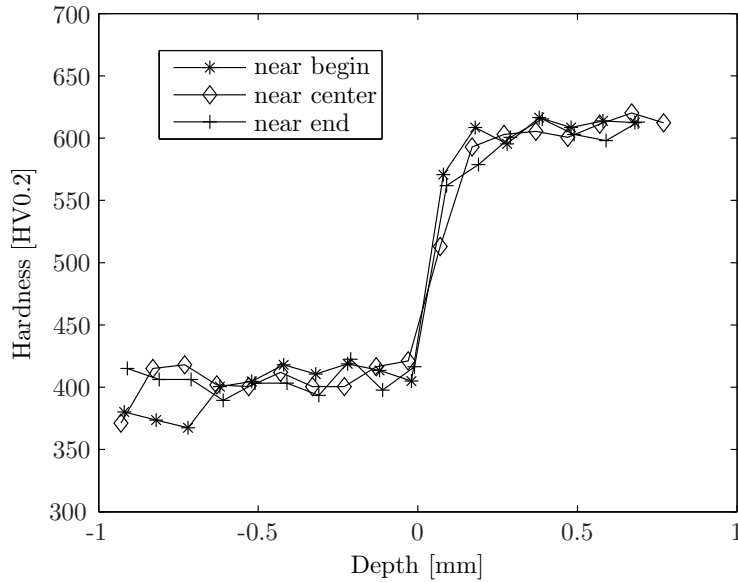


Figure 9.17: The hardness as function of the depth from the original substrate interface for three locations along the clad layer of experiment 6. (real time adjusted laser power)

- With the controller, the laser power is adjusted for such heat accumulation, resulting in a reduction of the power by 50 %. Due to this reduction, the dilution is kept constant over the entire clad layer. The hardness of the layer remains constant as well.

Chapter 10

Industrial implementation of the controller

10.1 Introduction

The feedback controller which is developed in this research and presented in chapter 8, was implemented at the industrial company Stork Gears & Services (SG&S), Rotterdam, The Netherlands. The goal was to obtain a constant high quality of clad layers as shown in chapter 8.

This chapter describes the implementation of the controller and its performance in practice. Section 10.2 describes the cladding setup. Section 10.3 discusses the influences of the powder feed and laser wavelength on the optical emission. Section 10.4 describes the implemented controller while section 10.5 describes the performance and robustness of the controller.

10.2 Laser cladding setup

The laser cladding department of Stork Gears & Services applies a 2 kW Laserline (LDF2000) diode laser. The laser light is transported to the process area by a 1.0 mm diameter fibre. A commercial cladding head from the Fraunhofer institute ILT, Aachen focusses the laser beam onto the workpiece. This cladding head has a 50 mm collimator and 150 mm focussing lens. At the focus plane an image of the fibre end gives a Top-hat spot of 3 mm in diameter. The powder feed is provided by GTV type PF 2/1 hopper system from GTV Verschleiss-Schutz GmbH Germany with a 3 mm transport tube. The powder is blown into a melt pool coaxially by nitrogen

gas. The majority of the products which need local repair by means of laser cladding are rotationally symmetric. A turn table is used for the rotational movement of the products while a manipulator with two degrees of freedom, on which the cladding head is mounted, provides the radial and longitudinal movements. The entire system is controlled by software and hardware which is developed by SG&S. For non-rotational parts, an industrial robot from Cloos Schweisstechnik with six degrees of freedom can be used. In that case, the cladding head is mounted on the robot. Figures 10.1 and 10.2 show these setups. A CCD camera is integrated into the system and looks coaxially at the melt pool.



Figure 10.1: Cladding setup of SG&S using a turn table.

10.3 Optical path and process radiation

Compared to the setup described in this thesis, the cladding installation at SG&S is quite different (different laser, different powder delivery system). The diode laser has four 500 W diode packs. Two of them operate at an wa-

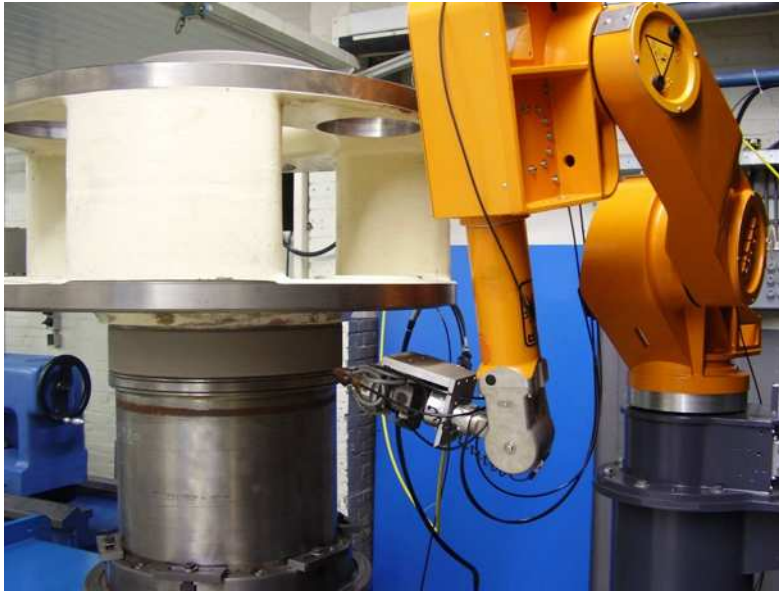


Figure 10.2: Cladding setup of SG&S using a robot.

wavelength of 940 and the other two at 980 nm. The powder delivery is done coaxially. As a consequence, the powder passes through the laser beam for a considerable longer time. This was expected to have an influence on the observability of the melt pool. To investigate this, spectroscopic measurements are performed. The spectrometer which is described in chapter 5 was mounted on the cladding head instead of the CCD camera.

The intensity of the reflected laser light is much stronger than the temperature radiation from the melt pool. Since the spectrometer has a relatively low signal to noise ratio (300:1), both components have been measured individually. The Figures 10.3 and 10.4 show the results. In the first situation, a melt pool was created without any powder supply while in the second situation the powder feed was switched on. This results in a reduction in the intensity of the radiation which equals to 16 % and 29 % for the laser and the melt pool radiations respectively. Clearly visible in Figure 10.3 are the two wavelengths of the diode laser at 935 and 975 nm. Note that the reflected laser radiation exceeds the process emission by a factor 10^4 . It is therefore necessary to suppress the laser radiation by an optical filter. Based on these measurement, a filter was selected which transmits the radiation to 800 nm while suppressing all higher wavelengths (FES0800

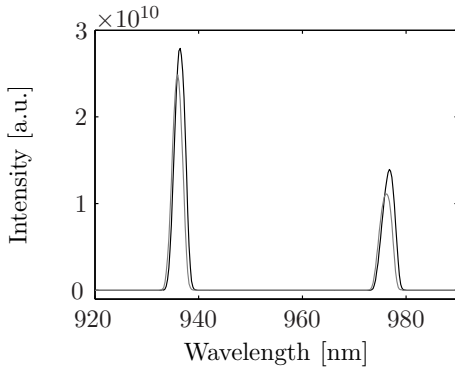


Figure 10.3: Spectroscopic measurements of the laser radiation. Black: no powder, gray: width powder.

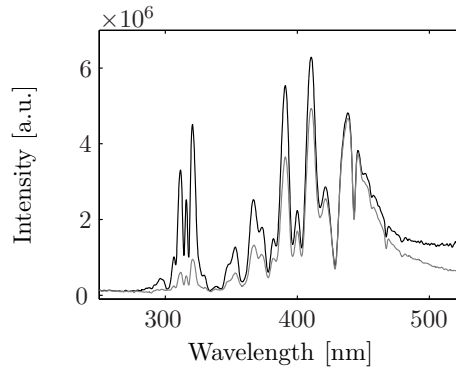


Figure 10.4: Spectroscopic measurements of the melt pool radiation. Black: no powder, gray: width powder.

filter from Thorlabs). Figure 10.5 shows the transmittance of this filter which has a transmittance less than 0.01% between 836 and 1040 nm. When using this filter the contribution of the laser radiation to the total intensity is about 2% which is considered insignificant.

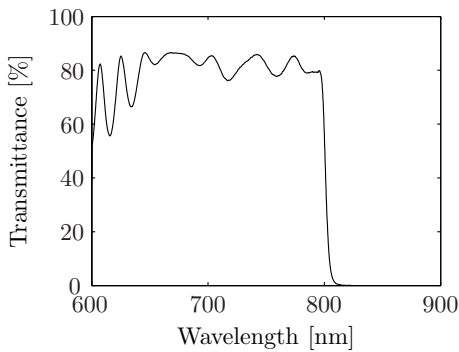


Figure 10.5: Transmittance of the FES0800 filter.

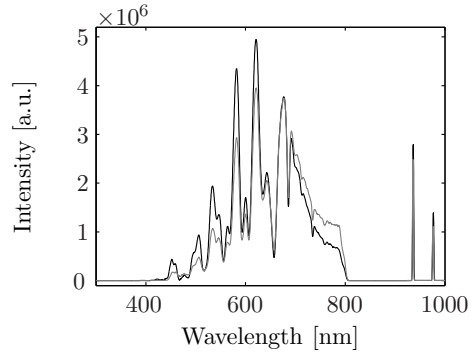


Figure 10.6: Spectroscopic measurement of the melt pool (300 - 850 nm) and laser radiation (940, 980 nm) after passing through the FES0800 filter. Black: no powder, gray: width powder.

Images of the melt pool were obtained by a PL-B741F firewire camera

from Pixelink. This camera has the same sensor chip as the one used in the monitoring and control system in chapter 5. Figure 10.7 shows the optical system including this camera.

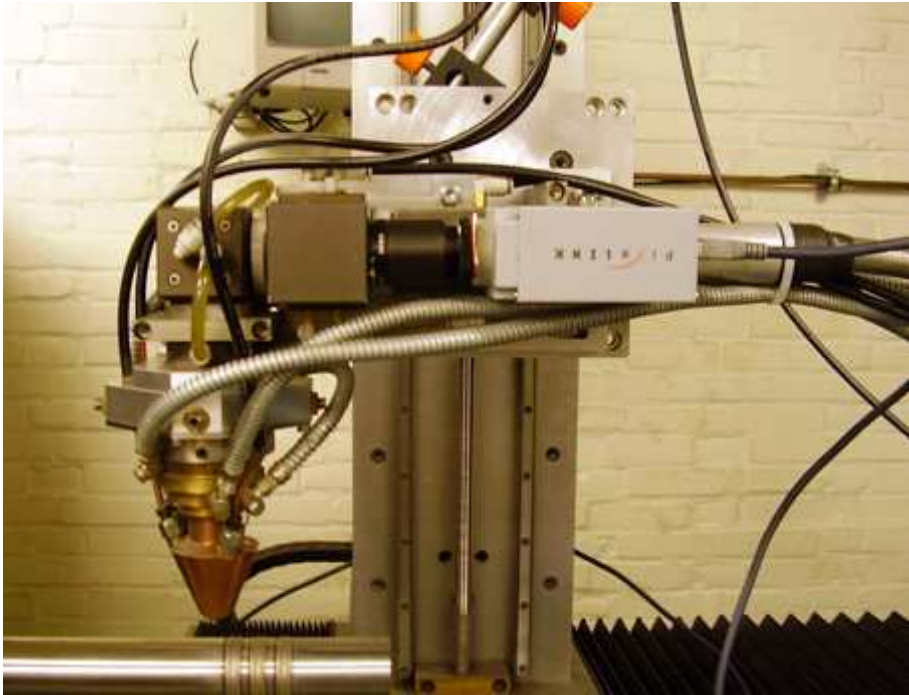


Figure 10.7: Optical system including the camera.

10.4 Controller system

The control system runs on a personal computer using WindowsTM as operating system. The Pixelink camera is connected to this computer. An IO-card provides an analogue output to the laser controller. The laser power control software, (Figure 10.8) which is specially written for this purpose, allows the laser to operate in two modes. The first mode allows to run the laser in feed forward mode (no control) so that a constant laser output can be selected. The second mode allows adjusting the laser power by means of the real-time control strategy as developed in chapter 8. This software enables the user to store relevant data and images of the melt pool dimensions as function of time for later reference and quality report.

Besides the main GUI of the program two additional windows are used. The first one shows images of the melt pool at a frame rate of 30 Hz. The second one shows a graphical representation of the laser power and melt pool dimensions as a function of the time. These windows allow for online viewing by the operator.

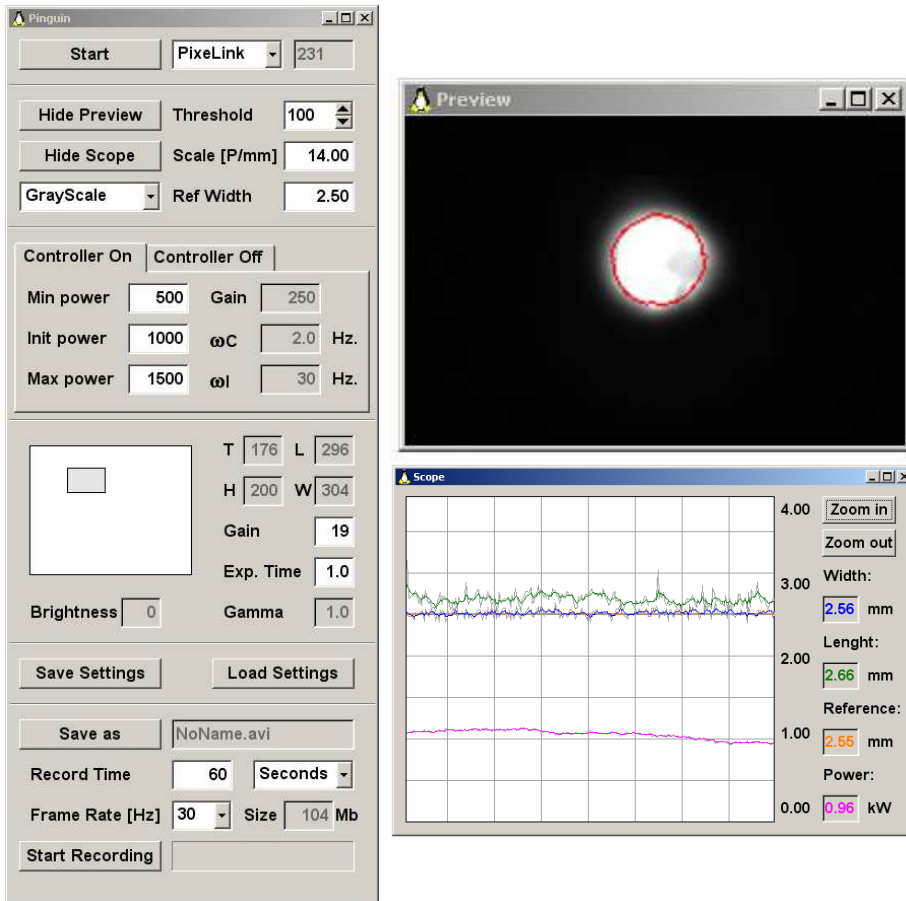


Figure 10.8: The control software which is developed as part of this research work. On the left side the main windows is shown. On the right side the preview and scope windows are shown.

The laser power control system does not interfere with any of the other machinery which is used at SG&S cladding facilities and enables easy handling by any operator (Figure 10.9). A master pc controls the movements of the product and the cladding head by sending set-points to the servo-

controllers. The master pc also switches the laser on and off. The control software acts as follows. While the laser is switched off, the control software requests a constant laser power (null power) from the laser. After the laser switches on, the control software will detect the presence of a melt pool and starts to analyze the width of the melt pool and compare this value with the reference melt pool width and controls the process. As soon as the laser has been switched off by the master pc, The control software program will detect the absence of a melt pool and the null laser power is requested from the laser controller again. The control software now goes to stand by mode waiting for the laser to be switched on again.

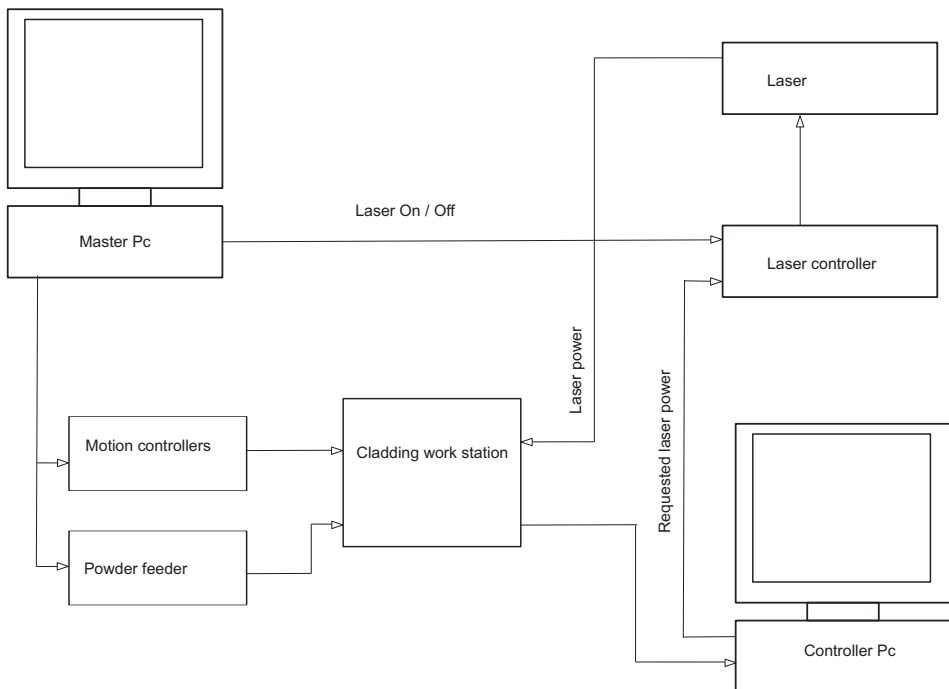


Figure 10.9: Schematic representation of the cladding system architecture and operation flow.

10.5 Controlled cladding

Several experiments were performed to check the performance in practice. The objectives of these experiments were to:

- Investigate whether the chosen optical filter suppresses the laser radiation satisfactory.
- Investigate the influence of the coaxial powder supply on the observability of the melt pool.
- Find the optimal settings for the controller.
- Investigate whether the required progressive relation between melt pool width and laser power exists.
- Investigate whether the controller can determine the required laser power in a stationary situation.
- Investigate whether the controller responds and correctly adjusts the laser power in case of disturbances.

10.5.1 Observability of the melt pool

The observability of the melt pool as well as the influence of the powder jet on this observability were checked. The process settings and used materials are presented in Table 10.1.

Table 10.1: Process settings.

	Experiment 1	Experiment 2	Experiment 3
Substrate material	42CrMo4	42CrMo4	42CrMo4
Clad material	None	Delchrome 200	Delchrome 200
cladding speed [mm/s]	13.33	13.33	13.33
Laser power [W]	1000	1000	500 - 1500
Specific powder feed rate [mg/mm]	-	20.5	20.5

Figure 10.10 shows two typical images of the observed melt pool with and without powder supply. The camera gain and exposure time are optimized to give clear images resulting in a gain of zero and exposure time of 5 ms. The coaxial powder feed has no adverse effect on the observability of the melt pool.

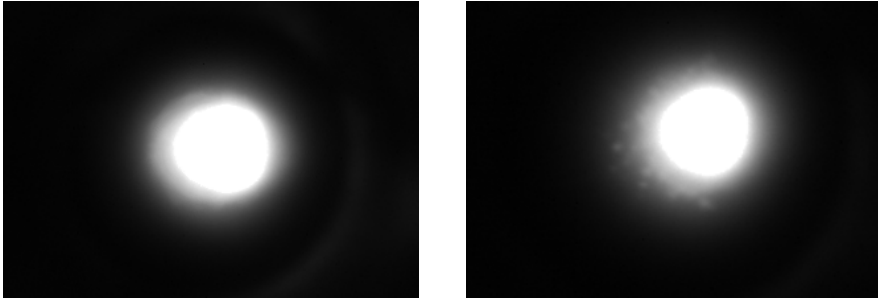


Figure 10.10: Melt pool as observed by the camera. Left: No powder supplied. Right: With powder supply.

10.5.2 Determination of the melt pool width

First the scale ratio between real dimensions and camera image dimensions was determined to be 35.2 mm/pixel. The pixel intensity value which corresponds to the melt temperature was determined using the width of the tracks (2.15 mm). The calculated widths for all possible pixel values is shown in Figure 10.11. A pixel intensity value of 128 corresponds to the melt temperature which occurs at the 2.15 mm width. This value of 128 is set as the threshold value in the controller.

10.5.3 Progressive relation between laser power and melt pool

To be able to control the width of the melt pool by means of the control strategy as discussed in chapter 8, a progressive relation between the laser power and the width of the melt pool must exist. To investigate whether such a relation is present, a single track was produced by ramping the laser power from 500 to 1500 W. Figure 10.12 shows the relation between the laser power and the melt pool width. As can be seen from this figure, at low laser powers no melt pool is formed. From about 700 W and up, the required progressive relation is present. A melt pool width of 3.5 mm can be realized. However, since the diameter of the laser spot is smaller, i.e. 3 mm, a high level of dilution can be expected if such a high melt pool width is chosen.

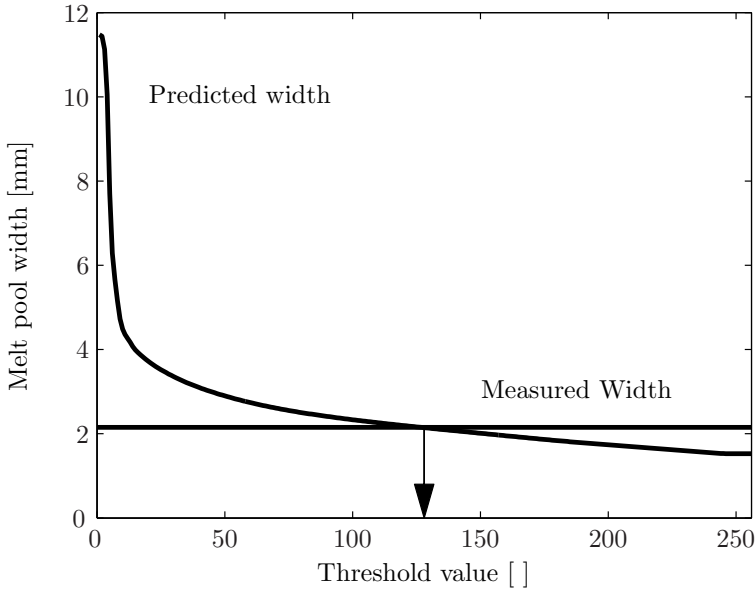


Figure 10.11: Threshold value versus predicted melt pool width.

10.5.4 Maintain a constant melt pool width

In this section, the performance of the control system to maintain a constant melt pool width is investigated. First an experiment was performed without any process disturbances. Secondly the cladding speed was disturbed by a stepwise increase. Single clad tracks were produced with the conditions presented in Table 10.2.

Table 10.2: Process settings applied for controlled cladding.

	Experiment 4	Experiment 5
Substrate material	42CrMo4	42CrMo4
Clad material	Delchrome 200	Delchrome 200
cladding speed [mm/s]	13.33	13.33 - 16.66
Laser power [W]	Controlled	Controlled
Initial laser power [W]	500	800
Melt pool width [mm]	Controlled	Controlled
Specific powder [mm ³ /mm]	2.1	2.1

Figure 10.13 on the left shows the laser power and melt pool width for

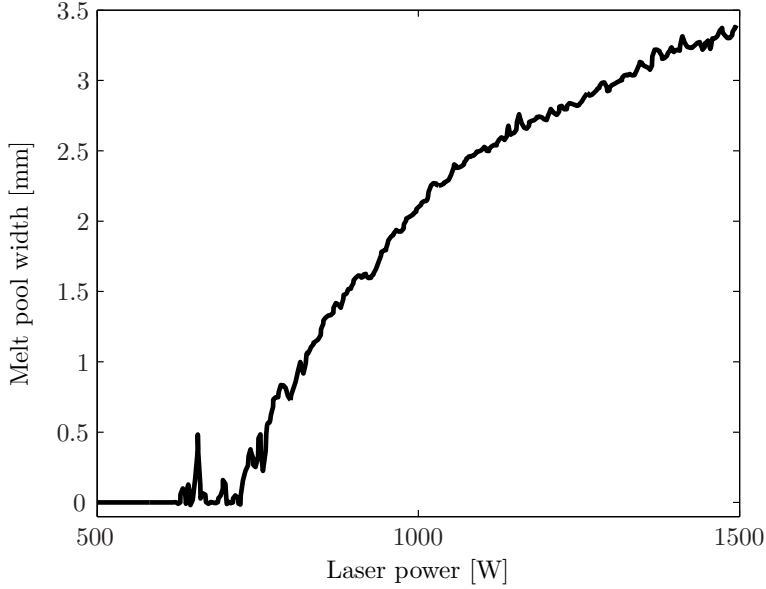


Figure 10.12: Melt pool width as function of the laser power.

the experiment without disturbance. The laser is switched on at $t = 2$ s. Within 0.3 second, the demanded melt pool width of 2.1 mm is realized. At this time, the laser power has reached a value of 980 W. In the next 8 seconds the laser power drops slightly to about 960 W because of the temperature increase of the substrate bar. The melt pool width remains at the demanded 2.1 mm. At $t = 10$ s., the width of the melt pool increases because the cladding speed is reduced to 0 mm/s. The controller acts robust and fast, showing only small fluctuations in melt pool width and laser power.

Figure 10.13 on the right shows the laser power and melt pool width of experiment 5 from Table 10.2. The cladding speed was suddenly increased from 13.33 to 16.66 mm/s. at $t = 5.5$ s. As soon as the cladding speed increases, the width of the melt tends to decrease but within half a second the laser power is adjusted. Although the cladding speed was increased by 25 %, the laser power increases only by 8% (960 to 1040 W). This is because the powder feed is not increased correspondingly. Since about half of the laser power is used to melt the powder, this contribution of the laser power need does not have to increase. Secondly, the energy losses by conduction reduce with increasing cladding speed.

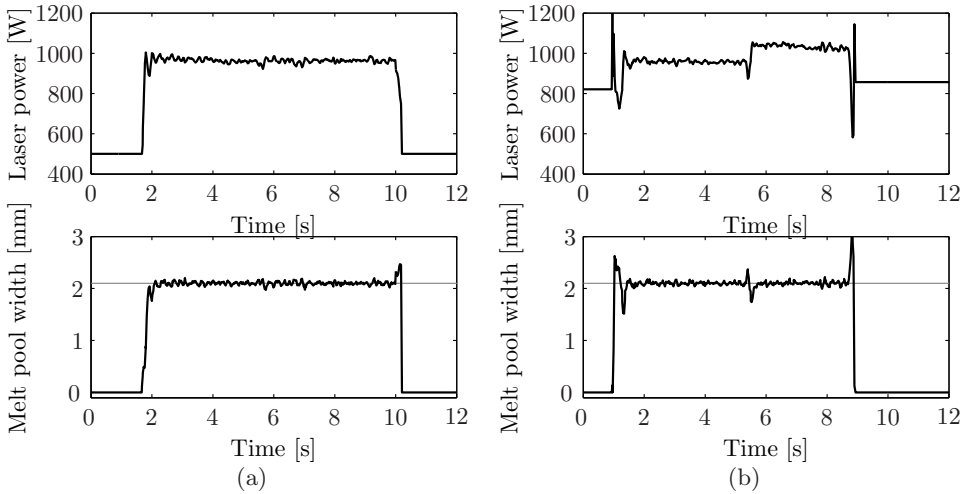


Figure 10.13: The laser power and melt pool width as function of the time for two cladding experiments. (a) constant cladding speed. (b) speed increase at $t = 5.5$ s.

10.5.5 Overlap cladding

In this section, the laser power changes during overlap cladding is discussed. A full surface layer was cladded on a bar. The process settings were similar to experiment 5. After laying one track, 4 overlap tracks and one end track were made. The shift between the tracks is 1.4 mm, resulting in an overlap ratio of 33 %. The first track was produced directly on the bar surface but after one revolution the cladding head starts to move along the bar axis, resulting in a spiral over the bar. At the start of the spiral the overlap is 100 % which reduces to 30 % after a full revolution. At the end, the linear movement was stopped and the overlap increases from 33 % to 100 %. The width of the melt pool might be influenced by such changes, absorptivity and conductivity. Figure 10.14 shows the response of laser power and melt pool width. After nine seconds the spiral movement starts. At this point, the heat conduction to the substrate reduces because of the 100 % overlap cladding and then increases gradually. During cladding of the successive 33 % overlap tracks, the required laser power (900 W) is below that of the first track (1000 W). At the end, the spiral stops causing an increasing overlap ratio. The laser power decreases correspondingly.

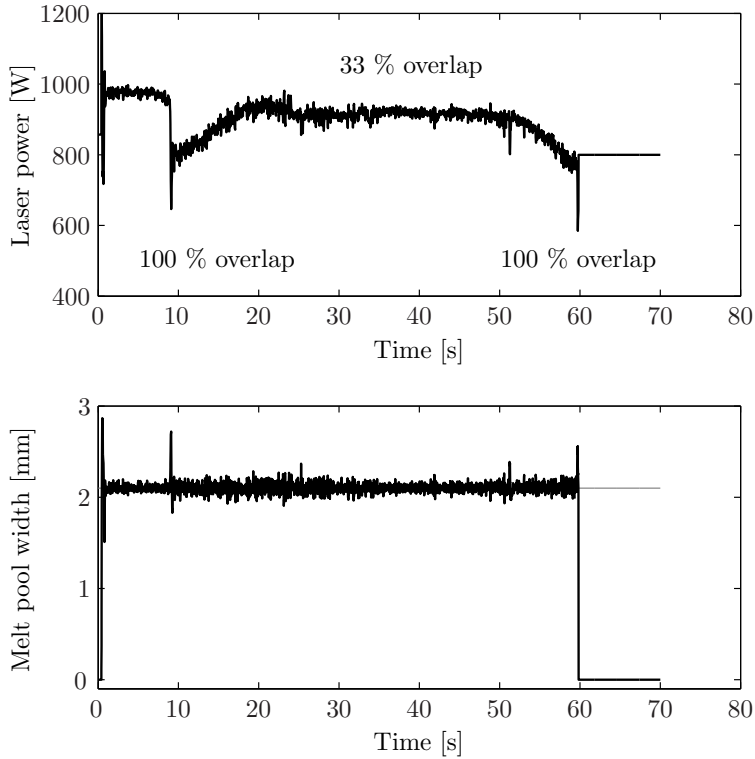


Figure 10.14: Laser power and melt pool width during overlap cladding.

10.5.6 Influence of the substrate temperature

As can be seen in Figure 10.14, the laser power drops slightly because of a small temperature increase of the substrate during cladding. To investigate the influence of the substrate temperature on the required laser power, two further experiments were performed; one in which the laser power is kept constant and one in which the melt pool width is kept constant. Both experiments were performed near the end of a bar. In a spiral using 33 % overlap, a layer is produced onto the end of a bar. The process settings were similar to the previous experiment. Figure 10.15 shows the laser power and melt pool width for both experiments.

At the beginning, the melt pool width in the uncontrolled experiment is less than 2.1 mm. At $t = 10$ s., the spiral starts. The uncontrolled laser power (900 W) results in an increased melt pool width which increases to 3.1 mm at the end of the cladding. In the controlled situation, the laser power

starts at about 1000 W. At $t = 10$ s. the laser power decreases to compensate for the overlap and lower heat losses. The melt pool width of 2.1 mm is maintained over the entire cladding. The laser power reduces considerably to 600 W at the end of the cladding process which is a reduction of 40 %.

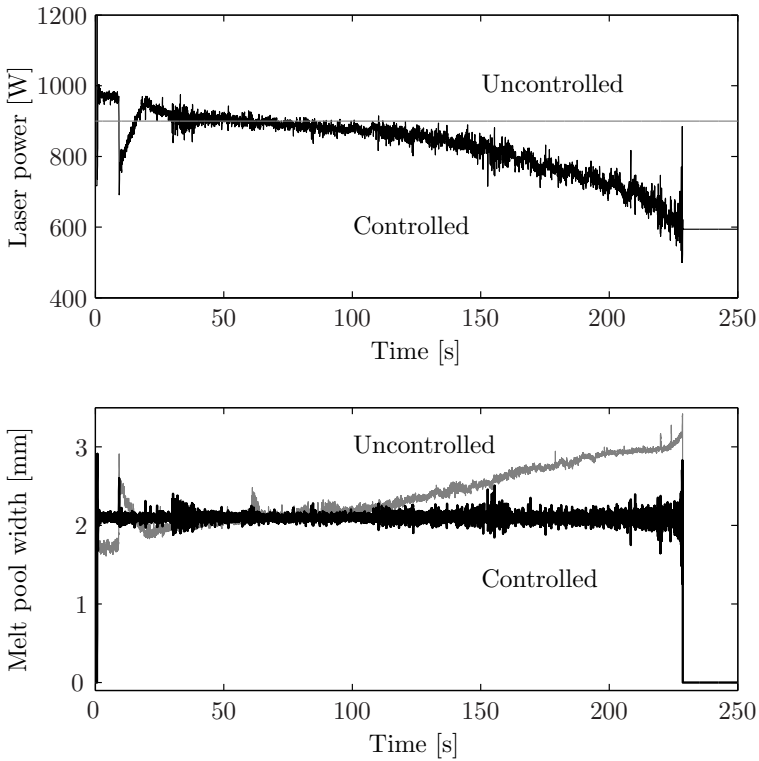


Figure 10.15: Laser power and melt pool width during overlap cladding at the end of a bar.

From both bars cross-sections were cut covering over the full length of the clad layer (40 mm). The samples were embedded, polished and etched using a 2 % Nital solution. Figure 10.16 show both layers. Over the first half of the layer, both samples show a comparable clad height, heat affected zone and no dilution. Further towards the end of the bar, the uncontrolled bar shows some limited dilution while the controlled bar remains at a minimal dilution. Figure 10.17 shows details from both bars, showing the difference between the two situations. The increased heat affected zone in the uncontrolled situation is clearly shown.

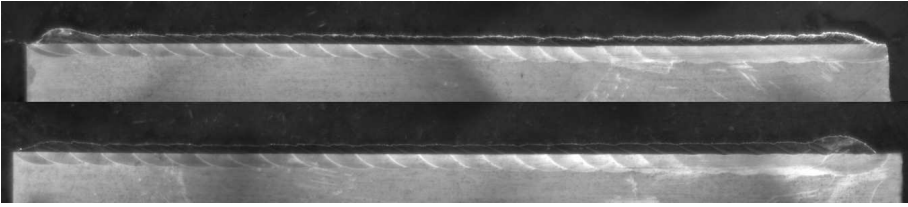


Figure 10.16: Micrographs of cross-sections of the two layers. Top: Controlled cladding (Constant melt pool width). Bottom: Uncontrolled cladding (constant laser power).

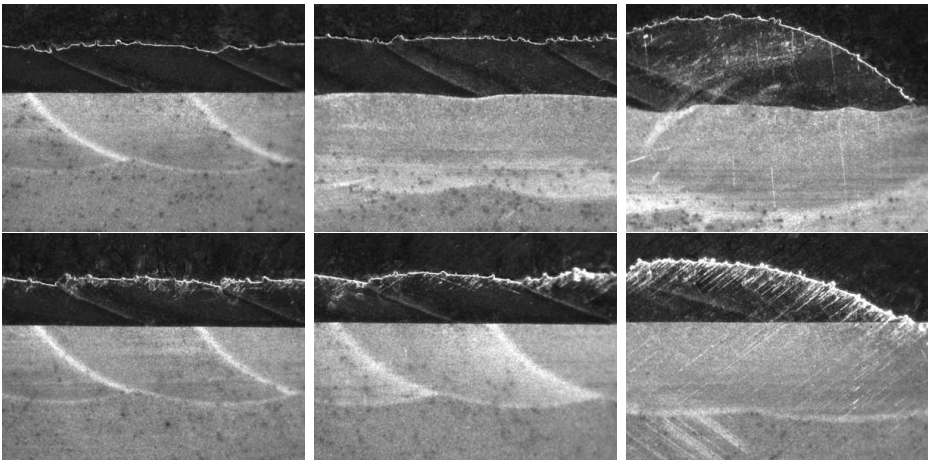


Figure 10.17: Details of the clad layers of Figure 10.16. Top: Uncontrolled, Bottom: Controlled. The photographs show the layers at the center, three quarter length and at the end.

10.5.7 Cladding of a pitch shaft of a windmill turbine.

Due to the high loads on the turbines of windmills, several part need periodic repair. One of the parts, which is often severely damaged is the pitch shafts. Figure 10.18 shows such a part, a pitch shaft with one of the bearing seats damaged. Over a length of about 200 mm this 150 mm diameter shaft has been repaired by laser cladding. The width of the melt pool was kept constant at 2.7 mm. The laser power for the first track was 1200 W reducing quickly to 850 and then gradually to 750 WW (Figure 10.20). During the last track cladding, the laser power falls to 700 W because of the 100 % overlap. Around $t = 300$ s, two jumps in the laser power are observed



Figure 10.18: Windmill pitch shaft.

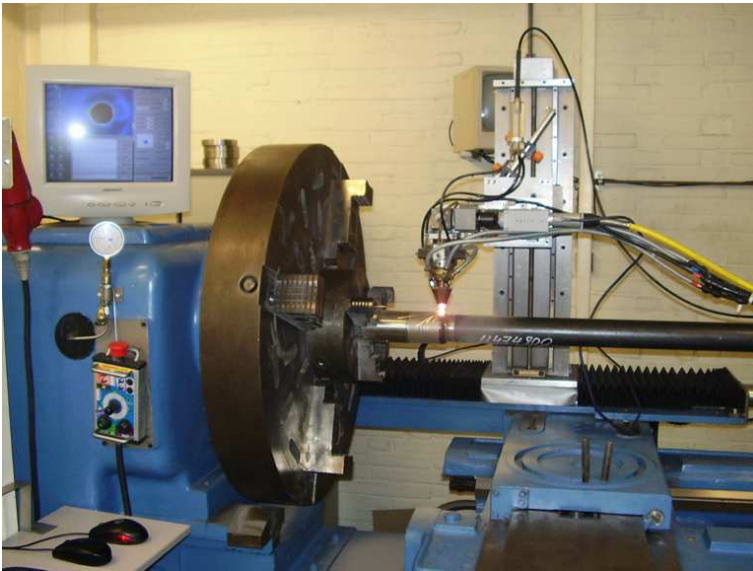


Figure 10.19: Controller in action.

where two single repair tracks have been placed before. Figure 10.21 shows the final surface after cladding with the two aforementioned places. Careful

inspection of the shaft has shown a constant, pore free quality of the clad layer over the entire surface.

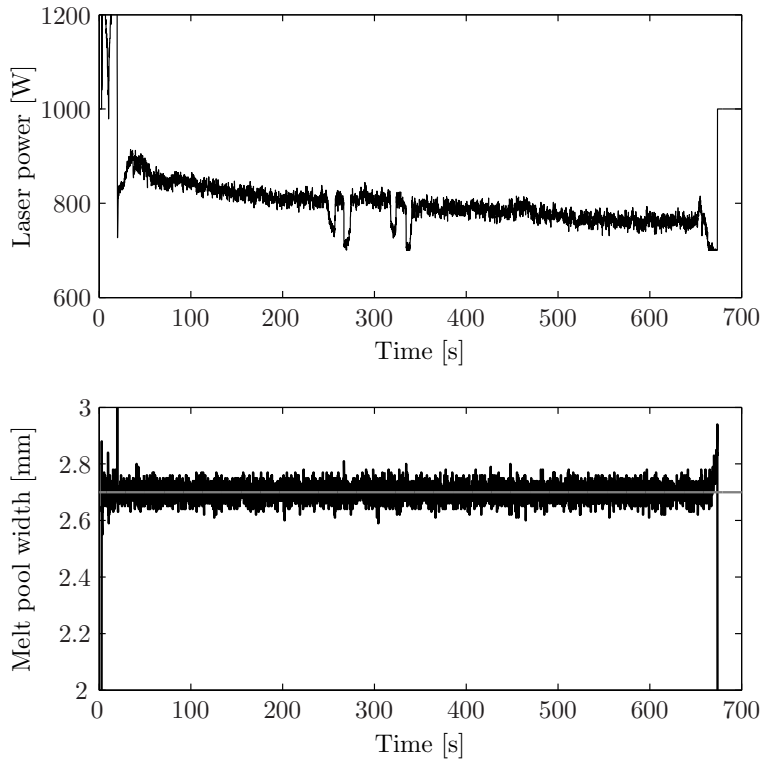


Figure 10.20: The laser power and melt pool width as function of the time during cladding of the pitch shaft.

The control system has proven to function robust and reliable in an industrial environment as demonstrated by this case. The system has enabled SG&S to further integrate the cladding technique in their business. It provides them of a quality assurance which could not be obtained without such a system.

10.6 Review and conclusions

The implementation of the process controller as developed in chapter 8 in an industrial environment has resulted in faster production and better quality. The controller software, however, has to be extended to meet the

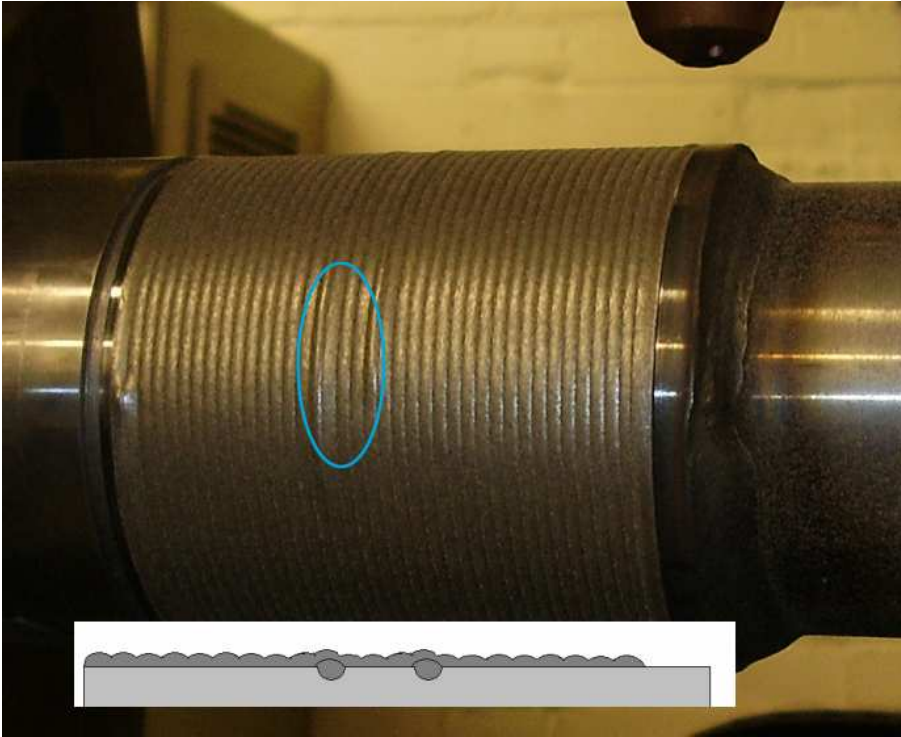


Figure 10.21: Cladded surface of the pitch shaft.

typical industrial requirements. For this purpose, a GUI was developed, allowing an operator to easily adjust necessary settings. The control loop is programmed in such a way that it functions independent of the rest of the cladding workstation.

Several experiments were performed to investigate how the controller behaves in the industrial environment of SG&S. The control system proved to be robust and reliable. The conclusions of this implementation are:

- The optical filter suppressed the laser radiation sufficiently, as clear images of the melt pool are observed.
- The coaxial powder supply does not disturb the observability of the melt pool.
- A progressive relation between melt pool width and laser power exists.

- The controller effectively adjusts the laser power to compensate for various disturbances.
- The controller is used successfully in several cladding products at SG&S.
- The dilution is significantly reduced using this controller.
- The use of this controller enables SG&S to repair damaged parts with lower heat input and consequently minimal deformations.
- The controller leads to an increased quality control and has enabled SG&S to repair more critical products at lower costs.

Chapter 11

Residual stresses

11.1 Introduction

The laser cladding technique is known for its advantages over other cladding techniques; a low dilution and limited heat effects on the base material, less distortion and suitability for process automation. However, due to the local heat input, the high temperature gradients may result in high tensile residual stresses [36]. As a consequence of the high stresses in the layers cracks may occur. Often such cracks propagate perpendicular to the cladding direction, indicating that the stresses are highest along the cladding direction. Stresses can be influenced by control of the cladding process. In this chapter some empirical relations between stresses and the process settings are presented. The experimental procedure for the determination of the stresses is based on deflection measurements. This method is relatively fast compared to other analysis methods. To validate the calculated stresses using deflection measurements, additional experiments using XRD [44] have been performed.

11.2 Experimental setup and procedure

The experimental setup is shown in Figure 11.1. Clad layers were produced onto square ($12 \times 12 \times 180$ mm) bars which were supported at the two ends. At the center of the bar at the bottom side, a Heidenhain linear displacement sensor measured the deflection during and after cladding. Over the entire length of the bar, an overlapping five-track clad layer is produced. The cladding experiments were performed in a controlled way by the deve-

loped process controller. The powder feed rate was related to the cladding speed to give a constant clad height. The laser power was controlled to get a constant (2.5 mm) melt pool width at all speeds using a 3 mm diameter laser spot. The powder was fed through a leading nozzle inclined at 40° to the laser beam. Due to heating of the top side of the bar during the

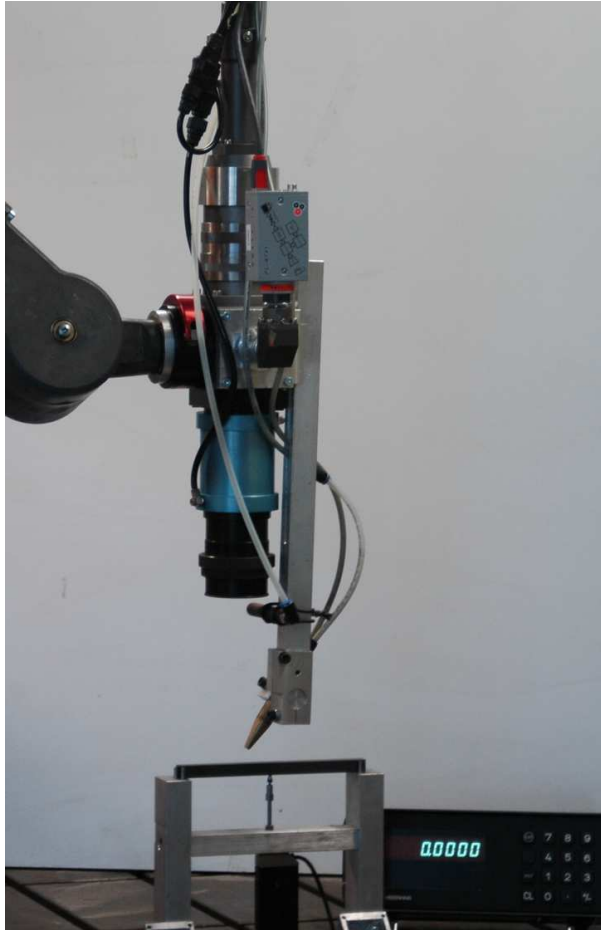


Figure 11.1: Experimental setup.

cladding process, the bar deforms, resulting in an upwards displacement of the center position. This bending reaches its maximum when about 70% of a track is laid. On each bar five overlapping tracks were produced. After cooling down, the deflection of the bar is measured. This deflection is due

to the effects of residual stresses in the bar and clad layer as well as the plastic deformation caused by bending during cladding.

Figure 11.2 shows the bar and clad layer and the used coordinate system. In the clad layer a three dimensional stress field will be present. Stresses in the cladding (x) direction will be high while the stresses transverse to the cladding direction (y) are expected to be much smaller. The stresses in the x -direction are calculated from the springback of the bar in the z -direction after removal of the clad layer. The stress levels will generally vary with the depth from the top of the clad layer. To investigate this, these layers are stepwise removed. After each step, the deflection of the bar is measured by an accurate three point measurement technique.

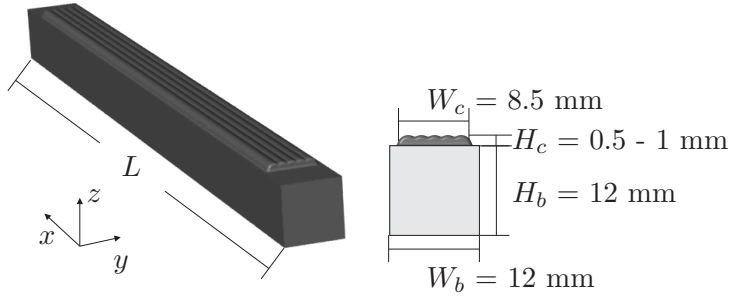


Figure 11.2: A schematic representation of the bar and clad layer and typical dimensions.

A constant moment M over the length of the bar is supposed to cause the deflection in the z -direction. The backspring in the z -direction at $\frac{1}{2}L$ due to a bending moment M is:

$$D = \frac{M \cdot (\frac{1}{2} L)^2}{2 E I}, \quad (11.1)$$

where I is the moment of inertia of the cross-section (bar + clad layer) and E is the Young's modulus. The moment M can also be expressed in terms of the stresses in the removed part of the clad layer.

$$M = R \cdot A \cdot \sigma_{av}, \quad (11.2)$$

where R is the distance from the neutral axis to the center of the removed

layer, A and σ_{av} are the cross-sectional area and the average longitudinal stress of the removed layer respectively.

11.3 Relations between process settings and residual stresses

The goal of the performed experiments was to investigate the influence of the cladding speed on the residual stresses. Clad layers of two different cladding materials (Stellite 12 and Inconel 625) were produced on a *S235JR* steel substrate. The cladding speed was varied from 3 to 20 mm/s. The laser power was adjusted in real-time to maintain a melt pool width of 2.5 mm resulting in minimal dilution. The powder feed rate was coupled to the cladding speed to get an area of 2.5 mm² for each track. Nitrogen was used as shielding gas. The Young's moduli for the different materials are taken from literature as 204 GPa, 224 GPa and 226 GPa for the steel substrate, the Stellite 12 and the Inconel 625 respectively. The total width of the clad layers was about 8.5 mm, and the height varied between 0.5 and 1.0 mm depending on the cladding speed despite the fact that the powder feed was increased proportionally.

11.3.1 Plastic and elastic deformations

The total deflection of the bar is due to the plastic deformation caused during cladding and the elastic deformation due to residual stresses present in the clad layer. The magnitude of the deflection depends on the number of tracks, i.e. the cross-sectional clad area. To investigate this aspect, a view steel bars were cladded with Stellite 12 at a cladding speed of 15 mm/s with 1 to 5 tracks. The deflections were measured at room temperature after cladding and after removing the clad layers. The plastic deformation is obtained from the remaining deflection after removal of the clad layers. The elastic part is the difference before and after removal of the layer. The results are shown in Figure 11.3. With the increasing number of tracks the magnitude of the total deflection increases. The elastic deflection due to residual stresses varies almost linearly with the number of tracks and therefore with the total cross-sectional area of the clad layer.

Figure 11.4 indicates the variation of the residual stresses with the depth from the clad layer surface, obtained after successive layer removal of the three samples with 5-track layers. Also these results indicate a good re-

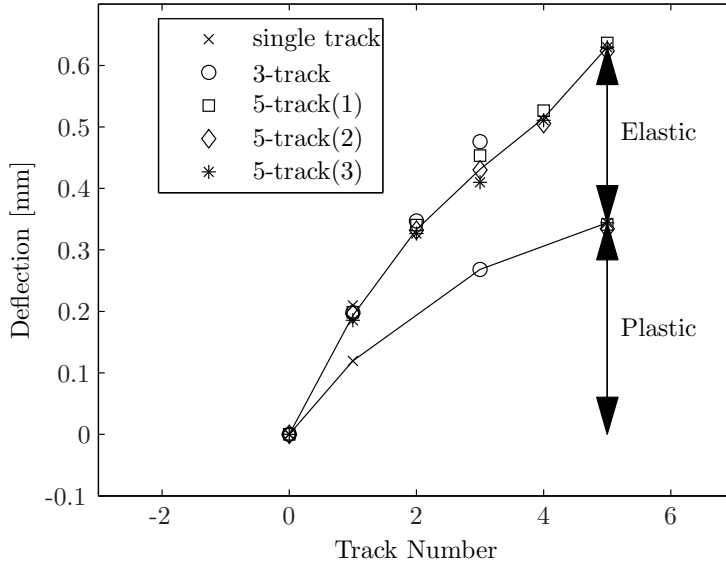


Figure 11.3: Deflection of the bars due to plastic and elastic deformation.

producibility. The tensile stresses have a minimum near the surface and a maximum close to the clad-substrate interface.

11.3.2 Laser power

The laser power was real-time controlled to maintain a constant melt pool width. Figure 11.5 shows that the specific energy as function of the speed for both materials. Both the specific energy for the first track and the average specific energy for the successive tracks are shown. The trends are similar for both cladding materials. The specific energy reduces with increasing cladding speed (by a factor of about 2 when the cladding speed is increased by a factor of about 5).

11.3.3 Deflection

With increasing speed, the thermal cycle of the material will change. This influences the residual stresses as well as the deformation. The relation between the speed and the elastic deflection due to the removal of the clad layer is expressed in Figure 11.6. The deflection caused by the Stellite

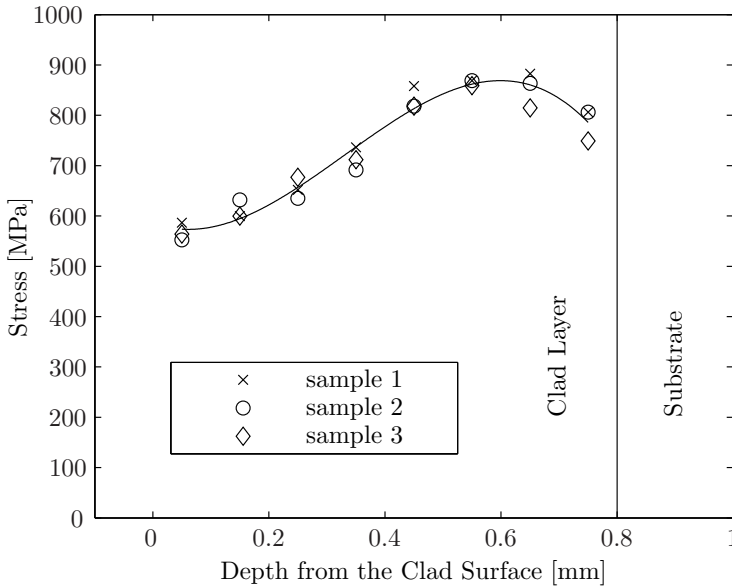


Figure 11.4: Stress as function of the depth from the clad surface obtained by stepwise removal of the layer. (Stellite 12, 15 mm/s cladding speed)

12 layers increases with the cladding speed while Inconel 625 deflections increase with cladding speeds up to about 10 mm/s and then stabilize.

11.3.4 Stress distribution in the clad layer

Figure 11.7 shows the stress in the Stellite 12 layers as function of the depth from the surface as obtained by the deflections. The clad-substrate interface positions are indicated as vertical lines. Also include the surface stresses. these stresses are obtained by XRD measurements as described in the next section.

The maximum stress is observed at the middle of the thickness for low cladding speeds. With increasing speed, the maxima shift towards the clad-substrate interface and increase at all depths.

The stress distribution in the Inconel 625 layers does not show a clear trend as was seen with Stellite 12 clad layers (See Figure 11.8). However, some of the observations are similar. The stress distributions show maxima at some depth from the surface for all cladding speeds except for the highest speed (20 mm/s). With increasing cladding speed, the maximum stress

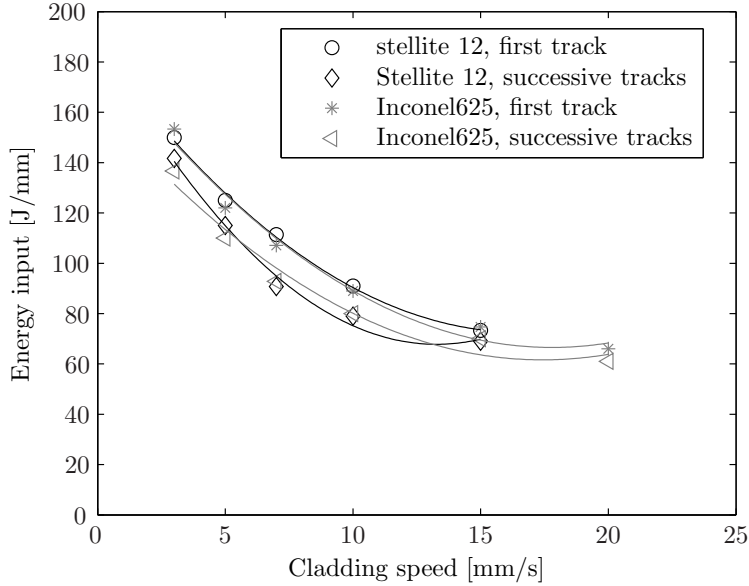


Figure 11.5: Average energy input per unit length as function of the cladding speed.

location shifts towards the clad-substrate interface. In general, the stresses in Inconel 625 layers are lower than those in Stellite 12 layers. Inconel 625 has a lower yield strength and higher ductility than Stellite 12, which might be a reason for the observed differences in the residual stresses.

11.3.5 Stresses at the surface

Because the deflection technique can not be applied to determine the stresses on the surface, the surface stresses were determined by the non-destructive XRD technique [44, 45, 46].

Residual stresses cause changes in the lattice spacing (a_0) resulting in a shift in diffraction peak positions. By measuring the diffraction peak positions in stressed and stress free conditions of the material, the strains can be obtained. From the measured strains, the stresses are obtained by the appropriate elastic constants (E , ν). The residual stress measurements have been carried out using a Rigaku X-ray stress analyser (MSF-2M) with a Ω - goniometer according to $\sin^2\psi$ method [44, 45, 46]. The stresses acting along the cladding and transverse directions have been obtained from

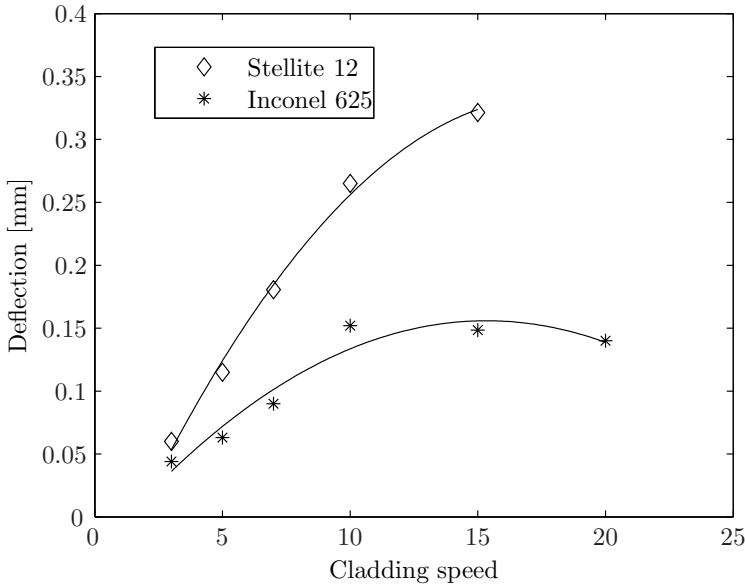


Figure 11.6: Deflection due to elastic deformation of the bar after removal of the layer.

strains measured along six different ψ angles. The measurements were done at the center of the clad tracks on an area of about $7 \times 3 \text{ mm}^2$. The sample surface was as cladded without any mechanical or chemical preparations. Vanadium $K\alpha$ radiation was used to measure the strains in $\{220\}$ crystallographic planes of Stellite 12 (Cobalt phase, FCC structure) and Inconel 625 (Nickel phase, FCC structure). To minimize the effects of the cast structure of the clad on the diffraction profiles, the goniometer was oscillated by $\pm 3^\circ$. The diffraction profiles were corrected for Lorentz Polarization and Absorption (LPA) and background. The corrected profiles were treated for $K\alpha 1/K\alpha 2$ overlap and the $K\alpha 1$ profiles were analyzed using the least squares parabola fitting method to determine the peak positions. From the peak position, the d-spacing was calculated using Bragg's law. A least squares linear fit of the measured $\varepsilon_{\varphi, \psi}$ versus $\sin^2 \psi$ was made and from the slope of this line, the stress σ_φ was computed using the X-ray elastic constant, $\frac{1}{2}S_2 = \frac{(1+\nu)}{E}$.

The surface strains acting in the longitudinal (ε_L) and the transverse (ε_T) directions were measured using the XRD technique. Figure 11.9 shows the strains in case of Stellite 12 as function of the cladding speed. The strains

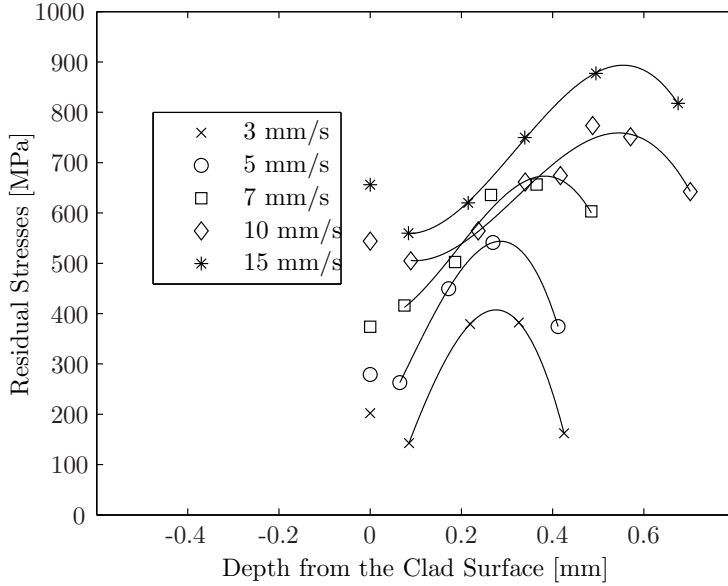


Figure 11.7: Stresses in the Stellite 12 clad layers as function of depth and cladding speed.

acting along the transverse direction (ϵ_T) are significantly lower than the longitudinal strains (ϵ_L). Similarly in Figure 11.10 the surface strains on Inconel 625 clad layers are compared showing that in this case the transverse strains (ϵ_T) are significant.

From the strains, the longitudinal and transverse surface stresses have been determined. The surface stresses as function of the cladding speed are presented in the Figures 11.11 and 11.12 for Stellite 12 and Inconel 625 respectively. At low cladding speed, the Inconel 625 layers show compressive stresses in the transverse direction. At high cladding speed the transverse stresses are tensile and are larger in magnitude compared to the longitudinal stresses. In case of Stellite 12, both the longitudinal and transverse stresses at the surface are tensile and increase with increasing cladding speed.

11.3.6 Stress as function of cladding speed

By using the total deflection of the bar before and after removing the entire clad layer, the average longitudinal stress in the cross-section of the clad

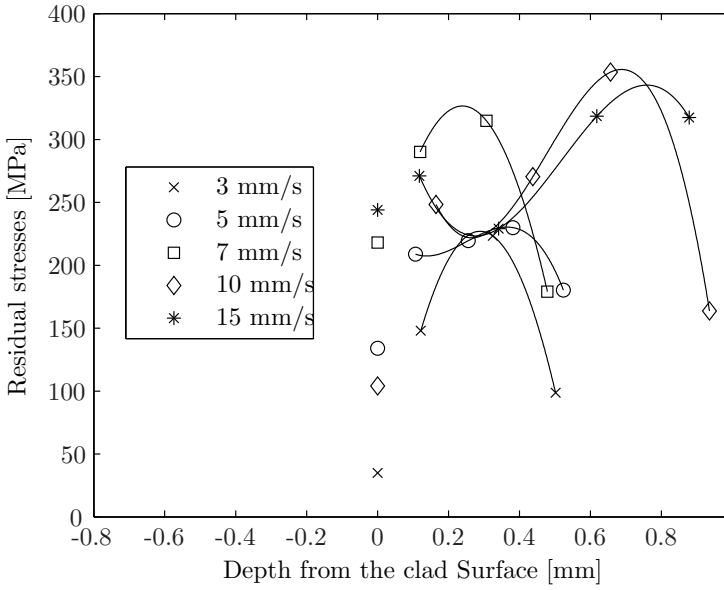


Figure 11.8: Stress in the Inconel 625 clad layers as function of depth and cladding speed.

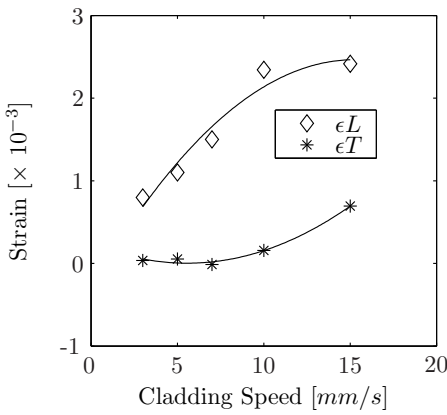


Figure 11.9: Strains at the surface for the Stellite 12 layers.

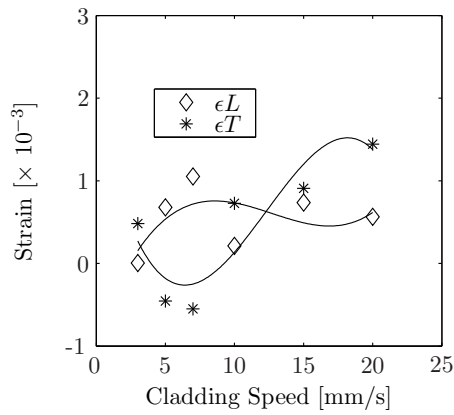


Figure 11.10: Strains at the surface for the Inconel 625 layers.

layers can be determined. These average stresses are graphically expressed in Figure 11.13 and figure 11.14 for Stellite 12 and Inconel 625 respectively. Also the stresses found at typical locations within the layers are indicated

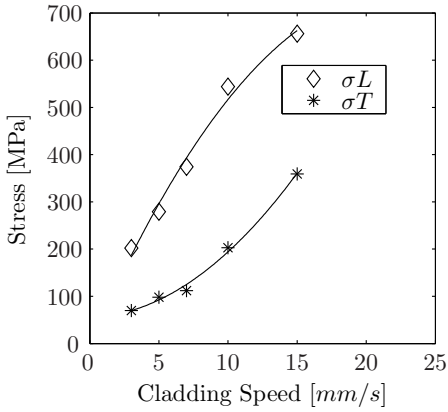


Figure 11.11: Stresses at the surface for the Stellite 12 layers.

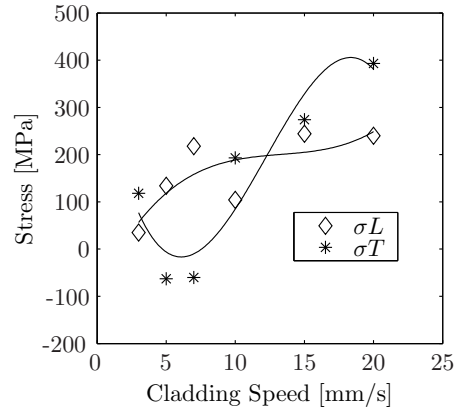


Figure 11.12: Stresses at the surface for the Inconel 625 layers.

for comparison. The stresses observed in the Stellite 12 layers are found to increase significantly with the cladding speed. With Inconel 625 layers, the increase in stresses with cladding speed is less pronounced.

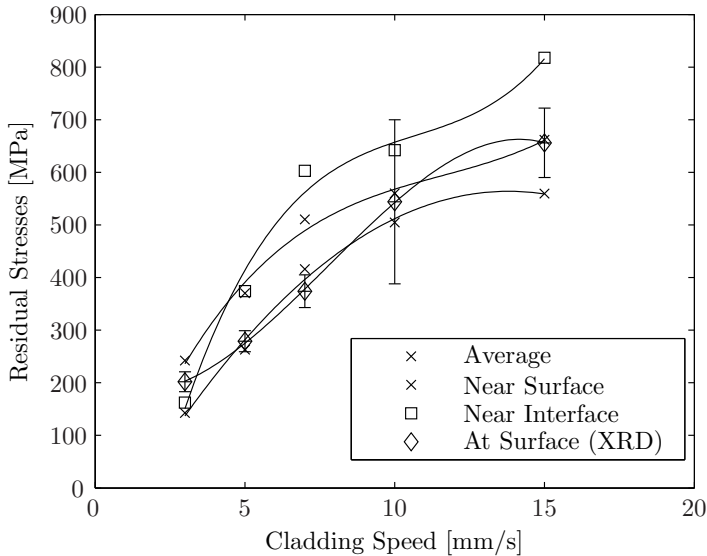


Figure 11.13: Average stresses in the Stellite 12 clad layers as function of the cladding speed.

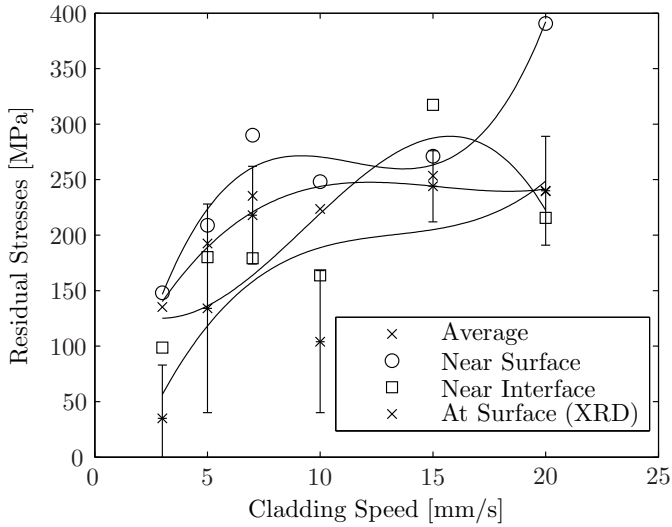


Figure 11.14: Average stresses in the Inconel 625 clad layers as function of the cladding speed.

11.4 Review and conclusions

The residual stresses developed during cladding are investigated using the deflection of a steel substrate bar sample. The deflection of the bar corresponds linearly with the longitudinal stresses in the clad layer, assuming that transverse stresses can be neglected. The main conclusions are:

- The stresses in the Stellite 12 layers are tensile and increase with the cladding speed.
- The stresses in the Stellite 12 layers vary with the depth from the surface and show a maximum within the clad layer. The location of such maxima shifts toward the clad-substrate interface with increasing cladding speed.
- Stresses in the Inconel 625 layers are considerable lower than those in the Stellite 12 layers.
- The near surface and at surface stresses calculated from the deflection and the XRD surface stresses are comparable for Stellite 12.
- With Inconel 625, the near surface stresses calculated from the deflection measurements are significantly higher than the stresses obtained

with X-rays. This difference is due to the influence of a significant transverse stress present in the Inconel 625 layers.

- The elastic deflection of the bars, caused by residual stresses is about half of the total deflection, making it possible to estimate the stresses by means of the bar deflection without removing the layer.

Chapter 12

Conclusions

In order for laser cladding to find a wider industrial application and increased market share, the cladding process should be easily controllable and the clad characteristics and quality should be uniform, consistent and reliable.

This research was aimed at achieving the above by accomplishing the following;

- Obtaining a better fundamental understanding of the laser cladding process.
- The development of a dedicated optical system for the laser beam delivery.
- The development of a Finite Element Method (FEM) model of the laser cladding process.
- Experimental and simulation analyses of the influence of the main process settings on the clad characteristics.
- The development of a camera based feedback control system suited for industrial use.
- The evaluation of the influence of the main process parameters on the development of residual stresses.

The major conclusions based on the results of this research are summarized below;

The main process variables like laser power, its distribution, beam spot size, cladding speed, substrate temperature and powder feed rate, influence significantly the clad track characteristics. The melt pool size, dilution and clad track geometry increase with increasing laser power or initial substrate temperature. Increasing the cladding speed has a decreasing effect on all these characteristics. The laser beam intensity profile (Top-hat, Gaussian or ring shaped) influence the clad shape, in particular the burn-in shape. However, the presence of melt recirculation flow patterns may have a larger influence. These flow patterns appear to be driven more by the momentum transfer from the powder jet than by Marangoni forces alone. A Gaussian intensity distribution is least preferable as it causes either a burn-in at the center of the clad track, or insufficient heating at the sides of the track. Clad tracks produced by the ring distribution show a double peaked burn-in. The burn-in depth is minimal and most constant along the transverse direction when a laser beam with a top-hat distribution is used (Chapter 5).

The powder feed nozzle can be either inclined to the laser beam axis or coaxial. The developed online feed back controlled laser system is able to perform equally well with both type of nozzles and powder feeding (see Chapters 9 and 10).

Real time monitoring of the melt pool dimensions, the width in particular, offers the best online feed back control strategy. Using a commercial CMOS camera and an optical low pass filter, images of the melt pool area can be captured. The developed software program is able to calculate the dimensions of the melt pool. The procedure involves the determination of the threshold value that corresponds to the melting temperature of the clad material. This value can be determined by measuring the actual width of a track and depends on the powder material used. The system runs at 30 - 300 Hz and is capable to obtain the dimensions of the melt pool in real time (Chapter 5).

The developed FEM model of the laser cladding process incorporates the effect of the powder jet on the heat balance as well as it's influence on the laser beam radiation. Using a geometrical transformation, the temperature solution is solved in the computational domain. With this solution, the real temperatures are obtained using the corresponding transformations. This approach solves the clad geometry and temperature field

simultaneously (Chapter 6).

The FEM model predictions are verified against experimental results. From the analysis of the cross-sections, the influences of the process parameters on the clad characteristics were determined. The width of the clad track is highly determined by the laser power, increasing rapidly at low laser powers and saturating at a value close to the laser beam diameter at high laser powers. The width of the melt pool is found to be dominantly controlled by the laser power. The dilution level is found to have a clear correlation with the melt pool width. This relation is found to be almost independent of the cladding speed and the specific powder feed rate. Based on these results, a control strategy to control the dilution can be developed. The temperature gradients are found to decrease with laser power, and increase with cladding speed. Since residual stresses are highly determined by the cooling rates, the stresses in clad tracks are expected to increase with cladding speed as well (Chapter 7).

A feed back control strategy for the laser cladding process has been developed which adjusts the laser power such that the width of the melt pool is kept at a user defined reference value. The control loop uses a CMOS camera and software algorithms to obtain the width of the melt pool as discussed in chapter 6. Using a discrete control filter, the required laser power to meet the reference melt pool width is determined. This signal is sent to the laser controller using an IO-card. Robustness of the system is guaranteed by designing the phase of the open loop system in such a way that the phase of this system is always larger than -90° . The control filter gain is designed such that the closed loop bandwidth of the cladding process is in the order of 5 Hz. As a result, the closed loop system will effectively compensate for disturbances (such as heat sink changes and speed changes) within a fraction of a second (Chapter 8).

To evaluate the performance of the developed control system, several experiments were performed, investigating the influence of the powder material, changes in the geometry and the heat accumulation (Chapter 9). The results show that;

- The melt pool width is successfully controlled by adjusting the laser power by the controller.

- The optimal melt pool width is determined by determining the crossing point of two asymptotes as indicated in Figure 7.16 on page 94 and is about 90 % of the spot diameter.
- The controller performs well independent of the powder material used.
- The controller successfully adjusts the laser power to compensate for changes in the heat conduction
- Changes in the substrate geometry and temperature make it necessary to adjust the laser power.
- A constant laser power leads to an excessive dilution and reduced hardness of the clad layer due to heat accumulation.
- With the controller, the laser power is adjusted for such heat accumulation, resulting in a reduction of the power by 50 %. Due to this reduction, the dilution is kept constant over the entire clad layer. The hardness of the layer remains constant as well.

The implementation of the process controller in an industrial environment has resulted in faster production and better quality. Several experiments were performed to investigate how the controller behaves in the industrial environment of SG&S, Rotterdam. The control system proved to be robust and reliable. With the application of this controller, the dilution is significantly reduced; deformations were minimal while repairing damaged parts and an increased clad quality is obtained (Chapter 11).

The residual stresses developed during cladding are investigated using the deflection of a steel substrate bar sample. The deflection of the bar corresponds linearly with the longitudinal stresses in the clad layer, assuming that transverse stresses can be neglected. The main conclusions are:

- The stresses in the Stellite 12 layers are tensile and increase with the cladding speed.
- The stresses in the Stellite 12 layers vary with the depth from the surface and show a maximum within the clad layer. The location of such maxima shifts toward the clad-substrate interface with increasing cladding speed.

- Stresses in the Inconel 625 layers are considerable lower than those in the Stellite 12 layers.
- The near surface and at surface stresses calculated from the deflection and the XRD surface stresses are comparable for Stellite 12.
- With Inconel 625, the near surface stresses calculated from the deflection measurements are significantly higher than the stresses obtained with X-rays. This is due to a significant transverse stress present in the Inconel 625 layers.

Appendix A

Ray pattern of the variable focus optics

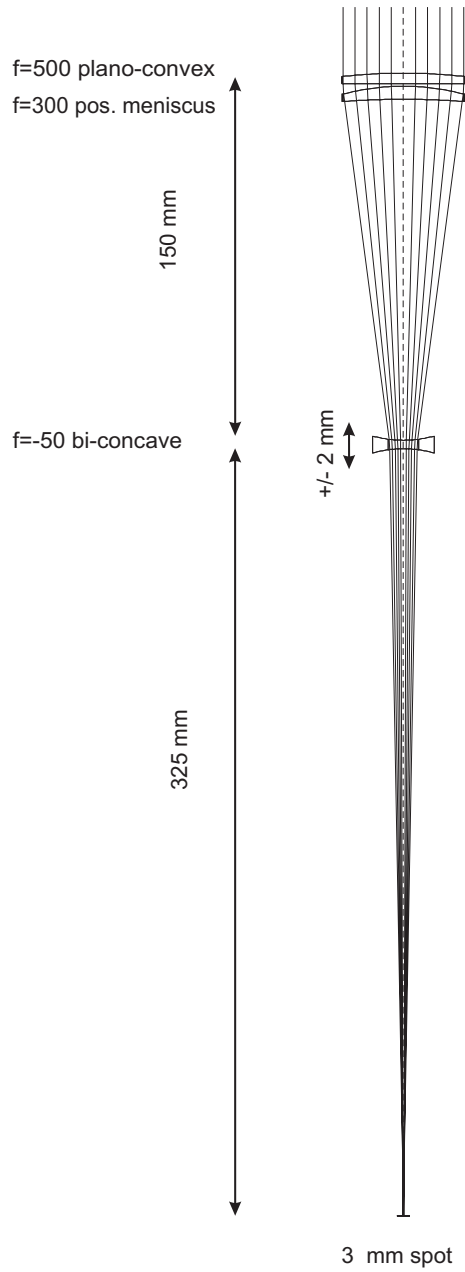


Figure A.1: Ray pattern of the variable focus system.

Appendix B

Powder jet speed

The following matlab script was used to determine the velocity field of the powder jet after leaving the nozzle as described in section 3.4.

```
delta = 5; % subwindow size
image = powder_image(:,:,1);

for k = 2:1000 % frame number
    image_previous = image;
    image          = powder_image(:,:,k);

    for y = 3:size(image,2)-2; % y-position in image
        for x = 3:size(image,1)-2; %x-position in image
            % obtain the subimage around [x,y] of the previous
            % image
            sub_image_previous = image_previous(y-delta+1...
                :y+delta,x-delta+1:x+delta);

            % remove the mean value of the image
            sub_image_previous = detrend(sub_image_previous,...
                'constant');

            % obtain the subimage around [x,y] of the current
            % image
            sub_image          = image(y-delta+1:y+delta,...
                x-delta+1:x+delta);
```

```

% remove the mean value of the image
sub_image          = detrend(sub_image,...
'constant');

% compute the correlation matrix between previous
% and current image
cor_matrix=xcorr2(sub_image,sub_image_previous);

% find the shifts in x and y direction that give
% the highest correlation
[dy dx]= find(cor_matrix==max(cor_matrix(:)));

% cor_matrix(2*delta,2*delta) (center of matrix)
% corresponds to no shift
dx =dx-2*delta;
dy =dy-2*delta;

% take the mean of dx and dy since no guaranty for
% one maximum
dx=mean(dx);
dy=mean(dy);

% add shifts to shift of previous image compare
shiftsx(y,x)=speedx(y,x)+mx;
shiftsy(y,x)=speedy(y,x)+my;
    end
end
end

% shifts are now total over 999 image, so divide
% by number of images
shiftsx=shiftsx/(k-1); shiftsy=shiftsy/(k-1);

% convert pixel shifts to meters
% 30 [pixels] = 2.4 [mm] -> 1 [pixel] = .08 [mm]
% = 80e-6 [m]
shiftsx=shiftsx*80e-6; shiftsy=shiftsy*80e-6;

% convert to speeds by dividing by the time

```

```
% between successive images
% framerate = 10,000 Hz -> dt = 1e-4
speedx = shiftsx/dt; speedy = shiftsy/dt;

% absolute speed
speed_abs = sqrt(speedx.^2+speedy.^2);
```


Appendix C

Laser and Powder interactions

The heat input for the laser cladding process can be split-up into two parts. At the surface the laser radiation is partially absorbed. The laser beam passes through the powder jet which arrives at the melt pool at an elevated temperature. This interaction of the laser beam with the powder jet is taken into account in the model. Also energy fluxes associated with material flow is taken into account. This results in the following boundary condition:

$$k \frac{\partial T}{\partial n} + q_{mass} = q_{laser} + q_{powder}. \quad (\text{C.1})$$

Here, $q_{laser}(\vec{\mathbf{x}})$ is the heat flux associated with the laser radiation and $q_{powder}(\vec{\mathbf{x}})$ the heat flux associated with the pre-heated powder. The convective heat flux $q_{mass}(\vec{\mathbf{x}})$ at the left side of the equation can be expressed as:

$$q_{mass}(\vec{\mathbf{x}}) = -\vec{\mathbf{v}} \cdot \vec{\mathbf{n}} \int_{T_0}^{T(\vec{\mathbf{x}})} \rho c_p dT. \quad (\text{C.2})$$

with $\vec{\mathbf{v}}$ the speed of the material, $\vec{\mathbf{n}}$ the outward normal vector of the surface and $\int_{T_0}^{T(\vec{\mathbf{x}})} \rho c_p dT$ the heat of the material at elevated temperature $T(\vec{\mathbf{x}})$.

Laser and powder distribution and orientation

The laser intensity distribution depends on the used laser source as well as the optical system. The distribution in the model is assumed to be independent of its main axis i.e.:

$$I_{0,laser}(\mathbf{P}_L) = I_{0,laser}(Px_L, Py_L) \quad (C.3)$$

Here, the z_L -axis is parallel to the laser beam direction, and the x_L - and y_L -axis will be defined later. Analogue to the laser intensity distribution, the powder flux distribution is assumed to be independent of its main axis as well i.e.:

$$\Phi(\mathbf{P}_\varphi) = \Phi(Px_\varphi, Py_\varphi) \quad (C.4)$$

Here, the z_φ -axis is parallel to the powder jet direction, and the x_φ - and y_φ -axes will be defined later. The orientation and location of the powder jet and the heat source can be varied, and are independent of each other. A graphical representation of the powder jet and the heat source is given in Figure C. A point in space $\mathbf{P} = [Px, Py, Pz]$ can be expressed in global,

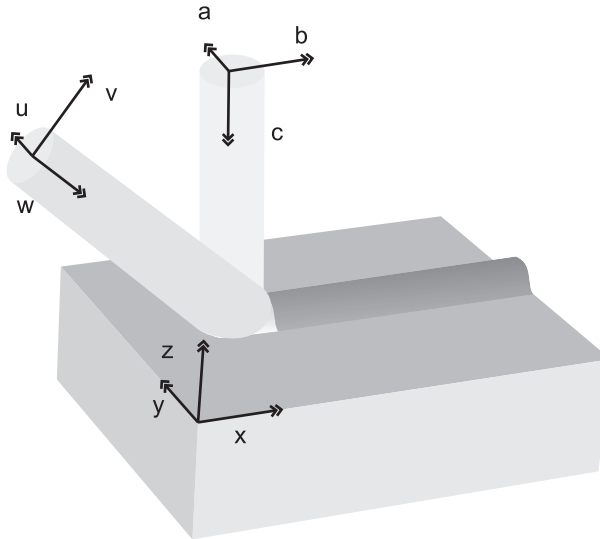


Figure C.1: laser beam and powder orientations.

laser or powder jet coordinates:

$$\begin{aligned} \mathbf{P}_g &= \begin{bmatrix} Px_g \\ Py_g \\ Pz_g \end{bmatrix}, & \mathbf{P}_L &= \begin{bmatrix} Px_L \\ Py_L \\ Pz_L \end{bmatrix}, & \mathbf{P}_\varphi &= \begin{bmatrix} Px_\varphi \\ Py_\varphi \\ Pz_\varphi \end{bmatrix}, \\ \mathbf{P}_g &= \mathbf{G}_L \mathbf{P}_L + \mathbf{O}_L, & \mathbf{G}_L &= [\mathbf{e}_L^1, \mathbf{e}_L^2, \mathbf{e}_L^3] \\ &= \mathbf{G}_\varphi \mathbf{P}_\varphi + \mathbf{O}_\varphi, & \mathbf{G}_\varphi &= [\mathbf{e}_\varphi^1, \mathbf{e}_\varphi^2, \mathbf{e}_\varphi^3] \end{aligned} \quad (\text{C.5})$$

where \mathbf{e}_L^i and \mathbf{e}_φ^i are the base vectors. \mathbf{O}_L and \mathbf{O}_φ are the origins of the laser beam and powder jet expressed in global coordinates. The z-axis of the laser beam and powder jet are chosen by the user:

$$\mathbf{e}_L^3 = \begin{bmatrix} e_L^3(1) \\ e_L^3(2) \\ e_L^3(3) \end{bmatrix}, \quad \|\mathbf{e}_L^3\| = 1, \quad \mathbf{e}_\varphi^3 = \begin{bmatrix} e_\varphi^3(1) \\ e_\varphi^3(2) \\ e_\varphi^3(3) \end{bmatrix}, \quad \|\mathbf{e}_\varphi^3\| = 1 \quad (\text{C.6})$$

The x-axes of the laser power distribution and the powder mass distribution are defined as:

$$\mathbf{e}_L^1 = \mathbf{e}_\varphi^1 = \frac{\mathbf{A}}{\|\mathbf{A}\|}, \quad \mathbf{A} = \mathbf{e}_\varphi^3 \times \mathbf{e}_L^3 \quad (\text{C.7})$$

This means that the x-axes are parallel and are perpendicular to a plane defined by the two z-axes. The y-axes of the laser power and powder distribution are defined as:

$$\begin{aligned} \mathbf{e}_L^2 &= \frac{\mathbf{B}}{\|\mathbf{B}\|} & \mathbf{B} &= \mathbf{e}_L^3 \times \mathbf{e}_L^1 \\ \mathbf{e}_\varphi^2 &= \frac{\mathbf{B}}{\|\mathbf{B}\|} & \mathbf{B} &= \mathbf{e}_\varphi^3 \times \mathbf{e}_\varphi^1 \end{aligned} \quad (\text{C.8})$$

Note that the matrices G_L and G_φ are unitary, i.e. $G_L^{-1} = G_L^T$ and $G_\varphi^{-1} = G_\varphi^T$.

Laser power attenuation

The laser light intensity at an arbitrary point in space \mathbf{P}_g is attenuated by the powder jet it has passed through. The powder mass M inside a small volume ΔV is determined by the powder flux intensity and the powder speed v_p :

$$M(\mathbf{P}_g) = \Phi(\mathbf{e}_\varphi^1 \cdot [\mathbf{P}_g - \mathbf{O}_\varphi], \mathbf{e}_\varphi^2 \cdot [\mathbf{P}_g - \mathbf{O}_\varphi]) \Delta V \frac{1}{v_p} \quad (\text{C.9})$$

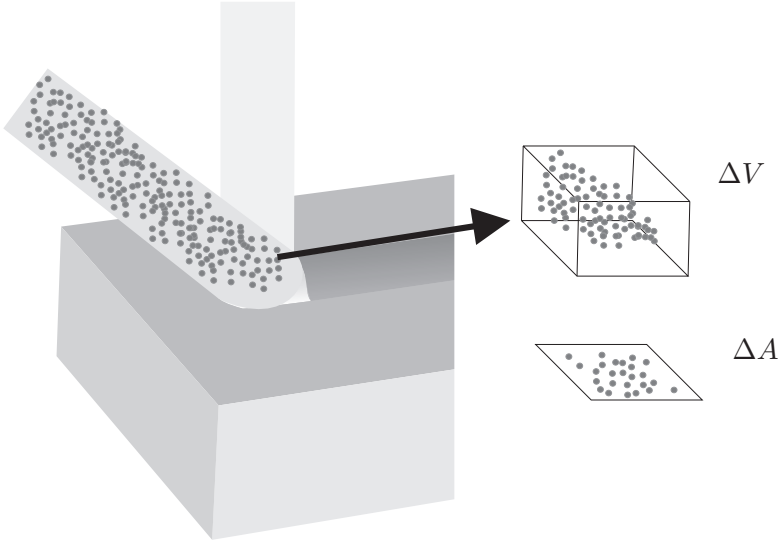


Figure C.2: Optical density of the powder jet.

Define the small volume as:

$$\Delta V = \Delta x_L \Delta y_L \Delta z_L, \quad (\text{C.10})$$

and assuming no overlapping particles, which is valid for low concentration powder clouds, the projected area of the particles $\Delta A = \Delta x_L \Delta y_L$, $A_{proj}(\mathbf{P}_g)$ can be expressed as:

$$\begin{aligned} A_{proj}(\mathbf{P}_g) &= M(\mathbf{P}_g) \frac{A_{particle}}{\rho_{particle} \cdot V_{particle}} \\ &= M(\mathbf{P}_g) \frac{3}{4 \rho_{particle} \cdot r_{particle}} \end{aligned} \quad (\text{C.11})$$

with $A_{particle}$ the (average) frontal area of one particle, $\rho_{particle}$ the density of the powder and $r_{particle}$ the average radius of one particle. The fill ratio $R_f(\mathbf{P}_g)$ of the jet perpendicular to the laser beam at \mathbf{P} can be expressed as:

$$R_f(\mathbf{P}_g) = \frac{A_{proj}(\mathbf{P}_g)}{\Delta x_L \Delta y_L} \quad (\text{C.12})$$

The optical density $\alpha(\mathbf{P}_g)$ is:

$$\alpha(\mathbf{P}_g) = \frac{R_f(\mathbf{P}_g)}{\Delta z_L} \quad (\text{C.13})$$

Combining equations C.9 , C.11 and C.13 gives:

$$\alpha(\mathbf{P}_g) = \frac{3\Phi(\mathbf{e}_\varphi^1 \cdot [\mathbf{P}_g - \mathbf{O}_\varphi], \mathbf{e}_\varphi^2 \cdot [\mathbf{P}_g - \mathbf{O}_\varphi])}{4 \rho_{particle} r_{particle} v} \quad (C.14)$$

The path of the laser radiation from the laser source through point \mathbf{P}_g , $S(\mathbf{P}_g)$ can be expressed as:

$$S(\mathbf{P}_g) = \mathbf{P}_g + s\mathbf{e}_L^3, \quad s \in [-\mathbf{e}_L^3 \cdot [\mathbf{P}_g - \mathbf{O}_L] \dots 0] \quad (C.15)$$

The change in laser power intensity $I_{laser}(\mathbf{P}_g)$ can now be expressed as:

$$\frac{\partial I_{laser}(\mathbf{P}_g + s\mathbf{e}_L^3)}{\partial s} = -\alpha(\mathbf{P}_g + s\mathbf{e}_L^3) I_{laser}(\mathbf{P}_g + s\mathbf{e}_L^3) \quad (C.16)$$

Taking integrals at both sides gives:

$$\begin{aligned} I_{laser}(\mathbf{P}_g + s_2\mathbf{e}_L^3) &= I_{reduction}(\mathbf{P}_g + s_2\mathbf{e}_L^3)I_{laser}(\mathbf{P}_g + s_1\mathbf{e}_L^3) \quad (C.17) \\ I_{reduction}(\mathbf{P}_g + s_2\mathbf{e}_L^3) &= \exp \int_{s_1}^{s_2} -\alpha(\mathbf{P}_g + s\mathbf{e}_L^3) ds \end{aligned}$$

Substituting $s_1 = -\mathbf{e}_L^3 \cdot [\mathbf{P}_g - \mathbf{O}_L]$ and $s_2 = 0$:

$$\begin{aligned} I_{laser}(\mathbf{P}_g) &= I_{reduction}(\mathbf{P}_g)I_{laser}(\mathbf{P}_g - \mathbf{e}_L^3 \cdot [\mathbf{P}_g - \mathbf{O}_L]\mathbf{e}_L^3) \quad (C.18) \\ &= I_{reduction}(\mathbf{P}_g)I_{0,laser}(Px_L, Py_L) \\ I_{reduction}(\mathbf{P}_g) &= \exp \int_{-\mathbf{e}_L^3 \cdot [\mathbf{P}_g - \mathbf{O}_L]}^0 -\alpha(\mathbf{P}_g + s\mathbf{e}_L^3) ds \end{aligned}$$

The integral of equation C.18, $I_{reduction}(\mathbf{P}_g)$ can be expressed as:

$$I_{reduction}(\mathbf{P}_g) = \exp \int_{-\mathbf{e}_L^3 \cdot [\mathbf{P}_g - \mathbf{O}_L]}^0 -\frac{3\Phi(Px_\varphi + 0, Py_\varphi + \mathbf{e}_\varphi^2 \cdot \mathbf{e}_L^3 s)}{4 \rho_{particle} r_{particle} v} ds \quad (C.19)$$

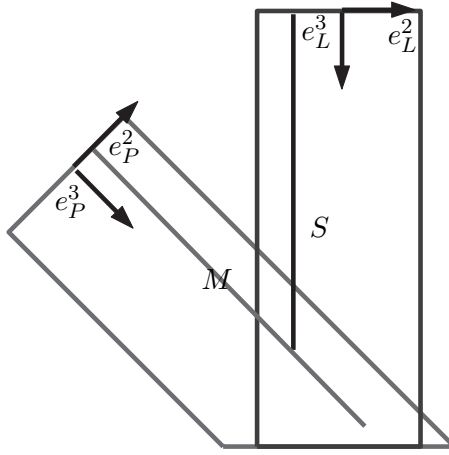


Figure C.3: laser and powder interaction.

Substituting $s' = \mathbf{e}_\varphi^{2T} \mathbf{e}_L^3 s$:

$$\begin{aligned}
 s' &= \mathbf{e}_\varphi^2 \cdot \mathbf{e}_L^3 s, \quad s' \in [-\mathbf{e}_\varphi^2 \cdot \mathbf{e}_L^3 \mathbf{e}_L^{3T} \{\mathbf{P}_g - \mathbf{O}_L\} \dots 0], \\
 \frac{\partial s}{\partial s'} &= \frac{1}{\mathbf{e}_\varphi^2 \cdot \mathbf{e}_L^3} \\
 &\Rightarrow
 \end{aligned} \tag{C.20}$$

$$\begin{aligned}
 I_{reduction}(\mathbf{P}_g) &= \exp \int_{-\mathbf{e}_\varphi^2 \cdot \mathbf{e}_L^3 \mathbf{e}_L^3 \cdot \{\mathbf{P}_g - \mathbf{O}_L\}}^0 -\frac{3\Phi(Px_\varphi, Py_\varphi + s')}{4 \rho_{particle} \cdot r_{particle} \cdot v} \frac{\partial s}{\partial s'} ds' \\
 &= \exp \int_{-\mathbf{e}_\varphi^2 \cdot \mathbf{e}_L^3 \mathbf{e}_L^3 \cdot \{\mathbf{P}_g - \mathbf{O}_L\}}^0 -\frac{3\Phi(Px_\varphi, Py_\varphi + s', 0)}{4 \rho_{particle} \cdot r_{particle} v \mathbf{e}_\varphi^2 \cdot \mathbf{e}_L^3} ds'
 \end{aligned}$$

The lower bound of the integral, $-\mathbf{e}_\varphi^2 \cdot \mathbf{e}_L^3 \mathbf{e}_L^3 \cdot \{\mathbf{P} - \mathbf{O}_L\}$, in practise will always be outside the powder distribution boundary and therefore may be replaced by $-\infty$. Finally, the expression for the laser power at point \mathbf{P}_g can

be written as:

$$I_{laser}(\mathbf{P}_g) = I_{reduction}(\mathbf{P}_g) \cdot I_{0,laser}(Px_L, Py_L) \quad (C.21)$$

$$I_{reduction}(\mathbf{P}_g) = \exp \int_{-\infty}^0 -\frac{3\Phi(Px_\varphi, Py_\varphi + s')}{4 \rho_{particle} r_{particle} v e_\varphi^2 \cdot e_L^3} ds'$$

Power absorption by powder

The path of the powder jet from the powder source through point \mathbf{P}_g , $S(\mathbf{P}_g)$ can be expressed as:

$$M(\mathbf{P}_g) = \mathbf{P}_g + m e_\varphi^3, \quad m \in [-e_\varphi^3 \cdot [P_g - \mathbf{O}_\varphi] \dots 0] \quad (C.22)$$

The change in absorbed power by the powder jet at an arbitrary point \mathbf{P}_g in space can be expressed as:

$$\frac{\partial I_{powder}(\mathbf{P}_g + m e_\varphi^3)}{\partial m} = C_{abs} \alpha(\mathbf{P}_g + m e_\varphi^3) I_{laser}(\mathbf{P}_g + m e_\varphi^3) \quad (C.23)$$

where $\alpha(\mathbf{P}_g + m e_\varphi^3)$ is as defined in equation C.13 and $C_{abs} E [0 1]$ is the absorption coefficient of the powder. Taking integrals at both sides gives:

$$I_{powder}(\mathbf{P}_g + m_2 e_\varphi^3) = C_{abs} \int_{m_1}^{m_2} \alpha(\mathbf{P}_g + m e_\varphi^3) I_{laser}(\mathbf{P}_g + m e_\varphi^3) dm$$

$$I_{laser}(\mathbf{P}_g + m e_\varphi^3) = I_{reduction}(\mathbf{P}_g + m e_\varphi^3) \cdot \dots \quad (C.24)$$

$$I_{0,laser}(e_L^1 \cdot [\mathbf{P}_g - \mathbf{O}_L + m e_\varphi^3], e_L^2 \cdot [\mathbf{P}_g - \mathbf{O}_L + m e_\varphi^3])$$

Note that (using equations C.20 and C.14) $I_{reduction}(\mathbf{P}_g + m e_\varphi^3)$ and $\alpha(\mathbf{P}_g + m e_\varphi^3)$ are constant along M .

$$I_{powder}(\mathbf{P}_g + m_2 e_\varphi^3) = C_{abs} \int_{m_1}^{m_2} \alpha(\mathbf{P}_g) I_{laser}(\mathbf{P}_g + m e_\varphi^3) dm \quad (C.25)$$

$$I_{laser}(\mathbf{P}_g + m e_\varphi^3) = I_{reduction}(\mathbf{P}_g) \cdot \dots$$

$$I_{0,laser}(e_L^1 \cdot [\mathbf{P}_g - \mathbf{O}_L + m e_\varphi^3], e_L^2 \cdot [\mathbf{P}_g - \mathbf{O}_L + m e_\varphi^3])$$

$$= I_{reduction}(\mathbf{P}_g) I_{0,laser}(Px_L - 0, Py_L + e_L^2 \cdot e_\varphi^3 m).$$

Substituting $m_1 = -\mathbf{e}_\varphi^3 \cdot [P_g - \mathbf{O}_\varphi]$ and $m_2 = 0$:

$$I_{powder}(\mathbf{P}_g) = C_{abs}\alpha(\mathbf{P}_g)I_{reduction} \cdot \dots \quad (\text{C.26})$$

$$(\mathbf{P}_g) \int_{-\mathbf{e}_\varphi^3 \cdot [P_g - \mathbf{O}_\varphi]}^0 I_{0,laser}(Px_L, Py_L + \mathbf{e}_L^2 \cdot \mathbf{e}_\varphi^3 m) dm$$

Substituting $m' = \mathbf{e}_L^2 \cdot \mathbf{e}_\varphi^3 m$:

$$m' = \mathbf{e}_L^{2T} \mathbf{e}_\varphi^3 m, \quad m' \in [-\mathbf{e}_L^{2T} \mathbf{e}_\varphi^3 \mathbf{e}_\varphi^3 \cdot \{\mathbf{P}_g - \mathbf{O}_\varphi\} \dots 0],$$

$$\frac{\partial m}{\partial m'} = \frac{1}{\mathbf{e}_L^2 \cdot \mathbf{e}_\varphi^3} \quad (\text{C.27})$$

Equation C.26 can be expressed as:

$$I_{powder}(\mathbf{P}_g) = \frac{C_{abs}\alpha(\mathbf{P}_g)I_{reduction}(\mathbf{P}_g)}{\mathbf{e}_L^2 \cdot \mathbf{e}_\varphi^3} \cdot \dots \quad (\text{C.28})$$

$$\int_{-\mathbf{e}_L^{2T} \mathbf{e}_\varphi^3 \mathbf{e}_\varphi^3 \cdot \{\mathbf{P}_g - \mathbf{O}_\varphi\}}^0 I_{0,laser}(Px_L, Py_L + m') dm'$$

The lower bound of the integral, $-\mathbf{e}_L^2 \cdot \mathbf{e}_\varphi^3 \mathbf{e}_\varphi^3 \cdot \{\mathbf{P}_g - \mathbf{O}_\varphi\}$, in practice will always be outside the powder distribution boundary and therefore may be replaced by $-\infty$. Finally, the expression for the powder power at point \mathbf{P}_g can be written as:

$$I_{powder}(\mathbf{P}_g) = \frac{C_{abs}\alpha(\mathbf{P}_g)I_{reduction}(\mathbf{P}_g)}{\mathbf{e}_L^2 \cdot \mathbf{e}_\varphi^3} \int_{-\infty}^0 I_{0,laser}(Px_L, Py_L + m') dm' \quad (\text{C.29})$$

Appendix D

Cross-section images of Clad tracks using a 3.0 mm spot

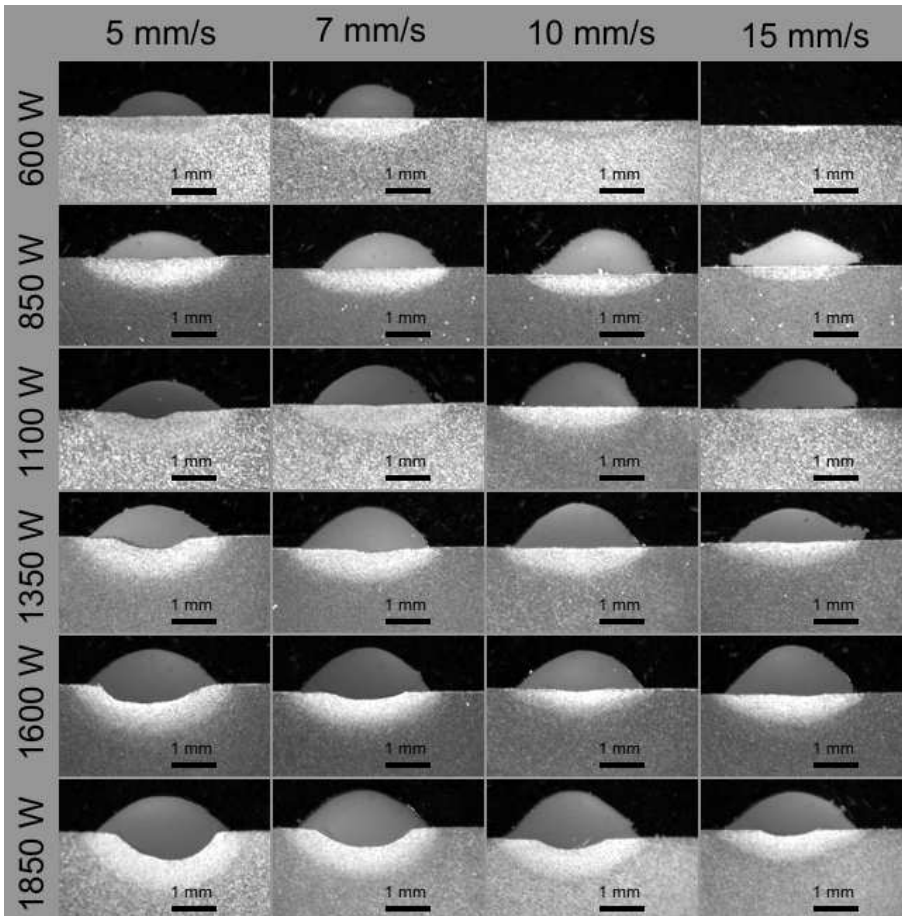


Figure D.1: Images of the samples produced using a 3.0 mm spot. From top to bottom: Laser power increases, from left to right: cladding speed increases.

Appendix E

Cross-section images of Clad tracks using a 4.5 mm spot

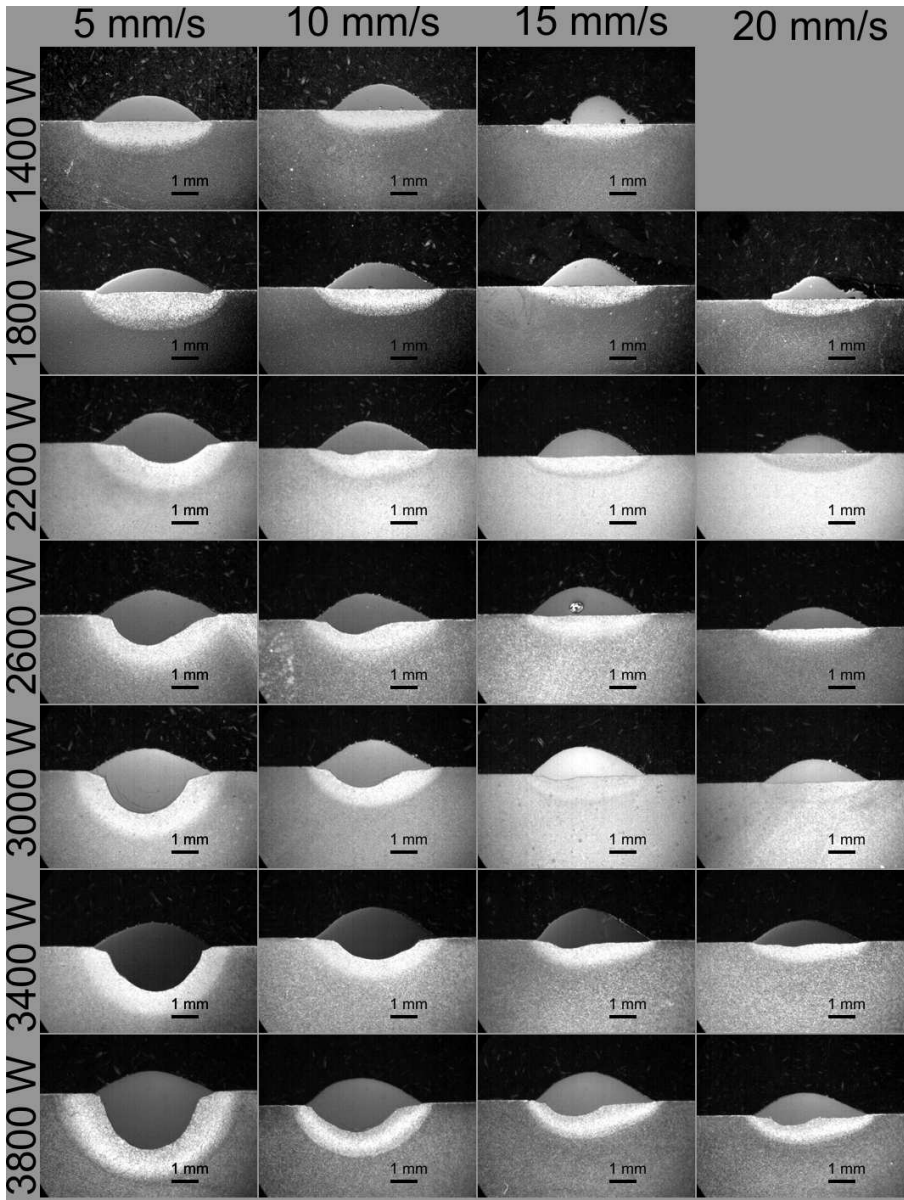


Figure E.1: Images of the samples produced using a 4.5 mm spot. From top to bottom: Laser power increases, from left to right: cladding speed increases.

Appendix F

Cross-section images of Clad clad layers

The following microscopic images of clad layers are from experiments as described in chapter 9. The process setting can be found in Table 9.3.

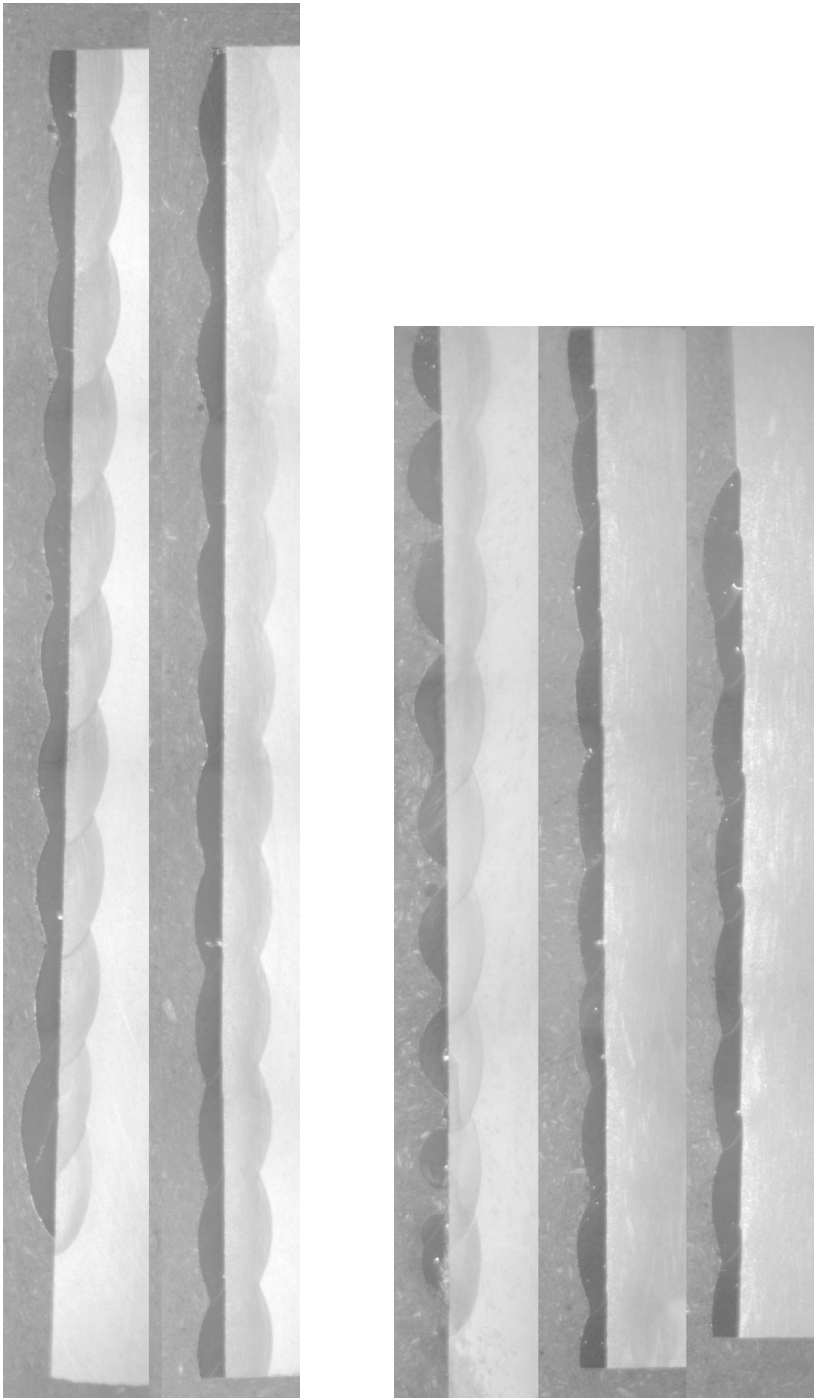


Figure F.1: Experiment 3 and 4.

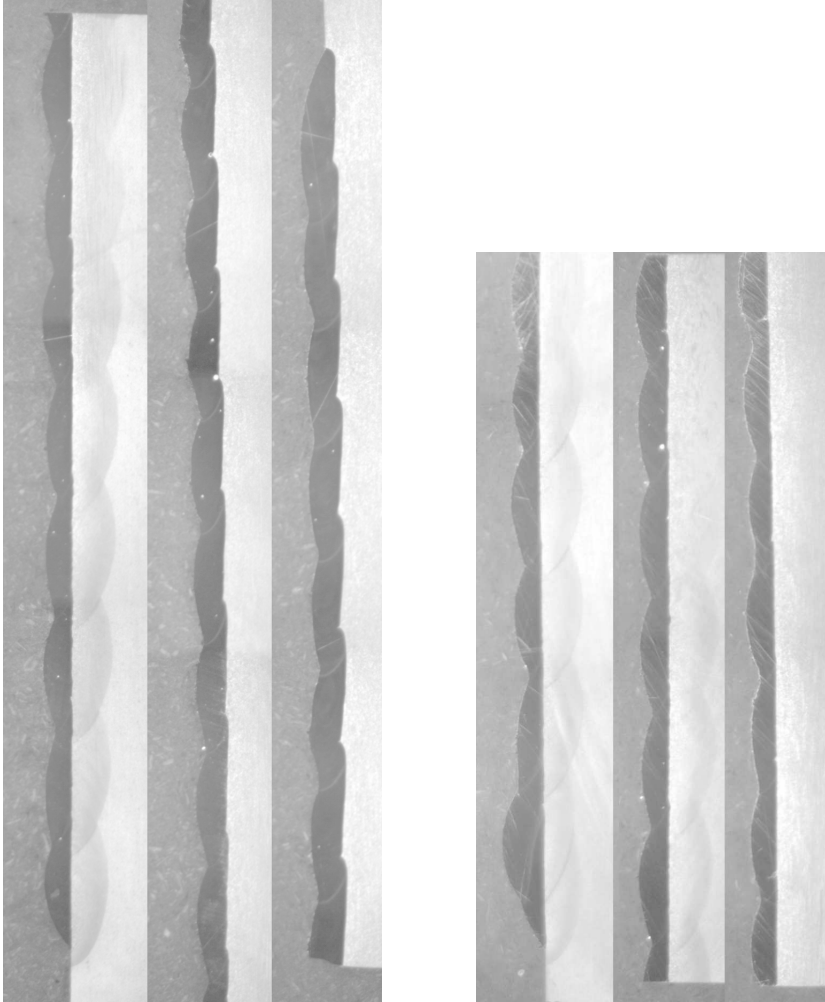


Figure F.2: Experiment 5 and 6.

Samenvatting

Ontwikkeling van een observatie en regelsysteem voor industrieel Laser cladden

Laser cladden is een coating techniek voor het aanbrengen van dikke lagen. Een van de bijzondere eigenschappen van deze lagen is de inter-metalische binding tussen het substraat en de coating. Tegenwoordig vormt laser cladden een belangrijke oppervlakte bewerkingstechniek in de industrie en de markt hiervoor blijft groeien. Laser cladden wordt niet alleen toegepast voor het coaten van een product maar ook voor reparatie en rapid prototyping.

Binnen het uitgevoerde onderzoek is een laser clad werkstation ontwikkeld. Dit werkstation maakt gebruik van een 4 kW fiber gekoppelde Nd:Yag laser. Het laser licht wordt door middel van een optisch systeem bestaande uit meerdere lenzen op het werkstuk gefocusseerd. Dit systeem is op een 6-assige robot gemonteerd waarmee het cladden van complexe geometrieën mogelijk wordt. Vaak wordt voor het cladden een gedefocusseerde laserstraal gebruikt om een grote spot te produceren. De energie verdeling is in zo'n geval verre van constant. Als gevolg hiervan neigt het substraat materiaal in het midden oververhit te raken. Als onderdeel van dit onderzoek is een nieuw optisch systeem ontwikkeld en gebruikt. Dit systeem combineert de voordelen van de energieverdeling van de uniforme verdeling met een praktische werkafstand. Het clad materiaal wordt aangevoerd door een flexibele buis en in het smeltbad geblazen door middel van een poeder nozzle. Een gas stroom met hoge snelheid rondom de poederstraal voorkomt dat deze kan divergeren.

Een camera gebaseerd observatie systeem voor het laser clad proces

is ontwikkeld. Dit systeem levert instantane beelden van het smeltbad. Een optische filter, dat voor de camera is geplaatst, onderdrukt de lasersstraling zodat alleen de temperatuurstraling van het smeltbad de sensor van de camera bereikt. De afmetingen van het smeltbad kunnen in realtime bepaald worden door een speciaal hiervoor geschreven software programma.

Er is een uitgebreide reeks clad experimenten uitgevoerd. Tijdens deze experimenten zijn de belangrijkste procesvariabele zoals de spot grootte, het laser vermogen, de clad snelheid en de poeder hoeveelheid gevarieerd. Met behulp van deze experimenten kunnen optimale proces instellingen bepaald worden.

Een belangrijke kwaliteitsparameter van het clad proces is de hoeveelheid opmenging van substraat materiaal in de coating. Onvoldoende opmenging kan tot een zwakke verbinding leiden. Een grote mate van opmenging leidt tot onbekende kwaliteit van de clad laag. Het is dus van belang om de opmenging tijdens het cladden in de hand te houden. Uit het experimentele werk is een duidelijke correlatie tussen de opmenging en de breedte van het smeltbad waargenomen. Deze breedte kan in tegenstelling tot de opmenging tijdens het cladden worden gemeten. Hierdoor is het mogelijk om de opmenging te beïnvloeden tijdens het proces door het laser vermogen aan te passen.

Een model van het laser clad proces is ontwikkeld met behulp van de Eindige Elementen Methode. Dit model kan nauwkeurig de vorm en de temperatuur van de clad lagen voorspellen, ondermeer door een goede modelering van de interactie tussen de laser- en de poederstraal. Met het model is het mogelijk om informatie over de temperatuur de temperatuurgradiënten in de clad sporen te bepalen. De model resultaten met betrekking tot geometrisch parameters als spoor hoogte en breedte en hoeveelheid opmenging zijn in goede overeenstemming met experimentele resultaten. De correlatie tussen de breedte van het smeltbad en de opmenging zoals waargenomen tijdens de experimenten blijkt ook te bestaan als de initiële temperatuur van het substraat materiaal toeneemt.

Als gevolg van de complexiteit van het laser clad proces met inbegrip van de interactie tussen de laser en het materiaal en materiaal eigenschappen, is een bekwame operator vereist. Wil de laser clad techniek verder groeien in de industrie, dan zal deze techniek eenvoudiger moeten

worden. Dit vereist een hoge mate van automatisering. Een feedback regelsysteem gebaseerd op de breedte van het smeltbad en zijn relatie met de opmenging, is ontwikkeld en geïmplementeerd. Dit systeem gebruikt de smeltbad breedte zoals gemeten met het camera systeem en past het laser vermogen realtime aan. Als gevolg hiervan wordt de opmenging beheerst en gelijktijdig een minimale warmte inbreng en product vervorming gegarandeerd. Als gevolg hiervan wordt de hardheid van de clad laag ook op een constante waarde gehouden.

De regelstrategie is in c++ code geschreven en draait onder WindowsTM. Dit systeem is industrieel geïmplementeerd bij Stork Gears & Services, Rotterdam. Dit systeem stelt Stork in staat om de clad technologie verder te benutten en geeft hen een kwaliteitsgarantie die zonder zo'n systeem niet verkregen kan worden.

Als gevolg van hoge temperatuur gradiënten en verschillen in de materiaal eigenschappen tussen clad materiaal en substraat, kunnen hoge rest spanningen of zelfs scheuren in de clad lagen ontstaan. Deze scheuren kunnen vaak worden voorkomen door gebruik te maken van een ductiele tussenlaag. Om de invloed van de clad snelheid op de ontwikkeling van deze rest spanningen te kwalificeren is een eenvoudige en snelle methode ontwikkeld, gebaseerd op doorbuigingen. De rest spanningen zoals bepaald met deze methode zijn vergeleken met de spanningen zoals gemeten met röntgendiffractie. Indien de spanningen groot zijn (vaak het geval bij bijvoorbeeld een harde clad laag) levert deze methode een goede schatting van de spanningen.

Acknowledgment

Vier jaar onderzoek gaan snel voorbij. Mijn onderzoek heb ik uitgevoerd binnen de leerstoel Toegepaste Laser Technologie van de vakgroep Werktuigbouwkundige Automatisering. Vooral het automatiseringsaspect trok mij erg aan. Ik heb hier dan ook de nadruk op gelegd tijdens de afgelopen jaren.

Mijn onderzoek werd gefinancierd door het M2i, toen nog NIMR. Ik wil M2i dan ook bedanken voor deze kans. Ik heb de richting van mijn onderzoek voor een groot deel zelf kunnen bepalen. Dit kwam ondermeer door de grote vrijheid die mijn promotor Prof. Meijer mij gaf. Hartelijk bedankt voor de begeleiding. Ik heb al onze gesprekken zeer gewaardeerd. Uiteraard bedank ik Prof. Meijer en Dr. Pathiraj voor de uitgebreide hulp met het schrijven van mijn proefschrift evenals Dr. de Lange voor zijn uitgebreide ondersteuning bij het ontwikkelen van het model en het ontwerp van het optische systeem. Ook wil ik Jeroen Olde Benneker bedanken, ondermeer voor de contacten met Stork. Ronald, bedankt voor het helpen instellen van de regelaar. Tyrone, bedankt voor het realiseren van de clad cell met de benodigde elektronica. Leo, bedankt voor de hulp tijdens het ontwerp en de productie van het optische systeem. Johannes wil ik nog bedanken voor zijn feedback op het hoofdstuk over het ontwerp van de regelaar.

Ik heb mijn werk bij de vakgroep als erg plezierig ervaren. Dit kwam in grote mate door alle gezellige collega's. Ik heb de inhoudelijk discussies, de wederzijdse hulp en de gezelligheid zeer gewaardeerd.

Via het M2i kwam ik in contact met Stork Gears & Services, met name Jelmer Brugman. De door mij ontwikkelde regelstrategie heb ik bij hen geïmplementeerd. Dit was voor mij een erg leuke en leerzame ervaring.

Als laatste bedank ik Janet. Ik kon altijd bij jou terecht als ik het even niet meer zag zitten, of juist wel. Bedankt voor jou hulp en geduld tijdens mijn promotie periode.

Bibliography

- [1] W.M. Steen. *Laser Material Processing*. Springer, second edition, 1998.
- [2] B. C. Oberländer and E. Lugscheider. Comparison of properties of coatings produced by laser cladding and conventional methods. *Materials Science and Technology*, 8:657 – 665, 1992.
- [3] T. Weber. Advances in the application of laser cladding of multi-dimensional part geometry's. *Proceedings of Laser in Motion for Industrial Applications, 1987, Los Angeles, CA*, 744:137 – 143, 1987.
- [4] R. Vilar. Laser cladding. *Journal of laser applications*, vol. 11:64 – 79, 1999.
- [5] M. F. Schneider. *Laser cladding with powder*. PhD thesis, University of Twente, The Netherlands, 1998.
- [6] D. S. Salehi. *Sensing and Control of Nd:YAG Laser Cladding Process*. PhD thesis, Swinburne University of Technology, Melbourne, Australia, 2005.
- [7] H. Gedda. Laser surface cladding, a literature survey. Technical report, Lulea Tekniska Universitet, 2000.
- [8] R. M. MacIntyre. Surfacing of gas turbine blade shroud interlocks. *Proceedings of LIM*, pages 86–94, 1983.
- [9] M. Eboo and A. E. Lindemanis. Advances in laser cladding technology. *Proceedings of ICALEO*, pages 31 – 39, 1983.
- [10] J. Hannweber, S. Bonss, and B. Brenner. Integrated laser system for heat treatment with high power diode laser. *Proceedings of ICALEO*, pages 1503–1508, 2004.

- [11] M. Seifert, S. Bonss, and B. Brenner. High power diode laser beam scanning in multi-kW range. *Proceedings of ICALEO*, pages 1201–1206, 2004.
- [12] G. Habedank, C. Theiler, M. Grupp, H. Kohn, G. Sepold, and F. Voltertsen. Laser beam cladding of steel with high power diode lasers. *Proceedings of LIM*, page 4549, 2003.
- [13] K. Partes, C. Theiler, and T. Seefeld. Laser cladding powered by diode lasers at high processing speed. *Lasers in Manufacturing*, pages 51–55, 2003.
- [14] V. Gapontsev. Industrial high power fiber laser systems. *Proceedings of the 2nd International Workshop on Fiber Lasers, dresden, Germany*, 2006.
- [15] G. R. B. E. Römer, R. G. K. M. Aarts, and J. Meijer. Dynamic models for laser surface alloying. *Lasers in Engineering*, 8:251–266, 1999.
- [16] G. R. B. E. Römer, H. Zwart, K. A. J. de Graaf, and J. Meijer. Modeling of the temperature field induced by laser surface irradiation in view of feedback control theory. *Lasers in Engineering*, 7:179–197, 1998.
- [17] G. R. B. E. Römer and J. Meijer. Inverse calculation of power density for laser surface treatment. *Annals of the CIRP*, vol 49:135–138, 2000.
- [18] E. Toyserkani, A. Khajepour, and S. F. Corbin. *Laser Cladding*. CRC Press, 2004.
- [19] M. Bamberger, W. D. Kaplan, B. Medres, and L. Shrprrlva. Calculation of process parameters for laser alloying and cladding. *Journal of laser Applications*, 10:29–33, 1998.
- [20] J. D. Kim and Y. Peng. Melt pool shape and dilution of laser cladding with wire feeding. *Journal Materials Processing Technology*, 104:284–293, 2000.
- [21] G. R. B. E. Römer, J. Meijer, and J. Olde Benneker. Process control of laser surface alloying. *Surface Engineering*, 14 - 4:295–298, 1998.
- [22] G. R. B. E. Römer, N. P. Weerkamp, J. Meijer, and J. Postma. Non-minimum phase behavior of laser material processing. *Proceedings of ICALEO*, pages 15 – 18, 2001.

- [23] G. R. B. E. Römer, M. Hoeksma, and J. Meijer. Industrial surface imaging controls laser surface treatment. *Photonics in manufacturing*, pages 104–110, 1997.
- [24] R. Jendrzewski, I. Kreja, and G. Sliwinski. Temperature distribution in laser-clad multilayers. *Materials Science and Engineering, A* 379: 313–320, 2004.
- [25] G. Palumbo, S. Pinto, and L. Tricarico. Numerical finite element investigation on laser cladding treatment of ring geometries. *Journal of Materials Processing Technology 155-156*, pages 1443–1450, 2004.
- [26] E. Toyserkani, A. Khajepour, and S. Corbin. Three-dimensional finite element modeling of laser cladding by powder injection: Effects of powder and travel speed on the process. *Journal of Laser Applications*, 15:153–160, 2003.
- [27] M. Picasso, C. F. Marsden, J. D. Wagniere, A. Frenk, and M. Rap-paz. A simple but realistic model for laser cladding. *Metallurgical and Materials Transactions, B* 25:281–291, 1994.
- [28] M. Sameni, E. Toyserkani, and A. Khajepour. Fuzzy model and compact fuzzy model identification of laser cladding process. *Proceedings of ICALEO*, 23:17–22, 2004.
- [29] F. Brückner, D. Lepski, and E. Beyer. Simulation of thermal stress in induction-assisted laser cladding. *Proceedings of ICALEO*, 26:647–656, 2007.
- [30] F. Brückner, D. Lepski, and E. Beyer. Modeling the influence of process parameters and additional heat sources on residual stresses in laser cladding. *Journal of thermal spray technology*, 16 No.3:355–373, 2007.
- [31] van J. Vaerenbergh. *Process Optimisation in Selective Laser Melting*. PhD thesis, University of Twente, 2008.
- [32] G. Bi, A. Gasserb, K. Wissenbachb, A. Drenkerb, and R. Popraweb. Identification and qualification of temperature signal for monitoring and control in laser cladding. *Optics and Lasers in Engineering*, 44: 1348–1359, 2006.

- [33] D. S. Salehi and M. Brandt. Melt pool temperature control using LabVIEW in Nd:YAG laser blown powder cladding process. *The international journal of advanced manufacturing technology*, 29:273 – 278, 2006.
- [34] G. R. B. E. Römer. *Modelling and control of laser surface treatment*. PhD thesis, University of Twente, 1999.
- [35] E. Toyserkani, A. Khajepour, and S. Corbin. Closed-Loop Control of Laser Cladding Process by Powder Injection. *Proceedings of ICALEO*, 2003.
- [36] U. de Oliveira, V. Ocelk, and J.Th.M De Hosson. Residual stresses in Co-based laser claddings investigated by lab X-rays and synchrotron diffraction techniques. *Computer Methods and Experimental Measurements for Surface Effects and Contact Mechanics VII '05*, pages 241 – 250, 2005.
- [37] G. Zhao, C. Cho, and J.D. Kim. Application of 3-d finite element method using Lagrangian formulation to dilution control in laser cladding process. *International Journal of Mechanical Sciences*, 45:777–796, 2003.
- [38] C. Limmaneevichitr and S. Kou. Experiments to simulate effects of marangoni convection on weld pool shape. *Welding Journal*, 79:231–237, 2000.
- [39] F. Vollertsen, K. Partes, and J. Meijer. State of the art of laser hardening and cladding. *Proceedings of the Third International WLTC Conference on Lasers in Manufacturing '05*, pages 281 – 305, 2005.
- [40] S. Kumar and S. Roy. Development of theoretical process maps to study the role of powder preheating in laser cladding. *Computational Materials Science '2006*, 37:425 – 433, 2006.
- [41] A. Bejan. *Heat Transfer*. John Wiley and Sons, Inc, first edition, 1993.
- [42] G. Bi, B. Schürmann, A. Gasser, K. Wissenbach, and R. Poprawe. Development and qualification of a novel laser-cladding head with integrated sensors. *International Journal of Machine Tools and Manufacture '2007*, 47:555 – 561, 2007.

- [43] G.F. Franklin, J.D. Powell, and A. Naemi-Emani. *Feedback Control of Dynamic Systems*.
- [44] V.M. Hauk and E. Macherauch. Useful Guide for X-Ray Stress Evaluation. *Advances in X-Ray Analysis 27 '84*, pages 81 – 99, 1984.
- [45] E. Macherauch. X-ray stress analysis. *Proceedings of the 2nd SESA International Congress on Experimental Mechanics '65*, pages 140 – 153, 1965.
- [46] E. Macherauch and P. Müller. Das $\sin^2\psi$ -Verfahren der röntgenographischen Spannungsmessung. *Zeitschrift für Angewandte Physik 13 '61*, pages 304 – 312, 1961.